Therapeutic approaches for two distinct CNS pathologies

Dissertation

for the award of the degree
"Doctor rerum naturalium"
of the Georg-August-Universität Göttingen

within the doctoral program *Center for Systems Neuroscience*
of the Georg-August University School of Science (GAUSS)

submitted by
Sina Kristin Stumpf
from Peine, Germany

Göttingen, 2018

Thesis Committee

Dr. Gesine Saher (1. Reviewer)
Department of Neurogenetics
Max Planck Institute of Experimental Medicine, Göttingen

Prof. Dr. André Fischer (2. Reviewer)
Department of Psychiatry and Psychotherapy
German Center for Neurodegenerative Diseases

Prof. Dr. Thomas Bayer
Department of Molecular Psychiatry
Clinic for Psychiatry

Further members of the Examination Board

Prof. Dr. Frauke Alves
Department of Molecular Biology of Neuronal Signals
Max Planck Institute of Experimental Medicine, Göttingen

Prof. Dr. Jens Frahm
Managing Director of Biomedical NMR Research GmbH
Max Planck Institute for Biophysical Chemistry

Prof. Dr. Ralf Heinrich
Department of Neurobiology
Institute for Zoology and Anthropology

Date of oral examination: 25.06.2018

Declaration

I hereby declare that the Ph. D. thesis entitled, "Therapeutic approaches for two distinct CNS pathologies", was written independently and with no other sources and aids than quoted.

Göttingen, 04.05.2018

Sina Kristin Stumpf

Acknowledgements

First of all, I thank my supervisor Dr. Gesine Saher for the opportunity to work on two highly interesting projects. Inspiring scientific discussions, but further her great support and guidance throughout the whole PhD contributed to my work.

I further thank Prof. Klaus-Armin Nave for giving me the opportunity to work in his department and for sharing his scientific experience and knowledge.

I thank my thesis committee members, Prof. Dr. André Fischer and Prof. Dr. Thomas Bayer for the support during my PhD including ideas and advices during the committee meetings that contributed to my work. Furthermore, I thank my extended examination board, Prof. Dr. Ralf Heinrich, Prof. Dr. Jens Frahm and Prof. Dr. Frauke Alves for their interest in my project and the participation of my thesis defense.

I am thankful to my collaborators: Dr. Petra Hülper, Dr. Thomas Michaelis, Dr. Takashi Watanabe, Dr. Sabine Höfer and Prof. Jens Frahm for their supportive contribution towards my project.

Many thanks goes to …

… the whole Saher/Cholesterol group, Stefan Berghoff, Nina Gerndt, Jan Winchenbach, Tim Düking, Lena Spieth, Carolin Böhler and Silvia Thüne for their scientific, technical and personal support during my time as a PhD student. Furthermore, Stefan Berghoff and Nina Gerndt for their active support in my project by the quantification of BBB permeability and the contribution of important cell culture experiments, respectively.

… Dinah Burfeind for her contribution to this project during her lab rotation and master thesis.

… Dr. Theresa Kungl and Dr. Thomas Prukop for exchange of information regarding Plp-tg mice.

… Annette Fahrenholz, Verena Meywirth, Dr. Katrin Kusch, Ulli Bode, and Ramona Jung for very valuable technical support.

… Dr. Wiebke Möbius, Torben Ruhwedel and Boguslawa Sadowski for advices and introductions into electron microscopy.

… Michaela Schmalstieg and Gabriele Endo for their help regarding administrative issues

… Hajo Horn, Rolf Merker and Lothar Demel for IT support.

… my colleagues and friends of the whole Neurogenetics department for a great working atmosphere and lots of fun during lunch breaks, retreats and other social events.

At last I thank my family and especially my parents, my grandmother and Oliver for their constant support, persistent care and love. Together with my happy little son Jonathan, they provided the basis of my achievements.

Table of Contents

1 List of Figures

2 Abbreviations

ACC1/Acaca	Acetyl-coA carboxylase 1
ACAT1	Acetyl-coA acetyltransferase 1
AIF1	Allograft inflammatory factor 1
ApoE	Apolipoprotein E
APP	Amyloid precursor protein
AQP4	Aquaporin 4
ATF	Activating transcription factor
ATP	Adenosine triphosphate
BBB	Blood-brain barrier
BDH1	β-Hydroxybutyrate dehydrogenase 1
BIP	Binding immunoglobulin protein
bp	Base pairs
BSA	Bovine serum albumin
°C	Degrees Celsius (centigrades)
CAII/Car2	Carbonic anhydrase II
Cav1	Caveolin 1
CCL2	CC-*chemokine* ligand 2
CD3	Cluster of differentiation 3
chol	Cholesterol
CHOP	CCAAT-enhancer-binding protein homologous protein
Cldn5	Claudin-5
CNP	2'3'-cyclic nucleotide 3'phosphodiesterase
CNS	Central nervous system
CoA	Coenzyme A
CSF	Cerebral spinal fluid
CSPG4	*Chondroitin sulfate proteoglycan 4*
CST	Cortiospinal tract
Ctrl	Control
DAB	3,3'-Diaminobenzidine
DAPI	4'-6-Diamidino-2-phenylindole
ddH2O	Double distilled water
DNA	Deoxyribonucleic acid
dNTPs	Desoxyribonukleosidtriphosphate
EB	Evans blue

EC	Endothelial cell
EdU	5-Ethynyl-2′-deoxyuridine
e.g.	Exempli gratia
EGTA	Ethylene-bis(oxyethylenenitrilo)tetraacetic acid
EM	Electron microscopy
ER	Endoplasmic reticulum
ERAD	Endoplasmic-reticulum-associated protein degradation
EtOH	Ethanol
FASN	Fatty acid synthase
FDFT1	Farnesyl-diphosphate farnesyltransferase 1
g	Gram
GBM	Glioblastoma multiforme
GFAP	Glial fibrillary acidic protein
GFP	Green fluorescent protein
h	Hour
HCl	Hydrogen chloride
HEXA	Hexosaminidase
HIF1α	Hypoxia-inducible factor 1 α
Hmgcr	3-Hydroxy-3-methylglutaryl-CoA reductase
Hmgcs1	3-Hydroxy-3-methylglutaryl-coA synthase 1
HRP	Horseradish peroxidase
HS	Horse serum
IHC	Immunohistochemistry
IL	Interleukin
Iso	Isoflurane
i.v.	Intravenously
JAM	Junctional adhesion molecule
KD	Ketogenic diet
kDa	Kilodalton
LAMP1	Lysosomal-associated membrane protein 1
LPS	Lipopolysaccharide
M	Molar
mA	Milliampere
MAC3	Macrophage-3 antigen
MAG	Myelin-associated glycoprotein

MAN2B1	alpha-Mannosidase
MBP	Myelin basic protein
MCAO	Middle cerebral artery occlusion
MCT	Monocarboxylate transporters
min	Minutes
µl	Microliter
µM	Micromolar
µm	Micrometer
mm	Millimeter
mM	Millimolar
MMP	Matrix metalloproteinase
MOG	*Myelin* oligodendrocyte glycoprotein
MPI	Max Planck Institute
mRNA	Messenger ribonucleic acid
MRI	Magnetic resonance imaging
n	Number
NADPH	Nicotinamide Adenine Dinucleotide Phosphate Hydrogen
NG2	Nerve-glia antigen 2 proteoglycan
NMDA	N-Methyl-D-aspartic acid or N-Methyl-D-aspartate
NPC	Niemann-Pick disease type C
ns	Not significant
nm	Nanometer
NVU	Neurovascular unit
OCLN	Occludin
OLIG2	Oligodendrocyte lineage transcription factor 2
o/n	Overnight
OPC	Oligodendrocyte precursor cell
OXCT1	3-Oxoacid CoA-transferase
P	Postnatal day
PBS	Phosphate buffered saline
PCR	Polymerase chain reaction
PDGF-β	Platelet-derived growth factor β
PDZ domain	Protein binding domain
PECAM1	Platelet EC adhesion molecules
PFA	Paraformaldehyde

PHD/Egln	Prolyl hydroxylases
PLP	Proteolipid protein
PMD	Pelizaeus-Merzbacher disease
ROS	Reactive oxygen species
RPLP0	Ribosomal protein lateral stalk subunit P0
rpm	Rounds per minute
RT	Room temperature
SC	Spinal cord
SD	Standard diet
sec	Second
s.e.m	Standard error of the mean
SDS	Sodium dodecyl sulfate
siRNA	small inhibitory RNA
SLC	Solute carrier
TCA	Tricarboxylic acid cycle
tg	Transgen
TGFβ	*Transforming growth factor beta-3*
TNF	Tumor necrosis factor
TUNEL	Terminal deoxynucleotidyl transferase dUTP nick end labeling
UPR	Unfolded protein response
V	Volt
VEGF	Vascular endothelial growth factor
WHO	World Health Association
w/o	Without
WST-1	Water soluble tetrazolium salt assay
WT	Wildtype
XBP	Xbox binding protein
ZO1/Tjp1	Zona occludens

3 Abstract

This work summarizes the analysis of two distinct therapeutic approaches for the central nervous system (CNS) pathologies, Pelizaeus-Merzbacher disease (PMD) and Glioblastoma multiforme (GBM).

PMD is a severe leukodystrophy that is mainly caused by the overexpression of the myelin proteolipid protein (PLP) in oligodendrocytes. Transgenic mice that mimic PLP overexpression (Plp-tg) served as a suitable model system to analyze a novel therapeutic approach by feeding a ketogenic diet (KD). In this study, KD treatment improved pathology in Plp-tg mice. In fact, KD treated Plp-tg mice revealed reduced inflammation and decreased lysosomal PLP accumulation with a diminished ER stress response. In addition, KD treatment increased oligodendrocyte numbers with enhanced myelination and amelioration of the impaired motor phenotype. Moreover, KD enhanced ketone body transport and utilization in the CNS, which was accompanied by an amelioration of axonal pathology. The present work summarizes an innovative therapeutic approach for PMD, in which ketone bodies can be integrated into CNS metabolism without the prerequisite of blood-brain barrier (BBB) alterations. This approach would provide a major advantage for PMD patients, since the status of BBB function is still unknown.

GBM is highly malignant form of brain tumors, in which standard treatment only provided minor impact on patients' survival. The major challenge in the chemotherapy of patients is the application of therapeutically relevant concentrations into the brain due to limitation of the BBB. This thesis presents a therapeutic strategy that comprises a combined treatment of the cytostatic agent cisplatin with controlled manipulation of BBB permeability by isoflurane anesthesia in a GBM mouse model. Highlighting the therapeutic benefit of the approach, the combined treatment of cisplatin and isoflurane reduced tumor volume and enhanced the immune response measured by elevated numbers of T-cell infiltration. In addition tumor viability was reduced. The major benefit of our therapeutic approach was the remarkably reduction of migrating tumor cells into healthy brain tissue. Therefore, the investigated therapeutic strategy for GBM research represents a novel approach to target in addition to the tumor center, migrating tumor cells to prevent the tumor from spreading. This strategy would provide future perspectives for GBM therapy in patients.

4 Ketogenic diet ameliorates disease expression in a mouse model of Pelizaeus-Merzbacher disease

4.1 Introduction

4.1.1 Central nervous system

The mammalian central nervous system (CNS) acts as a control center for most of the conscious body functions, including movement, thoughts and speech, but also sustains homeostasis of body temperature, breathing and heart rate. The CNS consists of the brain and spinal cord, which are connected via the brainstem. Furthermore, the spinal cord serves as the connection of the brain to the peripheral nerves. The blood-brain-barrier (BBB) provides the separation from the CNS and the periphery e.g. by regulation of metabolic influx and efflux as well as the protection from neurotoxic substances (see chapter BBB 5.1.1). Two types of tissue can be found within the CNS: the grey matter, which consists mostly of neurons and neuronal cell bodies and the white matter that contains axons. Within the white matter, most axons are ensheathed by a lipid-rich multilayered stack of membranes, also called the myelin sheath. Glia cells, earlier seen as the “glue” between neurons, were shown to be important supporters for neurons and harbor many other functions including the adjustment of metabolic homeostasis (Kettenmann and Verkhratsky, 2011). In the CNS, glia cells outnumber neurons in a ratio of 10 to 1, including astrocytes, oligodendrocytes, microglia and endothelial cells. Astrocytes provide nutrients to support synapses and axons (Pellerin and Magistretti, 1994; Supplie et al., 2017) and help maintaining BBB structure (Abbott et al., 2010). Oligodendrocytes are the myelinating glia cells in the CNS, but also provide direct metabolic support for the axon (e.g. lactate, pyruvate) (Fünfschilling et al., 2012; Hirrlinger and Nave, 2014). Microglia are immune system cells, acting as the primary immune response of the CNS and further show phagocytic function to clear cell debris. Endothelial cells provide the lining of the cerebral blood vessel. Tightly connected to each other, they build up one component of the BBB (Abbott et al., 2010).

4.1.2 Brain energy metabolism

Since the mammalian brain volume and complexity increased during development, efficient energy metabolism became fundamental. The human brain energy consumptions accounts for 20% of the total ATP production. All cells of the CNS are able to produce and use energy in form of ATP.

4.1.2.1 Glucose metabolism

Glucose, as the primary energy source of the brain, enters the CNS through glucose transporters. The expression of glucose transporters is diverse throughout cells types. The most important glucose transporter, GLUT1, is mainly expressed by astrocytes and endothelial cells, whereas GLUT3 and GLUT5 by neurons and microglia, respectively. (Vannucci et al., 1997; Zhang et al., 2014). Once entering the cell, glucose gets phosphorylated by hexokinase to form glucose-6-phophate. Glucose-6-phosphate can then be used in four main different ways: (1) as an energy depot in form of glycogen (2) for the pentose-phosphate pathway to produce NADPH by building DNA or RNA (3) for energy demands during cytoplasmic glycolysis, which produces two pyruvate molecules and lactate without the need of oxygen (4) glycolysis followed by transportation of glycolytic end products into mitochondria, where the tricarboxylic acid (TCA) cycle and oxidative phosphorylation takes place to produce ATP under oxygen consuming conditions. Furthermore, not only in terms of oxygen shortage, glycolysis derived pyruvate as well as lactate can be shuttled out of the cell via monocarboxylate transporters (MCT) to provide metabolic coupling to neighboring cells e.g. axons. This process, called the “lactate shuttle”, was first described from astrocytes to axons, but later it has been postulated that also oligodendrocytes can supply the axon with lactate (Figure 4.1) (Fünfschilling et al., 2012; Pellerin and Magistretti, 1994).

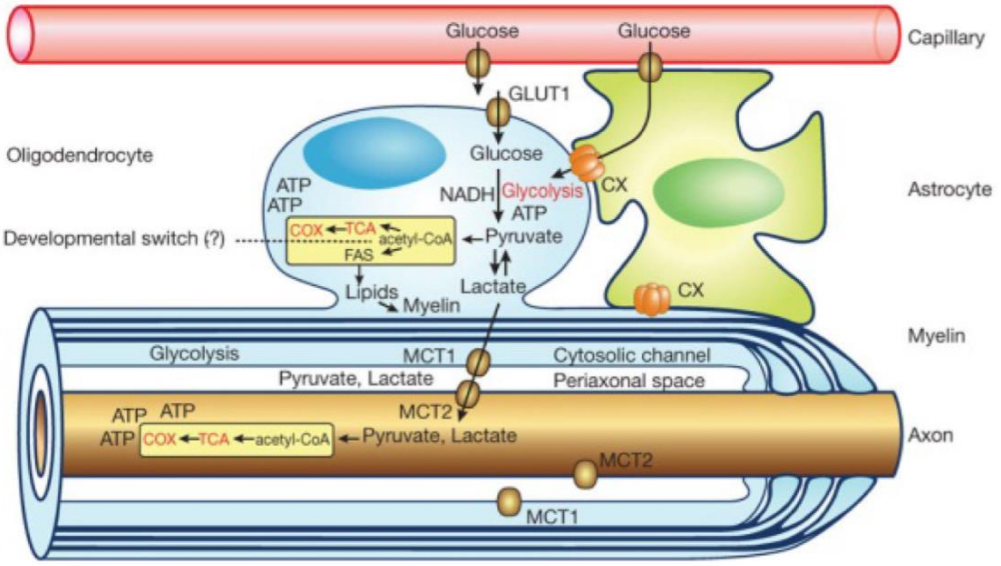

Figure 4.1I Model of neuronal metabolic support by oligodendrocytes. Glucose as the main fuel of the CNS is imported in oligodendrocytes via glucose transporter 1 (GLUT1) or through astrocytic connexins (CX) and gets integrated in glycolysis. Glycolysis derived lactate and pyruvate can be used in the tricarboxylic acid (TCA) cycle and oxidative phosphorylation (COX) for local adenosine triphosphate (ATP) production or upon axonal energy requirements they can be shuttled into the axon through the action of monocarboxylate transporters (MCT1,2) (taken from Fünfschilling et al., 2012).

4.1.2.2 Fatty acid metabolism

Already in the early 70th it was shown that fatty acids are able to enter the CNS (Dhopeshwarkar et al., 1971; Dhopeshwarkar and Mead, 1970, 1969). Fatty acids are actively transported via fatty acid transport proteins (FATPs) with FATP-1 and FATP-4 as the most abundant ones expressed in mice and human (Mitchell et al., 2011).

Besides glucose metabolism, the brain readily adapts to different metabolic conditions, by using circulating fatty acids for β-oxidation to comply energetic needs in the adult brain (Ebert et al., 2003; Romano et al., 2017). Once imported into the cytosol, fatty acids get activated via the fatty acyl-CoA synthetase to acyl-CoA and transported with a carnitine carrier system first into the outer mitochondrial membrane (carnitine palmitoyltransferase I (CPT-I)) followed by the inner (carnitine palmitoyltransferase II (CPT-II)), where the β-oxidation occurs. During β-oxidation, acyl-CoA is converted in a four step enzyme cascade to acetyl-CoA, which can directly be used in the TCA cycle or utilized in a reversed mechanism to build up fatty acids or cholesterol. To prohibit endless breakdown and rebuilding of fatty acids, the

transport of acyl-CoA into the outer mitochondrial membrane by the CPT-I, harbors a feedback loop by allosteric inhibition with malonyl-CoA, an intermediate in fatty acid synthesis.

4.1.3 Fatty acid and cholesterol synthesis

Despite the use of fatty acids as an energy source, the more common purpose is the synthesis of CNS sterols for the integration in membrane structures, especially myelin. Since the periphery is shielded from the CNS via the BBB, nutritional lipids enter the brain only in a limited manner. For example, phytosterols only account for >1% of adult CNS lipids (Jansen et al., 2006; Vanmierlo et al., 2012). Further it was shown that lipoproteins containing ApoE, the main carrier for cholesterol, are not able to enter the CNS (Linton et al., 1991).

The synthesis of fatty acids reached the highest capacity during myelination. Fatty acid synthesis takes place within the cytosol of the cell and includes a six-step mechanism. The rate limiting enzyme is acetyl-CoA carboxylase (ACC1) that converts acetyl-CoA into malonyl-CoA. In addition fatty acid synthases (FASN) catalyze the elongation of the fatty acid chain upon it reached the required carbon chain length. The chain length are classified in short-chain (<6 carbons), medium-chain (6-12 carbons), long chain (13-21 carbons), and very long-chain fatty acids (>21 carbons).

In the CNS cholesterol is synthesized locally by neurons and glia cells (Björkhem et al., 2004) (Figure 4.2). During myelination, mainly oligodendrocytes synthesize cholesterol. For cholesterol homeostasis, it has been claimed that astrocytes are the major source of CNS cholesterol (Pfrieger and Ungerer, 2011). Cholesterol homeostasis is highly regulated in the CNS, since blood-brain-barrier impairment increased both directions, import and export of cholesterol equally (Saeed et al., 2014). In the brain cholesterol is transported via lipoproteins, with the predominant one apolipoprotein E (ApoE). Import and export of ApoE bound cholesterol between different cell types of the brain is mediated via ATP-binding cassette (ABC) transporters (e.g. ABCA1, ABCG1) (Kim et al., 2008) and lipoprotein transporters such as LDL/ VLDL receptors during myelination (Zhao et al., 2007).

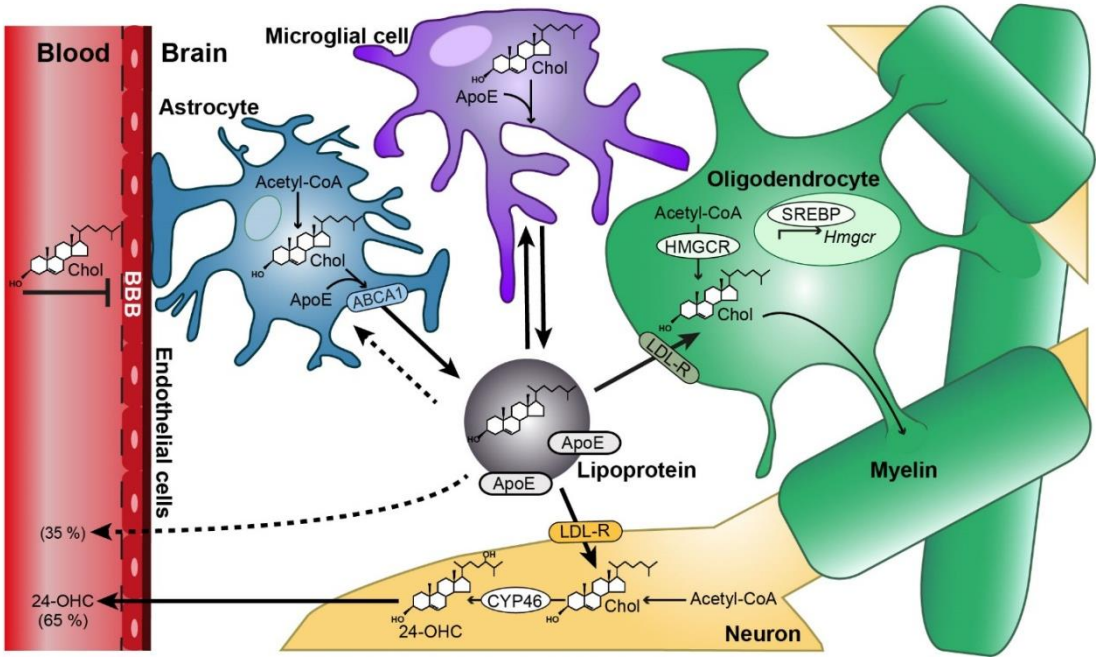

Figure 4.2l Cholesterol metabolism in the CNS. Since cholesterol is unable to cross the BBB, it is mainly synthesized locally in the CNS. All glia cells and neurons are able to synthesize cholesterol with 3-hydroxy-3-methyl-glutaryl-CoA reductase (HMGCR) as the rate-limiting enzyme. The expression of HMGCR is highly regulated by the transcription factor SREBP (sterol regulatory element-binding protein). In oligodendrocytes, cholesterol binds to proteolipid protein prior to the integration into the myelin sheath. ABC transporter (ABCA1) generate apolipoprotein E (ApoE) containing lipoproteins, the main cholesterol carrier within the CNS. Furthermore, cholesterol is highly reutilized with low-density lipoprotein receptors (LDL-R) responsible for endocytosis in oligodendrocytes and neurons. One major cholesterol excretion route is the hydroxylation to 24(S)-hydroxycholesterol (24-OHC) by cholesterol 24-hydroxylase (CYP46), but also another transport system has been postulated including ApoE (Xu, 2006) (modified from Saher and Stumpf, 2015).

The brain is able to turnover cholesterol to 24-hydroxycholesterol for excretion through the blood-brain-barrier and elimination by the bile. This step is catalyzed by the P450 enzyme (*Cyp46a1*), which was supposed to be mainly expressed in neurons (Lund et al., 1999; Smith et al., 1972), but new data revealed that further astrocytes and oligodendrocytes show a high expression (Zhang et al., 2014). Approximately two-thirds of brain cholesterol is excreted via this mechanism. The remaining third are supposed to be excretes through another pathway, which might involve of ApoE function (Saher and Stumpf, 2015; Xu, 2006).

4.1.4 Myelin

Highlighting the role of CNS sterols, one of the most important structure that is built up by lipids is the myelin membrane. Fast signal transduction of action potentials

consumes high amounts of axonal energy. Myelin, with its unique lipid composition increases membrane resistance and supports the axon with the insulation of a multilayered membrane stack. Axonal segments that are enclosed by myelin membranes comprises the internode, the adjacent juxtaparanodal region and the paranode. Myelin loops are anchored at the paranodes. The unmyelinated region between each axonal myelin segment are called nodes of Ranvier, which are highly enriched in voltage-gated sodium channels. These complex molecular organization allows rapid salutatory conduction of action potentials.

During myelination the newly formed myelin sheath is first assembled close to the axons inner tongue, followed by several wrapping steps from the inside to the outside (Snaidero et al., 2014) and later the compaction of the layers is achieved with the involvement of myelin proteins. The myelin sheath shows alternating structures of electron-dense and electron light layer, representing the major and minor dense lines inclosing cytoplasmic areas. The minor dense line is also called intraperiod line, since it displays the association of two myelin layers (Baumann and Pham-Dinh, 2001). The g-ratio, calculated by the ratio of fiber diameter divided by axon diameter, is a measure of myelin thickness for optimal conduction velocity. The optimum of conduction velocity was calculated as the g-ratio of 0.6-0.7, but further up to 0.8 was shown to provide effective insulation properties (Waxman, 1980).

4.1.4.1 Myelin lipids

CNS myelin contains high amounts of lipids with a dry weight of about 70%, including glycolipids (31%) and cholesterol (26%) (Chrast et al., 2011). The main components of myelin; cholesterol, phospholipids and glycosphingolipids are integrated in the myelin membrane in the ratio of 2:2:1 (O'Brien and Sampson, 1965). For cholesterol it was shown to be essential for myelin formation (Saher et al., 2005). Furthermore, myelin lipid and protein composition is highly conserved throughout species with an estimation of about 80% similarity between mice and humans (Gopalakrishnan et al., 2013). Despite the fact, that myelin lipids are important to sustain membrane fluidity, major interest focus on their role in distinctive membrane complexes, called membrane lipid rafts. Sphingolipids, cholesterol, and membrane proteins were shown to form these platforms to function in protein sorting, trafficking and signal transduction (London and Brown, 2000; Simons and Toomre, 2000).

4.1.4.2 Myelin-associated proteins

In addition to lipids, the myelin membrane contains different proteins, listed in descending order of abundance: MOG, MAG, CNP, MBP and PLP. The molecular function of the myelin oligodendrocyte glycoprotein (MOG) is so far unknown and it is of minor abundance in myelin (1%). It has been speculated, that it might be involved in the regulation of oligodendrocyte microtubule stability or in providing structural integrity by interacting with the cytoskeleton. Furthermore, it might support communication between myelin and the immune system (Johns and Bernard, 1999). Myelin-associated glycoprotein (MAG) belongs to the immunoglobulin superfamily and has with relatively low abundance (1%) in myelin. It is located at the periaxonal membrane along the inner myelin sheath, which emerged the assumption that MAG might function in axo-glia interaction (Martini and Schachner, 1988). Nevertheless, MAG-deficient mice only showed a minor delay in myelination, suggesting a compensatory mechanism (Montag et al., 1994). The biological function of the membrane interacting protein, 2',3'-cyclic nucleotide 3'-phosphodiesterase (CNP) remains so far elusive, since the substrate of the CNP enzyme is not located within the CNS. However, analysis of CNP knockout mice revealed normal myelin structure, but they develop severe axonal swellings resulting in axonal degeneration (Lappe-Siefke et al., 2003). These findings indicate a role of CNP in axo-glia support and axonal integrity. Myelin basic protein (MBP) constitutes with 8% as the second most abundant one in the CNS (Jahn et al., 2009). MBP functions in the adhesion of the different layers of the compact myelin. Furthermore MBP deficiency in mice led to the severely dysmyelinated phenotype of the “shiverer mouse”, with tremors, ataxia and acute seizures (Roach et al., 1983).

4.1.4.2.1 Proteolipid protein (PLP)

The *PLP1* gene encodes for proteolipid protein, which consists of 277 amino acids (30 kDa) and constitutes with ~17% the most abundant myelin protein in the CNS in mice (Jahn et al., 2009). PLP is a transmembrane protein of the myelin sheath, which upon splicing generates the 35bp smaller isoform DM20. PLP contains one intracellular and two extracellular loop regions. Both, the N- and the C-terminus protrude into the cytoplasm (Woodward, 2008). The extracellular loop contains two

disulfide bridges. Mutations disrupting these connections were shown to induce PLP endoplasmic reticulum (ER) retention and trigger the unfolded protein response (UPR) (Dhaunchak and Nave, 2007). *PLP1* is predominantly expressed in oligodendrocytes, especially during myelination. PLP protein synthesis takes place in the ER, in which PLP associates with cholesterol and is incorporated in membrane lipid raft domains in the secretory path (Krämer-Albers et al., 2006; Simons et al., 2000). After vesicular transport to the plasma membrane, PLP is finally integrated into the developing myelin sheath (Nussbaum and Roussel, 1983; Simons et al., 2000). PLP-deficient mice exhibit reduced cholesterol content in myelin membranes, highlighting the function of PLP in the enrichment of myelin cholesterol (Werner et al., 2013). Moreover, PLP-deficient mice show a condensed intraperiod line with reduced axonal conduction velocity, indicating that the extracellular structures of PLP function as a spacer between the single myelin layers (Boison and Stoffel, 1994). Furthermore, adult *Plp1* knock-out mice exhibit severe axonal swellings resulting in axonal degeneration (Klugmann et al., 1997). It has been postulated that PLP functions in the maintenance of axonal integrity (Garbern et al., 2002). Insight in PLP function to provide axonal integrity might be given by the finding that reduced N-acetyl-aspartate (NAA) levels were found in PLP-deficient mice and PMD patients (Garbern et al., 2002). NAA is synthesized in neuronal mitochondria and degraded by the enzyme aspartoacylase (ASPA), which is mainly expressed in oligodendrocytes. It has been postulated that neuronal-derived NAA is shuttled into oligodendrocytes to increase the expression of pro-myelination factors e.g. sphingomyelin synthesis (Singhal et al., 2017). A decreased level of NAA might indicate impaired axon-glia communication, which can affect axonal integrity.
Mutations, overexpression or loss of the *PLP1* gene (chromosome Xq22.2) cause the leukodystrophy Pelizaeus-Merzbacher Disease or the milder variant Spastic Paraplegia Type 2, respectively

4.1.5 Pelizaeus-Merzbacher Disease (PMD)

PMD is a severe and fatal leukodystrophy that currently lacks any therapeutic option. The incidence of PMD varies depending on demographic factors and ranges between 90.000 and 750.000 (Hobson and Kamholz, 1999). Typically men are affected and women are unaffected carriers, since the *PLP1* gene is located on the

X-chromosome. The symptoms of PMD include delayed motor and intellectual skills as well as tremor and spasticity. Furthermore, patients suffer from reduced white matter in the brain investigated by magnet resonance imaging (Wang et al., 1995). The clinical outcome of PMD varies from connatal severe forms with life expectancy of a few years to very mild PMD variants, such as Spastic Paraplegia Type 2 (SPG2). SPG2 is caused by deletion of the *PLP1* gene, and patients have a relatively normal life expectancy. Therefore, PMD pathology is rather caused by a "gain-of-function" effect than "loss-of-function", due to toxic accumulation of mutated or native PLP protein. Connatal forms of PMD are caused by a number of missense mutations or triplication of *PLP1*, whereas *PLP1* gene duplication accounts for the most common form of PMD, named classical PMD (Figure 4.3). Patients with classical PMD usually start to have symptoms within the first year of life and often fail to develop motor abilities, cognition and speech. With constant care, physiotherapy and slowed disease progression in adulthood, their survival extends often until the sixths decade (Woodward, 2008).

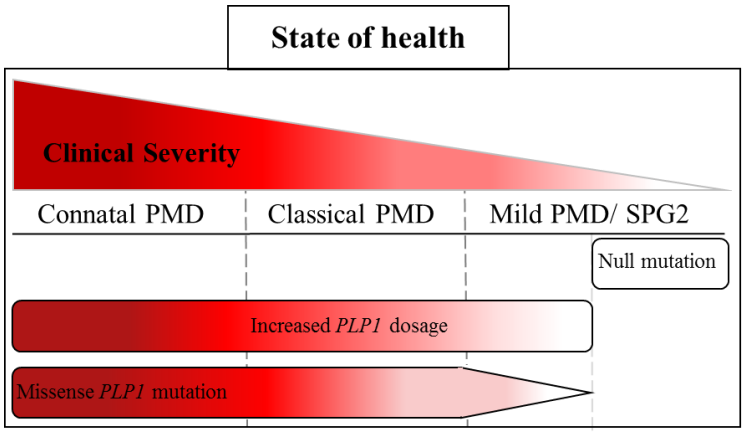

Figure 4.3l Classification of PMD according to clinical severity. The most severe cases of PMD (Pelizaeus-Merzbacher disease) are summarized by the term connatal PMD, which comprises highly increased *PLP1* dosages and severe missense mutation. The classical PMD that represents the most common form, includes *PLP1* duplication as well as mild missense mutations. Spastic paraplegia type 2 (SP2) describes the mildest form of PMD, which comprises null mutations, but also modest increase in gene dosage or mutations with unaffected PLP function (adapted from Yamamoto and Shimojima, 2013).

4.1.5.1 Mouse models of PMD

To date several mouse models mimicking diverse states of PMD pathology have been generated with distinct characteristics regarding the impact on oligodendrocyte function and axonal impairments. As already mentioned above, *Plp*1 null mice first

accomplish relatively normal myelin formation, but later they develop myelin outfoldings and highly severe axonal impairments (Boison and Stoffel, 1994; Klugmann et al., 1997). Mouse models for the most severe clinical outcome, the congenital PMD, include the naturally occurring *jimpy* and *rumpshaker* mouse lines. *Jimpy Plp1* contains a 74-nucleotide deletion in *Plp1* mRNA, resulting in a frameshift that causes the lack of the fourth PLP transmembrane domain (Nave et al., 1987, 1986). The milder *rumpshaker Plp1* mutant shows an amino acid substitution (Ile186Thr) (Griffiths et al., 1990). It was shown that PLP is a cholesterol binding protein mislocalized in *Plp1* transgenic and *Plp1* mutant mice (Krämer-Albers et al., 2006; Simons et al., 2002). PLP/DM20 misfolding, retention, missorting, and toxicity are relevant PMD disease mechanisms (Dhaunchak and Nave, 2007; Dhaunchak et al., 2011; Schneider et al., 1995) that apply to overexpressed PLP as well as PLP mutants. Toxicity is caused by accumulation of mutant as well as high amounts of native PLP protein, which leads to e.g. impaired trafficking of PLP and cholesterol to the plasma membrane (Saher et al., 2012).

The PLP *jimpy* mutant gets misfolded and retained in the ER provoking a strong unfolded protein response and ER stress (Gow et al., 1998, 1994; Swanton et al., 2005), whereas some *rumpshaker* PLP reaches the plasma membrane, also correlating with its residual ability to associate with cholesterol (Krämer-Albers et al., 2006). These results are supported by the finding that in PMD mutant mice the ER stress response correlates with the disease state (Southwood et al., 2002). Mouse models for *Plp1* overexpression include the Plp-tg$^{66/66}$ (seven copies) and Plp-tg$^{72/72}$ (three copies) mouse lines (Readhead et al., 1994) as well as the Plp (+ four copies) and Plp (+ two copies) mouse lines (Kagawa et al., 1994). The number of integrated transgene copies reflects disease progression including myelination state, oligodendrocyte and axonal loss as well as life expectancy, which is comparable to patients (Wolf et al., 2005).

4.1.5.1.1 Plp-tg$^{72/72}$ mouse line

During this study the Plp1-tg$^{72/72}$ transgenic mouse was used, which contains three copies of the *Plp1* transgene (Readhead et al., 1994). Plp1-tg$^{72/72}$ provides an accurate mouse model for classical PMD, since *Plp1* overexpression reflects a two-fold increase in protein abundance, which is comparable to PMD patients. The mice are highly dysmyelinated with ongoing demyelination in optic nerve, spinal cord and

brain. Together with strong inflammatory responses and oligodendrocyte loss these mice develop axonal degeneration (Readhead et al., 1994). On the behavioral level the mice exhibit severe motor impairments and acute seizures (Edgar et al., 2010; Karim et al., 2010). In *Plp1*-transgenic oligodendrocytes it was shown that PLP overexpression causes the accumulation of PLP and cholesterol in the late endosome/ lysosome, which leads to decreased levels of plasma membrane cholesterol (Saher et al., 2012; Simons et al., 2002). In a treatment approach, supplementation of dietary cholesterol rescued the PMD pathology in Plp1-tg$^{72/72}$ mice (Saher et al., 2012). The mice showed an increase in myelin content in optic nerve and spinal cord. Furthermore, cholesterol treatment reduced intracellular PLP/cholesterol accumulation in mutant oligodendrocytes, and secondary inflammation as well as motor defects were restored. A compromised blood-brain barrier of mutants served as prerequisite for the treatment approach, since cholesterol, which is normally shielded from the CNS, entered the brain and improved the balance between PLP and cholesterol. In two other studies, it was shown that curcumin treatment decreased oxidative stress levels and inflammation in Plp-tg mice by lowering glutathione levels and Lonaprisan administration (progesterone antagonist) targeted *Plp1* mRNA expression thereby decreasing the level of *Plp1* from 1.8 to 1.5 fold in brain tissue (Epplen et al., 2015; Prukop et al., 2014).

4.1.6 Ketogenic diet

The ketogenic diet (KD) is based on a ratio of high fat, low carbohydrates and sufficient protein, to reprogram the body to metabolize fats for energy requirements instead of carbohydrates. Ketone bodies are comprised by three compounds: β-hydroxybutyrate, acetoacetate and acetone, with the latter being less important as energy source. Ketone bodies are produced by fatty acid oxidation in the liver. They can enter the CNS via monocarboxylate transporters (MCT) and be integrated in local metabolism (Figure 4.4).

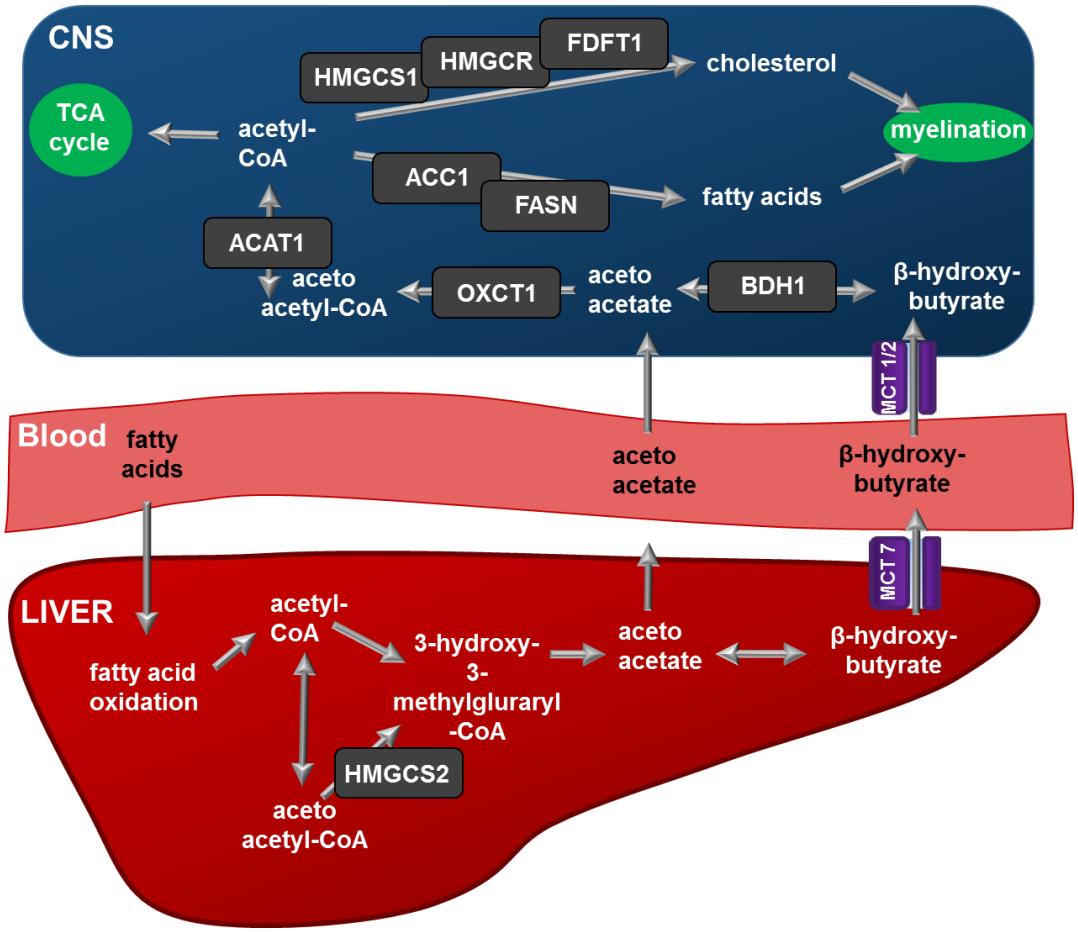

Figure 4.4l Model of metabolic support of ketone bodies. Fatty acids in the blood stream enter the liver and are converted to ketone bodies by fatty acid oxidation. The conversion of fatty acids into acetoacetate requires the enzyme 3-hydroxy-3-methylglutaryl-CoA synthase 2 (HMGCS2). Ketone bodies can be transported by monocarboxylate transporters (MCT1,2 or 7). The three enzymes involved in ketolysis are 3-hydroxybutyrate dehydrogenase 1 (BDH1), 3-oxoacid CoA-transferase 1 (OXCT1) and acetyl-coA acetyltransferase 1 (ACAT1) leading finally to acetyl-CoA production. Acetyl-CoA can be used in the tricarboxylic acid (TCA) cycle or to build-up fatty acids and cholesterol involving the following selected enzymes: 3-hydroxy-3-methylglutaryl-CoA synthase 1 (*HMGCS1),* 3-hydroxy-3-methylglutaryl-CoA reductase (*HMGCR*), farnesyl-diphosphate farnesyltransferase also referred to as squalene synthase (FDFT1), acetyl-CoA-carboxylase (ACC1), fatty acid synthases (FASN β-hydroxybutyrate dehydrogenase 1.

MCT1 is mainly expressed by astrocytes and endothelial cells. Whereas MCT2 was predominantly expressed by neurons, but also oligodendrocytes and microglia revealed MCT2 expression (Pellerin et al., 2005; Zhang et al., 2014). Once ketone bodies were imported into cells of the CNS, BDH1 interconverts β-hydroxybutyrate to acetoacetate. OXCT1, the rate-limiting enzyme of ketolysis, converts acetoacetate to aceto-acetyl-CoA. ACAT1 facilitated the reaction of aceto-acetyl-CoA to two molecules of acetyl-CoA. Acetyl-CoA can be used for example as energy source in the TCA cycle or utilized to synthesize fatty acids or cholesterol, but further many other metabolic pathways of acetyl-CoA are possible. In newborn rodents, which rely on the maternal, ketone body rich milk as food source, ketone bodies provide ~ 30%

of the brains energy requirements (Cremer, 1982). This proportion decreases drastically after weaning, which might reflect reduced activity of the main enzymes for ketone body lysis, BDH1 (β-hydroxybutyrate dehydrogenase 1), OXCT1 (3-oxoacid CoA-transferase 1) and ACAT1 (acetyl-CoA acetyltransferase 1). (Krebs et al., 1971). It was shown that in young rodents, ketone bodies are used to synthesize lipids and especially cholesterol, which is predominantly integrated in the myelin sheath (Koper et al., 1981). Furthermore, ketone bodies as metabolites were proven to be the main supplier of lipid and cholesterol synthesis, even in the presence of sufficient glucose (Webber and Edmond, 1977). A benefit for lipid synthesis by ketone bodies compared to glucose might be that aceto-acetyl-CoA, which is produced during ketolysis can be directly integrated in fatty acid synthesis. In contrast glycolytic derived acetyl-CoA must first be converted to aceto-acetyl-CoA (Morris, 2005).

4.1.6.1 Treatment potential of the ketogenic diet

In the early 1920s the ketogenic diet was developed and first applied in the treatment of epilepsy (Liu et al., 2018). Since then, researchers in a broad field of neurological related diseases discovered the potential of the ketogenic diet, but so far little is known about the function of KD. Hereafter, I summarize interesting findings providing insight in the neuroprotective role of ketone bodies

Treatment of KD in epilepsy provided anticonvulsant and anti-epileptogenic properties (Liu et al., 2018). In a clinical treatment trial of childhood epilepsy with KD it was shown that two-third of the children treated with KD had a seizure reduction of 50-90% (Neal et al., 2008). Direct mechanistic insight of KD action in epilepsy and seizure control is unknown, but it has been speculated that a combination of enhanced ketosis, reduced glycolysis and increased amounts of fatty acids leads to a metabolic switch which induces neuroprotection. Mechanisms that might be involved in KD neuroprotection include an increase in oxidative phosphorylation and enhanced mitochondrial biogenesis which can causes reduction of reactive oxygen species (ROS) (Bough and Rho, 2007). Furthermore, impact of KD function on the reduction of mitochondrial oxidative stress release might be provided by the fact that elevated amounts of fatty acids induce the expression of mitochondrial uncoupling proteins (UCP) via induction of PPARα (Masino and Rho, 2012). UCPs function via

upregulation of mitochondria biogenesis, control of calcium flux and reduce free radical formation (Andrews et al., 2005). The results are supported by KD fed mice, which showed increased abundance of cerebral UCPs associated with reduced ROS levels (Sullivan et al., 2004). Moreover, KD treatment has been postulated to ameliorate mitochondrial dysfunction. In a therapeutic approach, mice treated with MPTP (1-methyl-4-phenyl-1,2,3,6-tetrahydropyridine), which blocks mitochondrial complex I of the electron transport chain, were supplied with D-β-hydroxybutyrate infusion (Abou-Sleiman et al., 2006). Interestingly, neurons of D-β-hydroxybutyrate treated mice were protected from the neurotoxin. Further in vivo studies in cultured neurons provided evidence that D-β-hydroxybutyrate functions by elevating oxidative phosphorylation of mitochondria in a complex II dependent manner (Tieu et al., 2003). Besides the neuroprotective function of KD, another study provided insight in the anti-inflammatory role of ketone bodies by decreasing pro-inflammatory cytokines (Yang and Cheng, 2010).

In summary, KD provided anticonvulsant and anti-inflammatory properties, increased oxidative phosphorylation and reduced oxidative stress in mitochondria. Furthermore, the metabolic switch induced by KD treatment might enhance myelination due to fact that ketone bodies are predominantly used for the synthesis of fatty acids and especially cholesterol (Webber and Edmond, 1977). These findings could be of great interest for the treatment of neurodegenerative diseases associated with hypomyelination and mitochondrial malfunctions such as PMD.

4.1.7 Aim of the study

PMD is a fatal leukodystrophy with a lack of efficient therapeutic options. A previous therapeutic approach used the compromised blood-brain barrier of mutant Plp1-tg$^{72/72}$ mice for dietary cholesterol supplementation, which rescued PMD pathology (Saher et al., 2012).

The aim of this study was to analyze a new treatment approach of the Plp1-tg$^{72/72}$ mice by feeding a ketogenic diet to support endogenous CNS lipid homeostasis independent of blood-brain barrier alterations, since it is unknown whether PMD patients suffer from increased permeability. Our experimental design was based on the fact that ketone bodies are predominantly used for the synthesis of fatty acids and cholesterol. We speculated that this preference would lead to a benefit for Plp-

tg$^{72/72}$ mice, since an increase in local abundance of cholesterol together with fatty acids might further enhance myelin synthesis. In addition, all glia cells and neurons of the central nervous system can take up ketone bodies and utilize them as metabolites. Due to the severe loss of oligodendrocytes in Plp-tg$^{72/72}$ mice, oligodendrocytic support of axons is highly impaired. Therefore, we hypothesized that increased ketone body utilization might provide a direct or indirect support for axons to cover their local energy requirements.

In this study, ketogenic diet (KD) was fed from 2 until 12 weeks of age to investigate the impact on inflammation, oligodendrocyte numbers, myelination, axonal pathology and motor phenotype of PLP-tg$^{72/72}$ mice. Furthermore, metabolic changes in spinal cord tissue of PLP-tg$^{72/72}$ mice caused by stimulated ketone body metabolism were analyzed.

With our experimental approach we wanted to address the questions whether KD (1) can reduce CNS inflammation (2) increases oligodendrocyte numbers (3) enhances myelination (4) ameliorates the affected motor phenotype (5) alters ketone body and accordingly glucose metabolism within the CNS (6) decreases ER and lysosomal PLP accumulation and therefore reduces ER stress and further (7) ameliorates axonal pathology.

4.2 Results

4.2.1 Phenotypical change of Plp-tg mice

Classical Pelizaeus-Merzbacher disease (PMD) is a severe leukodystrophy that is mainly caused by increased gene dosage of the myelin protein PLP1. For this study the Plp1 transgenic mouse line 72 (Readhead et al., 1994), which harbor three copies of the *Plp1* gene resulting in an about two-fold overexpression, was used. These mice are further referred to as Plp-tg mice. In a novel therapeutic approach, it was possible to ameliorate disease severity in the transgenic mouse model by feeding a high cholesterol diet (Saher et al., 2012). Cholesterol in the circulation was able to pass the BBB, due to compromised BBB function.

The original aim of this study was to further define the potential of dietary cholesterol as a treatment option of PMD, but unexpectedly Plp-tg mice developed changes in pathology. In 2014, the entire mouse colony suffered from a wide-spread infection of mites and helminthes, which was treated with the standard treatment MiteArrest, Fenbendazol and Ivermectin. Despite the successful elimination of the infection, this treatment also strongly reduced breeding performance and diminished early postnatal survival of litters. Moreover, routinely monitored Plp-tg mice on standard diet after termination of the anti-infective treatment (further referred to as Plp-tg 2014) had improved in some features typical for PMD pathology. The newly patho-phenotype showed increased mean body weight reaching wildtype levels (23.1±0.4g body weight in 2012 prior to infection compared to 26.1±0.7 in 2014 after treatment). Backcrossing the line on the C57BL6/N genetic background (Plp-tg 2015) did not re-establish the previously observed reduced body weight (Figure 4.5a). Plp-tg mice as well as PMD patient suffer from acute seizures and impaired motor function (Edgar et al., 2010; Karim et al., 2010; Saher et al., 2012). Therefore, the altered patho-phenotype was further characterized by the elevated beam test which assesses motor coordination and balance. Mice walk on an elevated narrow beam into a save box. The number of paw slips that occur during this process is quantified. In accordance with the normalized body weight, Plp-tg mice in 2014 showed significantly improved motor function when compared to cohorts from 2012 (Figure 4.5b). Gliosis and inflammation are also hallmarks of PMD pathology in patients and mouse models.

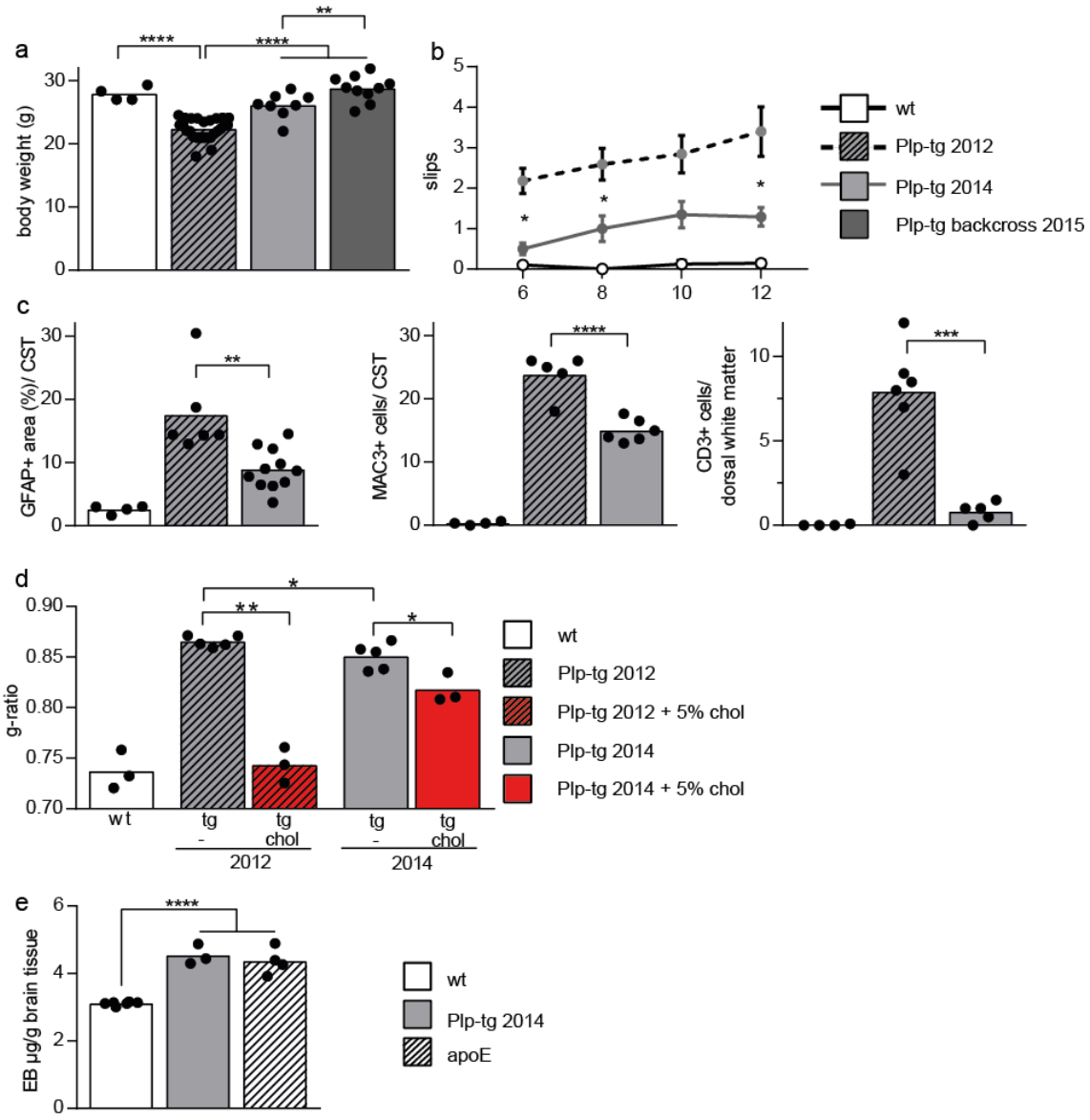

Figure 4.5| Plp-tg mice developed phenotypical changes. (a) Body weight at twelve weeks of age of non-transgenic wildtype, Plp-tg mice in 2012, 2014 and after backcross in 2015. One-way-ANOVA with Tukey's multiple comparison test was performed. **(b)** Motor performance assessed by the elevated beam test comparing the number of slips between non-transgenic wildtype (n=8), untreated Plp-tg mice in 2012 (n=19) and in 2014 (n=12). Two-way-ANOVA with Bonferroni's post test revealed significant differences between Plp-tg mice in 2012 and 2014. **(c)** Histological evaluation of wildtype controls and Plp-tg mice in 2012 and 2014, showing the number of activated microglia/macrophages (MAC3) (n=4-6), and reactive astrocytes (GFAP) (n=4-11) in the CST, and CD3+ T cells (n=4-6) in the dorsal white matter of the spinal cord. Three sections per animal were staining for quantification. One-way-ANOVA followed by Tukey's multiple comparison test in 2012 compared to mice from the 2012. **(d)** G-ratio analysis in the CST of non-transgenic wildtype compared with untreated Plp-tg versus treated mice (5% cholesterol supplementation to standard chow) assessed in 2012 (n=3-5) and 2014 (n=3-5). Student's t-test was performed on the g-ratio measurement of Plp-tg mice in 2014 in comparison to 2012. **(e)** Evans Blue extravasation assay for the measurement of BBB permeability in non-transgenic wildtype mice (n=6) compared to Plp-tg in 2014 (n=3). ApoE KO (n=4) mice served as positive control. One-way-ANOVA with Tukey's multiple comparison test. Differences were considered significant with a P-value of *, P<0.05; **, P<0.01; ***, P<0.001; ****, P<0.0001.

To determine whether also reduced inflammation contributed to the ameliorated phenotype, Plp-tg mice at the age of 12 weeks were re-evaluated histologically. Plp-tg mice in 2014 improved in all tested parameters in comparison to previous cohorts, showing strongly diminished microgliosis (MAC3+), astrogliosis (GFAP+) and T-cell infiltration (CD3+) (Figure 4.5c).

It is conceivable that the infection as well as the anti-mite/helminths treatment favored the selection of the fittest Plp-tg mice, but also an unspecific genetic drift could explain the improved phenotype of untreated Plp-tg mice. Particularly, loss of one transgene copy could have led to less severe *Plp1* overexpression, leading to the ameliorated disease expression in Plp-tg mice. Therefore, the level of *Plp1* mRNA overexpression in brain lysates was determined at the age of 13 weeks. In the brain of Plp-tg mice, a 1.8-fold overexpression of PLP was detectable in 2016 (Dr. Theresa Kungl, Dr. Thomas Prukop personal communication), which is in accordance with published data (Prukop et al., 2014), indicating unaltered genetic expression of *Plp1* in 13 weeks old mice.

The primary defect of Plp-tg mice is the severe hypomyelination. Therefore, the thickness of myelin sheaths was assessed by g-ratio analysis of the corticospinal tract (CST) in wildtype and Plp-tg (Figure 4.5d). Reflecting the overall ameliorated pathology pf Plp-tg mice in 2014, hypomyelination of Plp-tg slightly but significantly improved. Previously, a remarkable therapeutic benefit was observed by feeding a cholesterol-rich diet to Plp-tg mice that reached g-ratio levels comparable to wildtype mice (Saher et al., 2012). When testing the efficacy of dietary cholesterol supplementation on myelin thickness in the Plp-tg mouse line from 2014, Plp-tg mice significantly increased myelination in response to cholesterol as before; however, the degree of amelioration was strongly reduced compared to cohorts from 2012 (Figure 4.5d).

The impairment of the BBB is a prerequisite for peripheral cholesterol to enter the CNS and to ameliorate pathology in Plp-tg mice (Saher et al., 2012). To address the question, whether changes in BBB integrity contributed to the observed reduction in treatment efficacy of dietary cholesterol, the permeability of Plp-tg mice was quantified as described previously (Berghoff et al., 2017a). However, when measuring Evans blue extravasation in brain lysates, Plp-tg mice showed increased permeability of the BBB (Figure 4.5e) to a degree which is comparable to ApoE null mice, as shown previously (Saher et al., 2012). These results suggest that altered

BBB properties do not account for the altered treatment efficacy of dietary cholesterol supplementation.

4.2.2 Development of new treatment strategies in Plp-tg mice

Ketone bodies were shown to be predominantly used for the synthesis of fatty acids and especially cholesterol, even in the presence of high glucose (Webber and Edmond, 1977). This preference could lead to a benefit for Plp-tg mice, since they exhibit severe hypomyelination and an increase local abundance of fatty acids and cholesterol might enhance myelin synthesis. Therefore, we decided to test a new treatment approach, by feeding other lipid based diets to Plp-tg mice. High fat diets increase the abundance of free fatty acids in the blood stream, which are converted by the liver to ketone bodies. Endothelial cells at the BBB express monocarboxylate transporter 1 (MCT1) which mediates the transport of ketone bodies across the BBB. In the CNS, glia cells and neurons express different MCTs for the import of ketone bodies (or others e.g. lactate) to use them as an energy source. The advantage of ketone bodies to be directly transported across the BBB provides the main benefit for PMD patients, since it is unknown whether PMD patients suffer from increased BBB permeability as it was shown for the Plp-tg mouse model in 2012 (Saher et al., 2012).

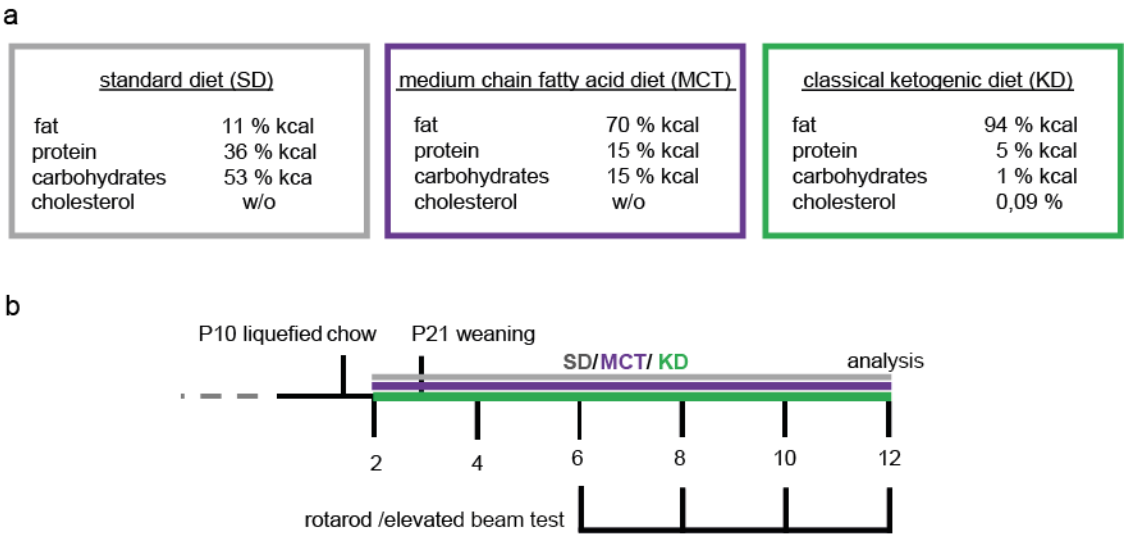

Figure 4.6| Treatment paradigm for lipid supplementation. (a) Composition of standard chow (SD), medium chain fatty acid diet (MCT) and classical ketogenic diet (KD). **(b)** Treatment scheme showing the treatment duration either with SD, MCT or KD. Additionally, time points of rotarod and elevated beam test performance as well as endpoint analysis are indicated.

For our treatment studies we decided to use the following diets: standard diet (SD, 11% fat), medium chain triglyceride diet (MCT, modified Surwit with 43% fat content) and classical ketogenic diet (KD, ketogenic diet with 80% fat content) (Figure 4.6a). Young mice during lactating phase highly express important enzymes for ketone body utilization (Krebs et al., 1971). To prevent the naturally occurring switch from ketone body usage to mainly glucose metabolism, ketogenic diet was provided already during lactating phase at two weeks of age until endpoint analysis with twelve weeks (Figure 4.6b). Motor performance was monitored by the elevated beam test and rotarod every other week between 6 to 12 weeks of age. The mice were weaned with three weeks of age.

4.2.3 Unaltered physiological parameters in MCT fed Plp-tg mice

Medium chain triglycerides were shown to facilitate ketone body production compared to long chain triglycerides, which are the main constituent of the classical ketogenic diet (Huttenlocher et al., 1971). Therefore, a MCT diet regime allows a higher intake of carbohydrates and proteins, facilitating digestion with a similar synthesis rate of ketone bodies in epileptic patients (Sills et al., 1986). To determine diet induced metabolic changes as a measure of liver ketogenesis, glucose and β-hydroxybutyrate levels in blood samples were analyzed (Figure 4.7a). In contrast to patients with epilepsy (Huttenlocher et al., 1971), blood concentration of β-hydroxybutyrate during MCT diet increased only slightly and blood glucose was not altered as expected (Eckel et al., 1992). Furthermore, evaluating motor performance on the elevated beam test revealed unaltered motor function in Plp-tg mice fed MCT diet (Figure 4.7b). Due to the small treatment benefit of MCT diet, the MCT treatment of Plp-tg mice was discontinued and we focused on the classical ketogenic diet.

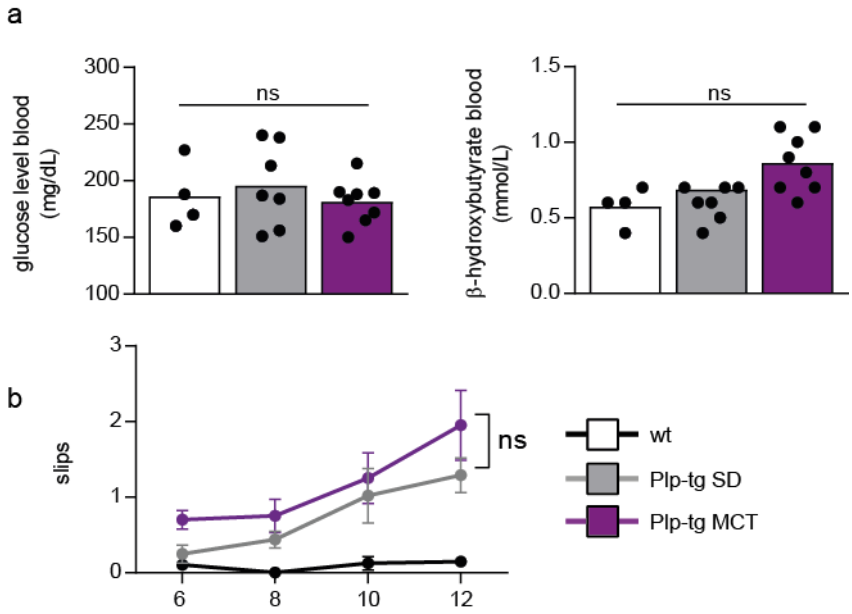

Figure 4.7l MCT diet revealed unaltered motor performance in Plp-tg mice. (a) Evaluation of glucose and β-hydroxybutyrate level in blood samples taken from the tail tip of non-transgenic wildtype, Plp-tg mice fed SD or MCT diet. One-way-ANOVA with Tukey's multiple comparison test was performed (n=4-8). **(b)** Elevated beam test as a measure of motor performance was done with wildtype and Plp-tg mice fed SD or MCT diet (n=4-8). Results were unaltered and therefore assigned not significant (ns).

4.2.4 Increase ketone body metabolism in Plp-tg mice fed KD

Since classical KD provides 94% kcal as fats compared to 70% kcal in the MCT diet (Figure 4.6a), a stronger change in physiological parameters reflecting enhanced ketogenesis was expected. Hence, blood β-hydroxybutyrate, blood glucose (Figure 4.8a) and body weight (Figure 4.8b) were monitored weekly. β-Hydroxybutyrate levels stayed persistently increased through the entire treatment period (Mean of 3-12 weeks of age for Plp-tg 0.63±0.04mg/dL on SD compared to 5.76±0.18 on KD). A strong reduction in blood glucose was determined one week after treatment start, at three weeks of age. Interestingly, blood glucose normalized during the ten weeks' treatment period (Plp-tg 3 weeks of age 139.5±15.89mg/dL SD compared to 95.33±9.11 KD; 12 weeks of age 200.8±7.87mg/dL SD compared to 154.2±13.96 KD). The increase in blood β-hydroxybutyrate as well as the decrease in blood glucose was expected (Mantis et al., 2014). Despite the expected observation that KD led to a strong reduction in the gain of body weight (Plp-tg 12 weeks of age 16±1g KD in comparison to 26±1 SD), mice appeared healthy and lively in accordance with other studies (Schnyder et al., 2017). Furthermore, these findings are supported by

unaltered serum pH (Figure 4.8c), which indicates that Plp-tg mice on KD did not suffer from ketoacidosis. Plp-tg mice fed KD revealed a persistent and reliable alteration of metabolism without any concerns about the safety and tolerability of KD. This provided the prerequisite for the analysis of a potential KD treatment benefit for Plp-tg mice.

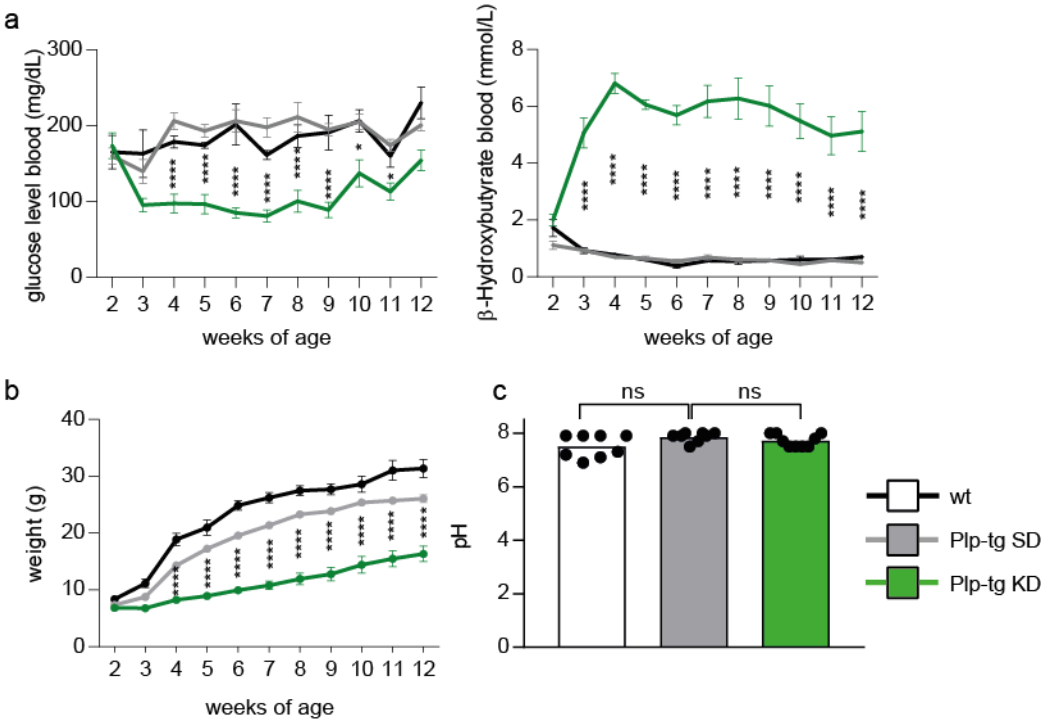

Figure 4.8l KD highly increased ketone body abundance in the blood of Plp-tg mice. (a) Blood glucose and β-hydroxybutyrate levels measured in non-transgenic wildtype and Plp-tg mice fed SD or KD. Two-way-ANOVA with Bonferroni's post test revealed significant difference between Plp-tg mice fed SD or KD. **(b)** Body weight of Plp-tg animals fed KD compared to SD fed littermate controls. Quantification was performed by two-way-ANOVA with Bonferroni's post test. (c) Serum pH at 12 weeks of age in wildtype and Plp-tg mice fed SD or KD. Differences were considered significant with a P-value of *, P<0.05; ****, P<0.0001.

4.2.5 Plp-tg mice fed KD show reduced markers for microgliosis, but not astrogliosis

Marked inflammatory responses are associated with disease expression in Plp-tg mice, including microgliosis and astrogliosis (Epplen et al., 2015; Prukop et al., 2014; Saher et al., 2012).

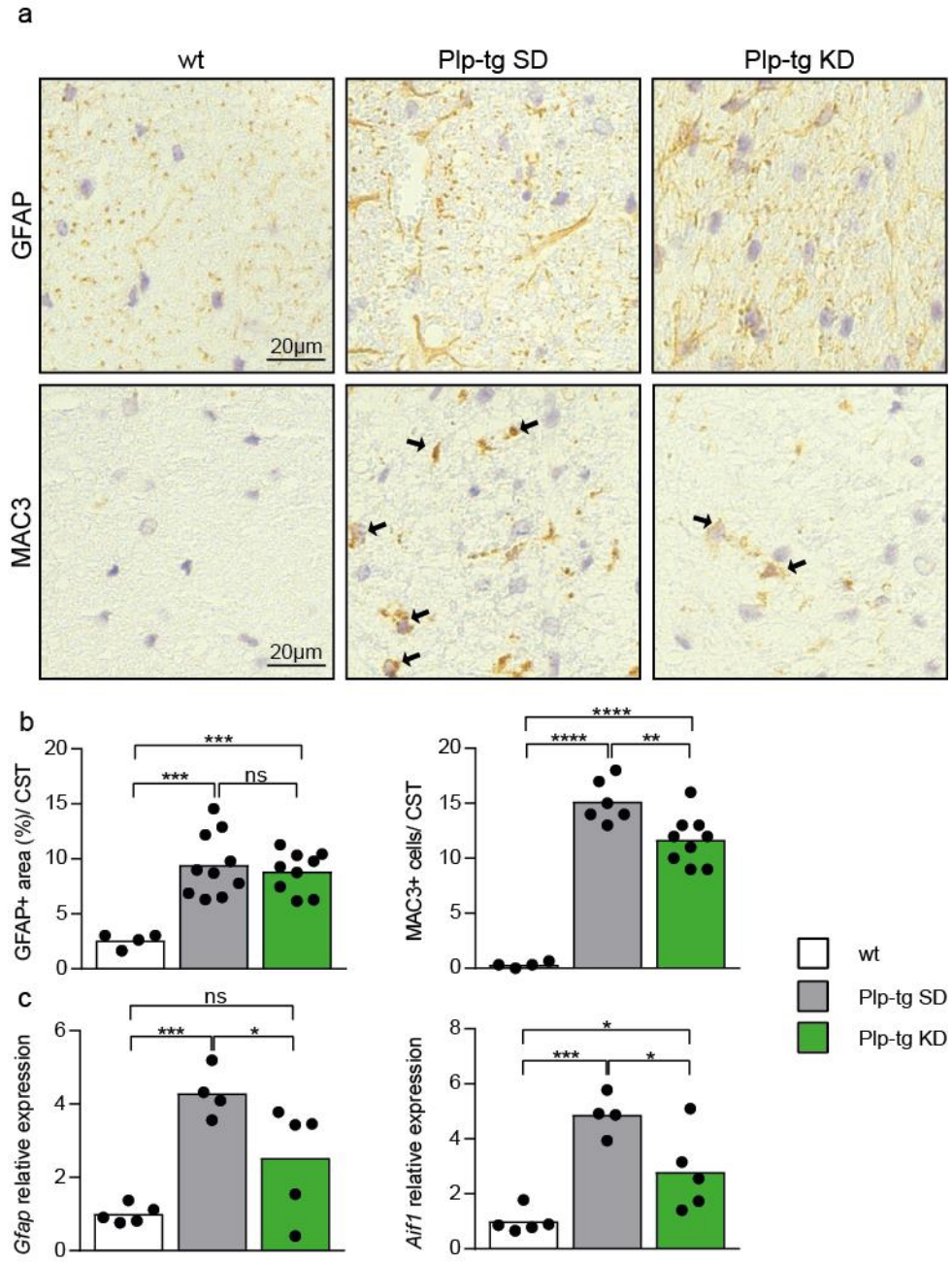

Figure 4.9l Reduced microgliosis and unaltered astrogliosis in Plp-tg animals. (a) GFAP and MAC3 stainings in the CST of non-transgenic wildtype, Plp-tg mice on SD and KD. **(b)** Histological evaluation showing the number of activated microglia (MAC3) (n=4-6), and the GFAP positive area for reactive astrocytes in the CST of wildtype and Plp-tg mice (n=4-11). One-way-ANOVA with Tukey's multiple was performed. **(c)** Normalized quantitative RT-PCR on dissected lumbar spinal cord tissue determining the marker genes for activated microglia (*Aif1*) and reactive astrocytes (*Gfap*). One-way-ANOVA with Tukey's multiple comparison test revealed differences for Plp-tg mice on SD compared to KD. (P-values of *, P<0.05; **, P<0.01; ***, P<0.001; ****, P<0.0001; ns = not-significant, scale bar, 20µm).

To address, whether KD leads to reduced inflammation in Plp-tg mice, we evaluated astrogliosis with the use of a marker for reactive astrocytes, GFAP (glial fibrillary acidic protein). Furthermore, microgliosis was analyzed in Plp-tg mice by using

immunohistochemistry staining for MAC3 (macrophage-3 antigen) which stains activated, including phagocytic, microglia.

Quantification of astrogliosis in Plp-tg mice fed SD revealed a strong GFAP positive signal in the cortical spinal tract (CST) (Figure 4.9a). Interestingly, Plp-tg mice fed KD showed unaltered astrogliosis, indicated by comparable GFAP positive area to SD littermates (Plp-tg mice: 9.5±0.91 $GFAP^+$ area SD compared to 8.9±0.62 KD) (Figure 4.9b). However, an about 50% reduction of *Gfap* expression (Figure 4.9c) in whole lumbar spinal cord lysates including further grey matter parts suggests decreased astrogliosis.

Histological quantification of microgliosis in the CST of Plp-tg mice revealed a significant increase in MAC3 positive cells in Plp-tg mice fed SD compared to wildtype controls (Figure 4.9a). Feeding KD strongly reduced microgliosis (Plp-tg mice: 15.2±0.79 $MAC3^+$ cells SD compared to 11.7±0.75 KD in the CST) (Figure 4.9b). The reduced microgliosis in KD fed Plp-tg mice was further supported by 50% decreased mRNA expression of the microgliosis marker *Aif1* (allograft inflammatory factor 1) (Figure 4.9c). These data suggest that KD led to ameliorated gliosis in Plp-tg mice. Furthermore, astrogliosis was shown to be highly persistent at the twelve weeks' time-point, indicating that KD treatment did not influence the number of activated astrocytes.

4.2.6 Increased oligodendrocyte numbers in KD fed Plp-tg mice

Oligodendroglial differentiation is characterized by the expression of marker proteins. Immature oligodendrocytes, named oligodendrocyte precursor cells (OPC's) synthesize NG2 (nerve-glia antigen 2 proteoglycan), whereas mature oligodendrocytes express CAII (carbonic anhydrase II). Olig2 (oligodendrocyte lineage transcription factor 2) is expressed by the complete oligodendroglial lineage. The demyelinating and dysmyelinating pathology of Plp-tg animal includes the early loss of oligodendrocytes (Readhead et al., 1994). This defect is supposedly paralleled by enhanced OPC differentiation in the attempt to maintain functionality. To test whether KD treatment of Plp-tg mice might influence the abundance of oligodendroglia, we performed histologically analyses with stainings detecting NG2, CAII and Olig2 in the CST of Plp-tg mice (Figure 4.10a). Quantification of NG2 positive cells in the CST revealed a strong increase in OPC numbers in Plp-tg mice

on SD and a further elevation when feeding the KD (WT: 5.6±0.43 $NG2^+$ cells; Plp-tg mice: 10.2±0.37 SD compared to 12.2±0.49 KD). The CAII staining showed highly reduced numbers of mature oligodendrocytes in Plp-tg mice on SD compared to wildtype mice.

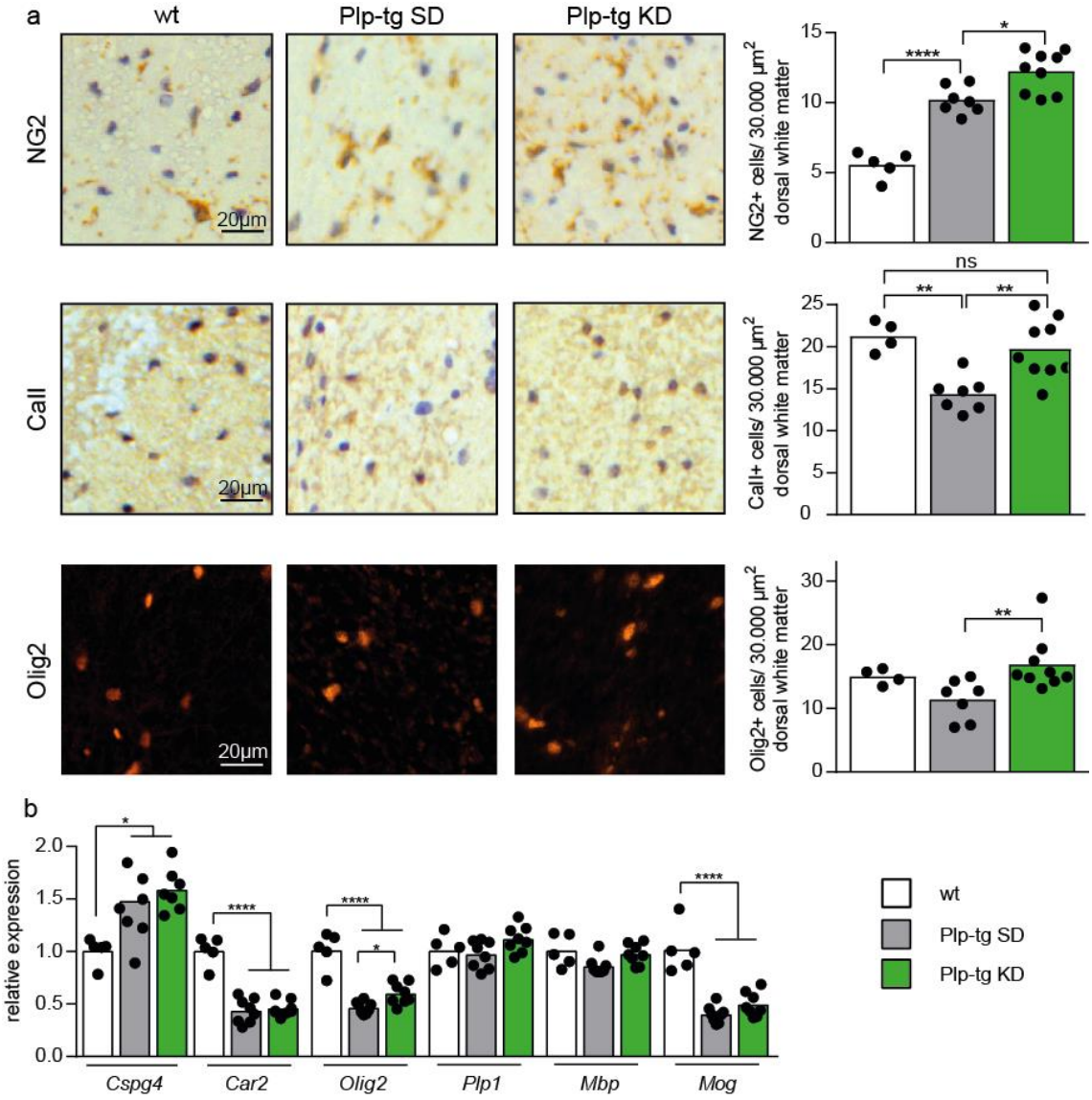

Figure 4.10l KD increased oligodendrocyte numbers in Plp-tg mice. (a) Stainings of NG2 (oligodendrocyte progenitor cells), CAII (mature oligodendrocytes) and Olig2 (oligodedrocyte lineage) in the CST of wildtype, Plp-tg mice on SD and KD. Histological evaluation showing the number of OPCs (NG2; n=5-9), mature oligodendrocytes (CAII; n=4-9) and the whole oligodendrocyte lineage (Olig2; n=4-9). Three sections per animal were staining for quantification. One-way-ANOVA with Tukey's multiple comparison test showed a significant difference between groups. **(b)** Quantitative RT-PCR on dissected lumbar spinal cord tissue determining the expression of *Cspg4*, *Car2*, *Olig2* and, *Plp1*, *Mbp* and *Mog* normalized by *Rplp0* (ribosomal protein P0). One-way-ANOVA with Tukey's multiple comparison test was performed and differences were considered significant with a P-value of *, P<0.05; **, P<0.01; ****, P<0.0001; ns = not-significant, scale bar, 20µm.

In contrast, Plp-tg animals fed KD revealed rescued numbers of mature oligodendrocytes in the CST (WT: 21.3±0.91 $CAII^+$ cells; Plp-tg mice: 14.4±0.78 SD compared to 19.7±1.12 KD).

The same tendency was monitored for Olig2 staining (WT: 15.0±0.63 $Olig2^+$ cells; Plp-tg mice: 11.4±1.19 SD compared to 16.9±1.44 KD). Therefore, these data imply that feeding KD to Plp-tg mice supports OPC differentiation and oligodendrocyte stability. Quantification of the relative expression level of oligodendroglial (*Olig2, Car2* for CAII and *Cspg4* for NG2) and myelin related proteins (*Plp1, Mbp, Mog*) showed a significant increase in *Olig2* expression in KD fed Plp-tg mice (Figure 4.10b). This finding might reflect increase oligodendrocyte stability. The results of increased CAII staining and unaltered *Car2* expression in Plp-tg mice fed KD might be explained by the analysis of different tissues, CST versus whole lumbar spinal cord lysates, respectively.

4.2.7 Increased numbers of myelinated axons in the CST of KD fed Plp-tg mice

Elevated numbers of OPCs and mature oligodendrocytes point to the hypothesis that also myelination might be increased in KD fed Plp-tg mice. Therefore, electron micrographs were evaluated for the number of myelinated axons and the g-ratio in the CST of Plp-tg animals. Ten pictures of single animals were analyzed in regard to the classification of myelinated or unmyelinated axons and the quantification of the g-ratio. Quantification revealed unaltered distribution of axon caliber in the CST of Plp-tg mice (Figure 4.11a).

The g-ratio analysis, reflecting the ratio of fiber diameter divided by axon diameter, was unaltered in the cloud diagram between Plp-tg mice on SD and KD (Figure 4.11b). The significant decrease in myelin thickness of Plp-tg mice compared to wildtype animals was not rescued by feeding KD shown by the measurement of the mean g-ratio. However, plotting the measured g-ratio as a relative frequency distribution with the g-ratio of 0.8 as a border, since it was shown to provide sufficient insulation capacity for proper conduction velocity (Waxman, 1980), myelinated axons below 0.8 showed increased abundance (g-ratio <0.8 in Plp-tg mice: 25.0±5.16% SD compared to 38.1±2.93 KD). Furthermore, a strong decrease in unmyelinated axons (g-ratio of 1) was quantified for KD fed Plp-tg mice (unmyelinated axons in CST of

WT: 4.6±0.51% and Plp-tg mice: 33.4±0.92 SD compared to 23.4±3.08 KD) (Figure 4.11c).

In summary, Plp-tg mice fed KD showed elevated levels of oligodendrocytes as well as increased numbers of myelinated axons both within the CST.

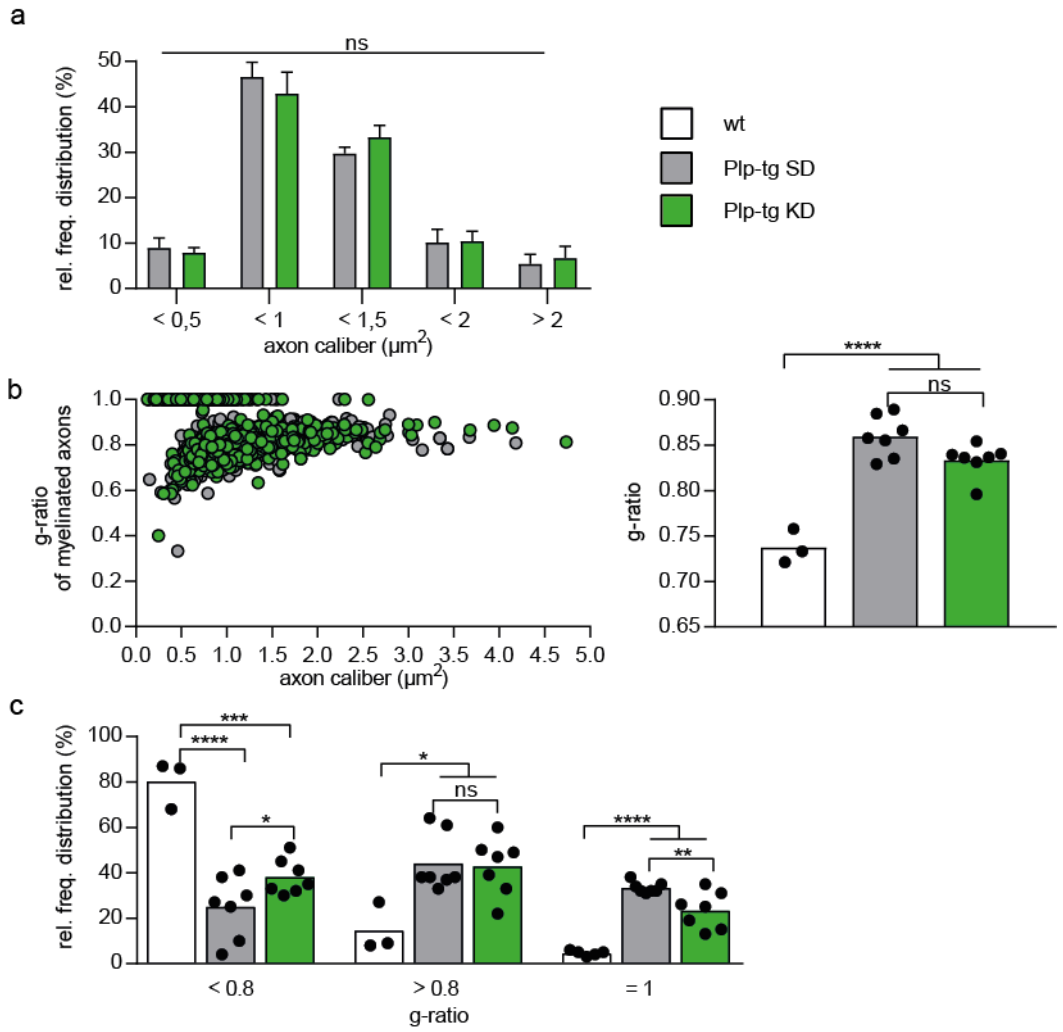

Figure 4.11l Feeding KD increases the number of myelinated axons in Plp-tg animals. (a) Relative frequency distribution of axon calibers in Plp-tg mice on SD and KD (n=7). Student's t-test revealed unaltered distribution. **(b)** G-ratio analysis of only myelinated axons of the CST from wildtype mice, and Plp-tg mice on SD and KD (n=7). One-way-ANOVA with Tukey's multiple comparison test. **(c)** Relative frequency distribution of the g-ratio results from wildtype mice, Plp-tg mice on SD and KD divided in<0.8, >0.8 and 1 for unmyelinated axons. Significance was tested with one-way-ANOVA with Tukey's multiple comparison test. Differences were considered significant with a P-value of *, P<0.05; **, P<0.01; ***, P<0.001; ****, P<0.0001; ns = not-significant.

4.2.8 Feeding a ketogenic diet improved motor performance in Plp-tg mice

Since the Plp-tg mice fed KD for ten weeks showed a reduced gain in body weight, the physical condition was analyzed every other week from six until twelve weeks of age by rotarod performances. Furthermore, to address the question, whether the amelioration of the hypomyelination benefits the affected motor pathology of Plp-tg mice, elevated beam tests were performed as described before (Saher et al., 2012). The rotarod can be used as a measure for motor coordination and alterations might reflect impaired physical condition. The used rotarod set-up consisted of a circular rod turning with increasing speed over time (max. 26 rpm in 150 sec). Quantifications were performed by measuring the accomplished max. speed per animal. Plp-tg mice fed SD showed decreased motor performance with increasing age (Figure 4.12a). In contrast, Plp-tg mice treated with KD showed comparable motor performance on the rotarod to wildtype animals (rotarod speed at 12 weeks WT: 23.9±1.09rpm and Plp-tg mice: 15.5±1.30 SD compared to 21.7±0.99 KD). Therefore, the decreased body weight did not reflect impaired physiological conditions.

The elevated beam test revealed increased numbers of slips for the Plp-tg mice on SD compared to wildtype mice (Figure 4.12b). Interestingly, the number of slips was reduced to wildtype levels in KD fed Plp-tg mice (beam test at 12 weeks WT: 0.15±0.07 slips and Plp-tg mice: 1.29±0.23 SD compared to 0.15±0.8 KD).

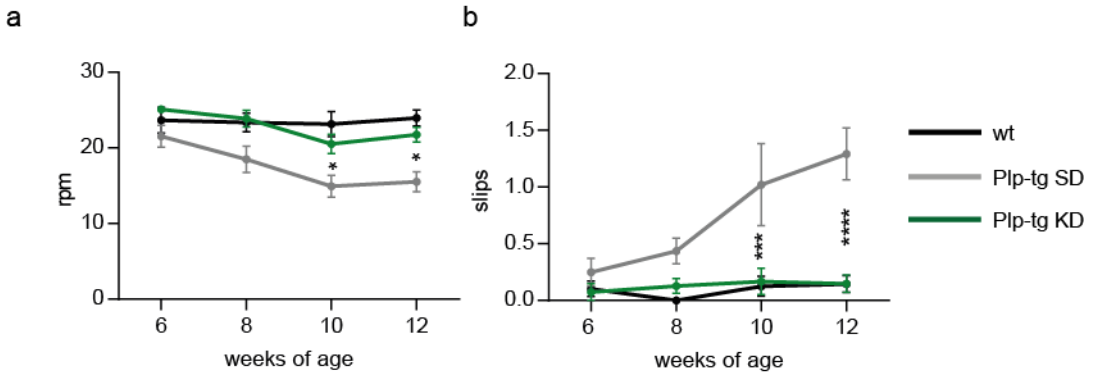

Figure 4.12l Feeding KD to Plp-tg mice improved motor performance. (a) Rotarod performance of wildtype and Plp-tg mice fed SD or KD chow evaluated at 6, 8, 10 and 12 weeks of age. Significance was tested using two-way ANOVA with Sidak's post test. **(b)** Elevated beam test performance of wildtype animals and Plp-tg mice fed SD or KD evaluated at 6, 8, 10 and 12 weeks of age. Two-way ANOVA with Sidak's post test revealed significantly improved motor performance in Plp-tg mice fed KD compared to SD animals. Differences were considered significant with a P-value of *, P<0.05; ***, P<0.001; ****, P<0.0001.

Both behavioral analyses showed amelioration of the affected motor phenotype of Plp-tg mice when feeding KD.

4.2.9 Increased ketone body uptake and consumption in Plp-tg mice treated with KD

Since KD provided an overall benefit for Plp-tg mice by reduced inflammation, increased oligodendrocyte numbers, enhanced myelination and ameliorated motor performance, we wanted to investigate KD induced metabolic changes, which could favor the ameliorated pathology. Fatty acids that have been converted to ketone bodies in the liver are able to cross the BBB mediated by monocarboxylate transporters (MCT) and serve as alternate source for energy and anabolic metabolism. To elucidate whether the Plp-tg mice treated with KD show altered ketone body metabolism within the CNS (lumbar spinal cord tissue was used for comparison with previously tested parameters), the expression level of important enzymes involved in ketone body uptake and ketolysis, were analyzed. Quantification of qRT-PCR results revealed unaltered expression of both monocarboxylate transporters, MCT1 and MCT2 in Plp-tg mice fed SD and an elevation for Plp-tg mice fed KD. MCT1, which is expressed in glia cells and mainly endothelial cells, showed a twofold increase in expression, and MCT2, mainly expressed on neurons increased the expression level by about 50% (Figure 4.13a). These results suggest increased uptake of ketone bodies in glial cells and neurons of the CNS. The main enzymes involved in ketolysis are BDH1 (β-hydroxybutyrate dehydrogenase 1), OXCT1 (3-oxoacid CoA-transferase 1) and ACAT1 (acetyl-coA acetyltransferase 1) (see Introduction Figure 4.4). In Plp-tg mice fed KD, the expression level of *Bdh1* as well as *Acat1* were significantly increased compared to control littermates (*Bdh1* Plp-tg mice: 0.62±0.02 rel. exp. SD compared to 0.83±0.05 KD; *Acat1* Plp-tg mice: 0.6±0.02 rel. exp. SD compared to 0.8±0.05 KD) (Figure 4.13b). *Oxct1*, which expresses the rate limiting enzyme for ketolysis, shows increased protein abundance in the process of ketone body consumption, rather than increased expression levels (Schnyder et al., 2017). Accordingly, *Oxct1* expression level in qRT-PCR analysis was unaltered compared to control littermates (Figure 4.13b). Quantification of OXCT1 protein abundance on western blot revealed a significant increase in KD fed Plp-tg mice compared to SD suggesting enhanced ketone body consumption (Figure 4.13c).

Together, these data suggest not only elevated uptake of ketone bodies in the spinal cord, but also increased ketone body metabolism to build up acetyl-CoA. The metabolite acetyl-CoA can be used in various pathways e.g. to produce energy in form of ATP via the TCA cycle and oxidative phosphorylation or it can be used to build up fatty acids or cholesterol to increase myelination.

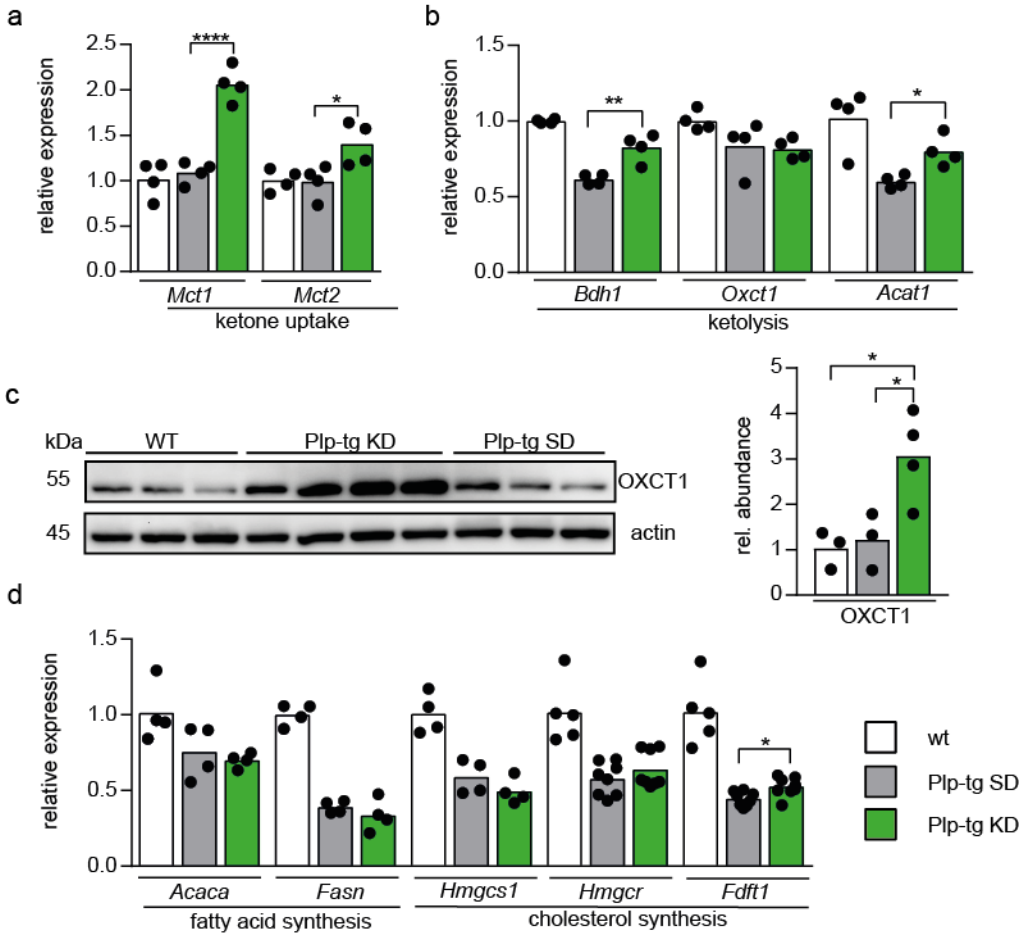

Figure 4.13l Increased ketone body uptake and ketolysis in KD fed animals. (a) Quantitative RT-PCR on dissected lumbar spinal cord tissue determining the expression of markers for ketone body uptake *Mct1* and *Mct2*. **(b)** Markers for ketolysis *Bdh1*, *Oxct1* and *Acat1* **(c)** Western Blot quantification of OXCT1 for wildtype mice (n=3), Plp-tg mice on SD (n=3) compared to KD (n=4). Equal protein load was confirmed with a comparable staining of actin. **(d)** Markers for fatty acid synthesis (*Acc1*, *Fasn*) and cholesterol synthesis (*Hmgcs1*, *Hmgcr*). Significance was tested using one-way-ANOVA with Tukey's multiple comparison test. Results were normalized to untreated wildtype mice and significant was depicted only between Plp-tg groups. Differences were considered significant with a P-value of *, P<0.05; **, P<0.001; ****, P<0.0001.

Due to the fact that increased oligodendrocyte numbers as well as elevated levels of myelinated axons in the CST were quantified, increased fatty acid and cholesterol synthesis were expected. The expression level of *Acaca* (acetyl-coA carboxylase 1, gene), the rate limiting enzyme in fatty acid synthesis and *Fasn (Fatty acid synthase)*

were analyzed. Additionally *cholesterol synthesis with Hmgcs1 (*3-hydroxy-3-methylglutaryl-coA synthase 1), *Hmgcr (*3-hydroxy-3-methylglutaryl-CoA reductase), the rate-limiting step in cholesterol biosynthesis and *Fdftf1* (farnesyl-diphosphate farnesyltransferase 1), also known as squalene synthase, which catalyzes the first dedicated step to cholesterol biosynthesis (Figure 4.13e) were quantified.

Only a significant increase in *Fdft1* expression was detected (*Fdft1* Plp-tg mice: 0.45±0.02 rel. exp. SD compared to 0.53±0.02. KD), which might indicate ongoing myelination. Together, evaluation of fatty acid and cholesterol synthesis revealed almost unaltered synthesis rates indicating that ketone bodies might be predominantly used to provide acetyl-CoA for the energy metabolism, but these needs to be further elucidated.

4.2.10 Decreased accumulation of PLP in endo/lysosomal compartments

Results from cultured *Plp1*-transgenic oligodendrocytes revealed that PLP overexpression causes the accumulation of PLP and cholesterol in the late endosome/ lysosome (Simons et al., 2002). Feeding of a cholesterol-rich diet was shown to prevent the oligodendrocyte from PLP accumulation (Saher et al., 2012). To address the question whether feeding a KD might decrease lysosomal PLP accumulation, co-staining of PLP1 and Lamp1, detecting the endosome/lysosome compartment, was performed.

The co-staining revealed that in Plp-tg animals, PLP accumulates in the endosome/lysosome compartments of the CST. Notably, feeding KD to Plp-tg animals decreases PLP/Lamp1 positive co-staining (preliminary data, not quantified) (Figure 4.14a). PLP might accumulate within oligodendrocytes or in microglia during inflammation.

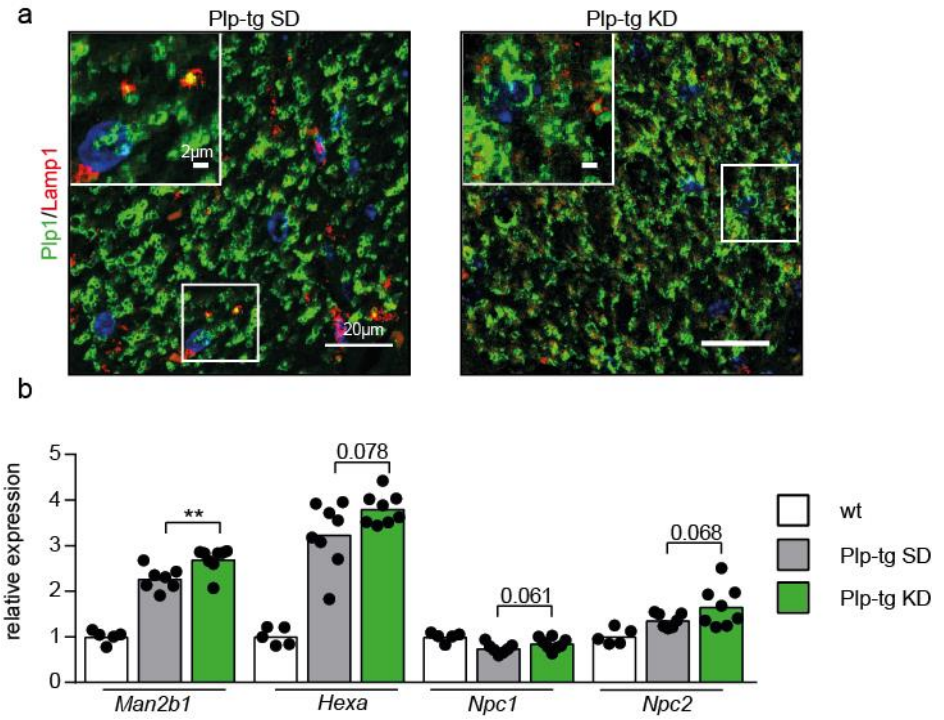

Figure 4.14l Ketogenic diet reduces lysosomal PLP1 accumulation. (a) *Plp1* (green) and *Lamp1* (red) staining, for accumulated *Plp1* in the late endosome/lysosome (*Lamp1*) in the corticospinal tract of wildtype, Plp-tg mice on SD and KD. Scale bar 20µm, selection 2µm. **(b)** Quantitative RT-PCR on dissected lumbar spinal cord tissue determining the expression of markers for lysosomal degradation and transport *Man2b1*, *Hexa Npc1* and *Npc2*. Normalization was performed with *Rplp0*. Results were normalized to untreated wildtype mice and significant was depicted only between Plp-tg groups. One-way-ANOVA with Tukey's multiple comparison test was performed. Differences were considered significant with a P-value of **, P<0.01. Numbers in the bar diagram reveal the P-values, if significance was not given.

One of the main functions of lysosomes is the degradation of intracellular material mediated by acid hydrolases, such as alpha-mannosidase (*Man2b1*) for the breakdown of mannose bound to imported glycoproteins and hexosaminidase (*Hexa*) for the breakdown of GM2 ganglioside. The expression of alpha-mannosidase and hexosaminidase showed a high increase in Plp-tg mice compared to wildtype animals. Moreover, expression was further elevated in KD fed animals compared to control littermates (*Man2b1* Plp-tg mice 2.28±0.09 rel. exp. SD compared to 2.7±0.10 KD; *Hexa* Plp-tg mice: 3.25±0.25 rel. exp. SD compared to 3.81±0.12 KD) (Figure 4.14b).

Membrane remodeling and short-term storage of endocytosed cholesterol is performed by two lysosomal proteins, Niemann-Pick disease type C1 (*NPC1*) and type C2 (*NPC2*). *NPC1* encodes for a large membrane protein and *NPC2* for a small soluble protein. Upon axonal signaling (Trajkovic et al., 2006), these two proteins work together for the egress of cholesterol from the endosomal/lysosomal

compartment. Evaluating the expression level of *Npc1* and *Npc2*, a slight increase was detected in mice fed KD compared to control littermates (*Npc1* Plp-tg mice: 0.75±0.04 rel. exp. SD compared to 0.86±0.05 KD; *Npc2* Plp-tg mice: 1.37±0.06 rel. exp. SD compared to 1.67±0.16 KD). The increase in gene expression might reflect a compensatory mechanism to exocytose accumulated cholesterol together with PLP for reintegration into the secretory pathway. Whether axonal signals contribute to the increased expression of NPC proteins needs further investigation.
In summary, the results suggest decreased PLP abundance in the endo/lysosomal compartment, increased expression of degrading enzymes as well as elevated levels of lysosomal cholesterol transport proteins.

4.2.11 Reduced ER stress in Plp-tg mice fed KD

It is well known that PLP missense mutations cause high ER stress responses with the induction of the unfolded protein response (UPR) (Roboti et al., 2009; Southwood et al., 2002). Elevated myelination as well as decreased PLP accumulation in the endosome/lysosome compartment might indicate that also a reduced amount of PLP is retained within the ER leading to minor ER stress response. Therefore, we investigated whether PLP overexpression in the Plp-tg mice causes an ER stress response and whether KD might alter the ER stress response. Furthermore, degradation of overexpressed PLP was shown to be mainly performed through the action of the cytosolic proteasome (Karim et al., 2010). The ER export of unfolded or retained proteins for proteasomal degradation is mediated by a pathway called endoplasmic-reticulum-associated protein degradation (ERAD) (Anelli and Sitia, 2008). Since elevated levels of the ER-stress transcription factors *Atf6* and *Xbp1* were shown to increase the expression of ERAD transcription factors (Kaneko et al., 2007), the expression level of *Atf6* (Activating transcription factor 6), *Xbp1* (Xbox binding protein 1) and additional marker were analyzed.
Interestingly, expression analysis revealed a high increase especially in *Atf6* as well as *Xbp1* expression in Plp-tg mice on SD. This effect was significantly reduced in KD fed animals compared to control littermates (*Atf6* Plp-tg mice 4.08±0.37 rel. exp. SD compared to 2.51±0.15 KD; *Xbp1* Plp-tg mice 4.58±0.18 rel. exp. SD compared to 3.04±0.35 KD) (Figure 4.15a). Additionally, western blot analysis revealed increased protein abundance of ATF6 in Plp-tg mice on SD compared to wildtype mice. Notably,

the increase was rescued to wildtype levels in KD fed animals (ATF6 Plp-tg mice 3.4±0.66 rel. abundance. SD compared to 0.74±0.08 KD) (Figure 4.15b).

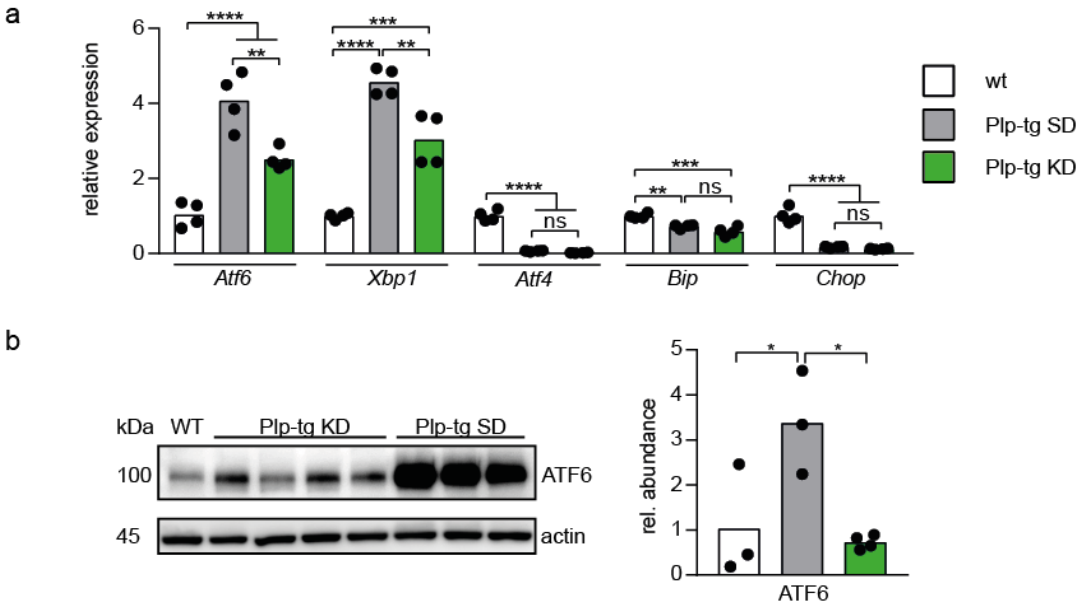

Figure 4.15l KD decreased ER stress response markers in Plp-tg mice. (a) Quantitative RT-PCR on dissected lumbar spinal cord tissue determining the expression of markers for ER stress response, *Atf6*, *Atf4*, *Xbp1*, *Bip* and *Chop* normalized by *Rplp0.* Results were normalized, indicating the relative expression compared to untreated wildtype mice. **(b)** Western blot analysis of full length ATF6 with β-actin used for normalization (one representative wildtype) One-way-ANOVA with Tukey's multiple comparison test was performed and differences were considered significant with a P-value of *, P<0.05; **, P<0.01; P<0.01; ***, P<0.001; ****, P<0.0001.

In summary, these set of experiments revealed an increased ER stress response in untreated *Plp1*-overexpressing mice. This effect was diminished by KD treatment of Plp-tg mice.

4.2.12 Increased mitochondria size in Plp-tg mice can be rescued by KD treatment.

Myelin is essential for proper axonal conduction velocity by providing electrical insulation and the loss of insulation is hypothesized to cause higher energy demands for thinly or unmyelinated axons. Furthermore, unmyelinated axons have a five-fold increased energy demand to preserve wiring capacity in comparison to myelinated axons with the same diameter (Neishabouri and Faisal, 2011). In a severe model of PMD it was shown that Plp-tg mice (Plp-tg$^{66/66}$ with 7 copies of the transgene (Readhead et al., 1994) suffer from an increased mitochondria size in axons of the

spinal cord accompanied by mitochondria dysfunction and decreased ATP levels (Ruiz et al., 2017). To address the question whether our Plp-tg mice (Plp-tg$^{72/72}$) show also increased mitochondria size in spinal cord axons, mitochondria size on electron micrographs of the CST of Plp-tg mice at the age of twelve weeks was analyzed.

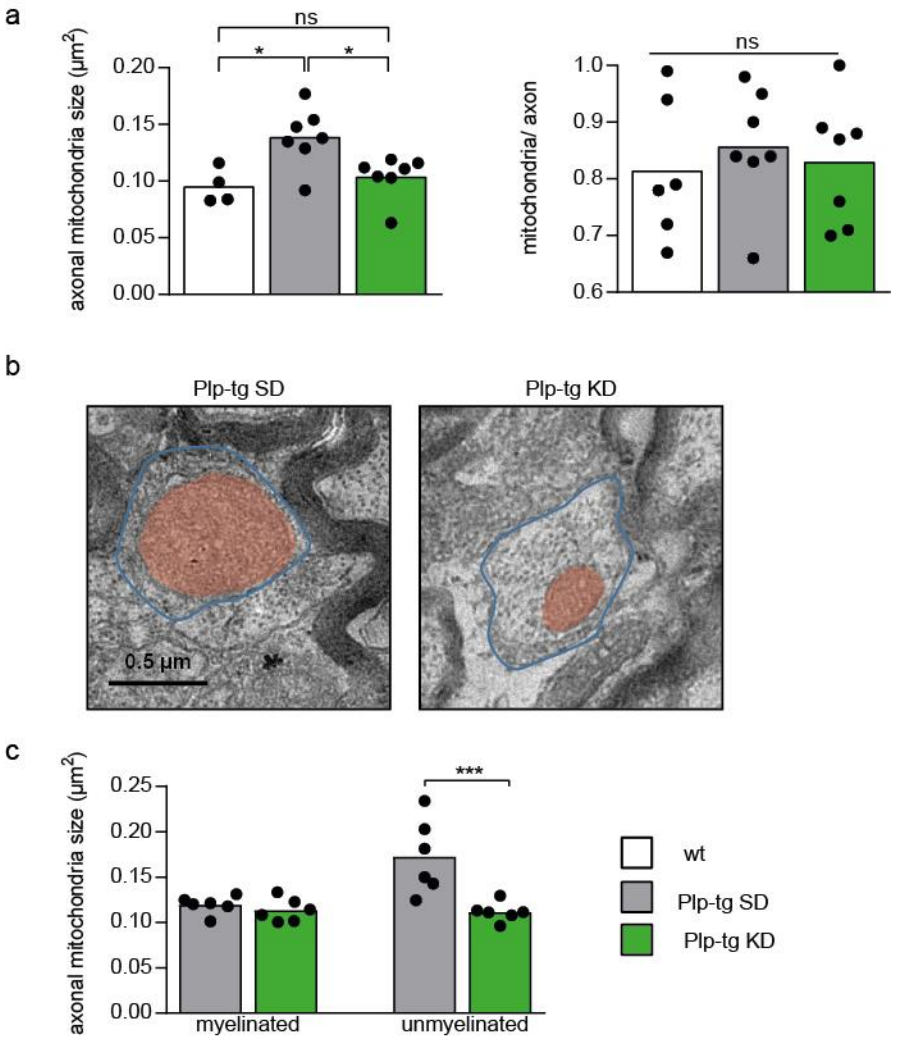

Figure 4.16l Ketogenic diet rescues mitochondria enlargement in Plp-tg mice. (a) Quantification of mitochondria size in the CST of wildtype mice, and Plp-tg animals on SD or KD (n=4-7). 100 mitochondria per animal were counted in approximately 80 axons. Differences between groups were evaluated with the one-way-ANOVA with Tukey's multiple comparison test. **(b)** Mitochondria in the CST of Plp-tg mice on SD and KD. The unmyelinated axon is outlined in blue and the mitochondria colored in red. **(c)** Mitochondria size in µm^2 divided in myelinated and unmyelinated axons for Plp-tg mice treated with SD or KD Scale bar 0.5µm. Differences were considered significant with a P-value of *, P<0.05; ***, P<0.001; ns = not-significant

Interestingly, elevated numbers of mitochondria with increased size were found in Plp-tg mice fed SD compared to wildtype mice (Figure 4.16a/b). Surprisingly, mitochondria size was rescued to almost wildtype level by providing KD to the animals (mitochondria size for WT: 0.096±0.01µm^2 and Plp-tg mice: 0.14±0.01 SD

compared to 0.10±0.01 KD). Notably, the increased mitochondria size in SD fed Plp-tg was limited to unmyelinated axons, suggesting altered mitochondrial function in unmyelinated axons of Plp-tg mice fed SD. In contrast, mitochondria of unmyelinated axons in Plp-tg mice fed KD showed unaltered size (mitochondria size of unmyelinated axons for Plp-tg mice 0.17±0.02µm^2 SD compared to 0.11±0.01 KD) (Figure 4.16c).

These data might suggest axonal mitochondria dysfunction especially in unmyelinated axons of our Plp-tg. Interestingly, feeding the KD to Plp-tg animals might provide a treatment strategy to address impaired mitochondrial function.

4.2.13 Ameliorated axonal pathology in Plp-tg mice fed KD

Data of the demyelination state and mitochondria size point to the assumption that especially unmyelinated axons of Plp-tg animals suffer from impaired mitochondrial metabolism, which could affect axonal health. As readout for axonal pathology, APP (amyloid precursor protein) staining was performed and axonal spheroids in the CST of Plp-tg mice were counted. The quantification exhibit highly increased numbers of APP positive spheroids within the CST of Plp-tg mice on SD compared to wildtype controls. These results suggest axonal impairments of untreated Plp-tg animals. Interestingly, Plp-tg mice fed KD showed a dramatic reduction of APP positive spheroids compared to control littermates on SD indicating increased axonal health in KD fed animals (WT: 3.6±1.01 APP$^+$ spheroids; Plp-tg mice: 62.4±7.37 SD compared to 25.6±1.9 KD) (Figure 4.17).

Taken together, these data showed enhanced axonal pathology in untreated Plp-tg mice, which was diminished by KD treatment.

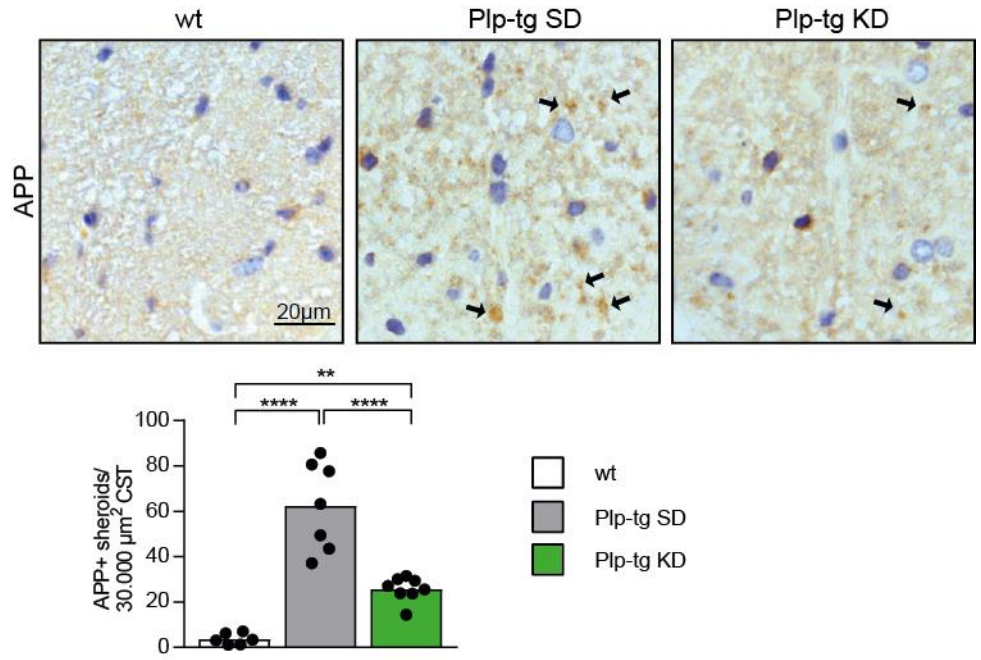

Figure 4.17l Decreased number of APP positive axonal spheroids in KD fed animals. APP staining in the CST of non-transgenic wildtype, Plp-tg mice on SD and KD. Quantification of the number of APP positive axonal spheroids (n=6-8). Three sections per animal were staining for quantification. One-way-ANOVA with Tukey's multiple comparison test were performed with differences considered significant with a P-value of **, P<0.01; ****, P<0.0001; scale bar, 20µm.

4.3 Discussion

4.3.1 Phenotypical changes of Plp-tg mice

The first challenge of the experimental work was the unexpected phenotypical change of Plp-tg mice. Overall, the current Plp-tg mice showed reduced disease expression compared to the same mouse colony in 2012, including ameliorated hypomyelination pathology accompanied by less severe inflammation and improved motor performance. We investigated whether loss of transgene copy might explain the phenotypic alterations, but overexpression of *Plp1* mRNA in brain lysates was still detectable to the same extend as shown previously (Prukop et al., 2014). Another possibility might be that Plp-tg mice experienced an unspecific genetic drift and that the infection of mites and helminths provoked a highly selective environment, spreading the genetic alteration throughout the mouse colony. Many inbred laboratory mouse strains are prone to genetic alterations due to heterozygote selection, mutations or contamination by uncontrolled breeding between different strains (Casellas, 2011). In fact, Plp-tg mice suffer from toxic accumulation of PLP protein, one possibility to explain the weaker phenotype might be by diverse alteration of the PLP degradation machinery (e.g. increased expression of ERAD components). Increased PLP degradation would lead to stress release in oligodendrocytes which might cause enhanced oligodendrocyte survival with secondarily reduced inflammation and reduced hypomyelination. Another example might be that an unspecific genetic drift affected the translation of Plp mRNA into PLP protein, which might lead to decreased levels of PLP protein and therefore release of cell stress. However, the detection of genetic alterations is only possible by the performance of a full genome scan of the mouse line, at best in comparison with phenotypically unaffected control mice of previous cohorts. Even after localization of the genetic alteration, the reestablishment of the former genotype remains challenging. Since this study focused on a novel therapeutic approach by feeding a lipid-based KD, we decided to perform our new experimental design with the current Plp-tg mouse line, because PMD disease parameters were still present, albeit weaker.

4.3.2 Mitochondrial dysfunction contributes to axonal loss

Our study provides insight in structural alterations of axonal mitochondria in the CST of untreated Plp-tg mice, which is in accordance with another study of Plp overexpressing mice (Plp-tg$^{66/66}$; (Ruiz et al., 2017). Plp-tg$^{72/72}$ mice at the age of twelve weeks exhibit highly increased mitochondrial size in unmyelinated axons of the CST. Our results are supported by the finding that Plp-tg$^{72/72}$ showed increased mitochondrial density in the optic nerve especially at advanced demyelination state with four month (Hogan et al., 2009). Furthermore, Plp-tg overexpressing mice (Plp-tg$^{66/66}$) showed decreased ATP levels to about 50% in whole brain tissue (Hüttemann et al., 2009). In addition calculation using a stochastic, biophysical model revealed a five-fold increased energy demand to preserve wiring capacity of unmyelinated axons in comparison to myelinated axons with the same diameter (Neishabouri and Faisal, 2011). Therefore, the increased axonal mitochondria size and elevated mitochondria density might be a compensatory mechanism of axons to adapt to the higher energy needs upon severe demyelination.

Further, overexpressed PLP seems to be highly associated to the inner mitochondrial membrane accompanied with reduced mitochondrial membrane potential and increased mitochondrial biogenesis in brains of five weeks old mice (Hüttemann et al., 2009). In accordance, cysteine motifs of PLP protein were demonstrated to be recognized by the Mia40/Erv1 pathway for mitochondrial import (Appikatla et al., 2014). Mitochondrial PLP association was accompanied by decreased pH levels in media. Furthermore, DRG neurons co-cultured with Plp-overexpressing HEK cells showed an acidification of cultivation media leading to reduced neuronal viability (Boucher et al., 2002). These results suggest an effect of elevated PLP levels on neuronal health in addition to a direct effect of PLP overexpression on mitochondrial function. Therefore, PLP accumulation in oligodendroglial mitochondria might cause mitochondrial dysfunction with the disruption of axonal energy supply ultimately leading to neuronal death (Hüttemann et al., 2009).

These results might suggest a mechanism by which increased axonal energy demands, due to accumulated PLP and demyelination, could lead to an increase in mitochondria density or the elevation of mitochondrial function accompanied by an increase in size. Upon disease progression with highly severe demyelination of axons, the theoretical mitochondrial adaptation to axonal energy requirement might be insufficient to sustain neuronal function highlighted by changes in axonal pH might

resulting in axonal death. However, direct evidence for an *in vivo* mechanism is lacking. Nevertheless, these observations in combination with our data support a possible therapeutic target by providing a metabolic alternative to axons to cover for increased energy demands.

4.3.3 KD therapy ameliorated disease severity in Plp-tg mice

The present study further proposes a novel therapeutic approach for the leukodystrophy Pelizaeus-Merzbacher disease (PMD) by feeding a lipid-based KD. Previously, KD treatment was shown to provide anti-inflammatory properties, increase oxidative phosphorylation and reduce oxidative stress in mitochondria (Abou-Sleiman et al., 2006; Bough and Rho, 2007; Yang and Cheng, 2010). Moreover, KD treatment might induce a metabolic switch that could enhance myelination due to fact that ketone bodies are predominantly used for the synthesis of fatty acids and especially cholesterol (Webber and Edmond, 1977). Therefore, KD provided the perfect requirements for the treatment of neurodegenerative diseases associated with hypomyelination and mitochondrial malfunctions such as PMD. Hence, Plp-tg mice were used to investigate whether increased cerebral ketone body metabolism might provide advantages to ameliorate PMD disease severity.

The mammalian brain requires high amounts of energy to sustain essential functions, like neuronal activity and recycling of neurotransmitters (Bélanger et al., 2011). Despite the use of glucose as primary energy source, brain cells metabolize other substrates such as fatty acids or ketone bodies during glucose deprivation or increased energy demands (Ebert et al., 2003; Morris, 2005). According to our hypothesis, ketone bodies as alternative metabolites might be able to increase local cholesterol synthesis (e.g in astrocytes) to support oligodendrocytes from Plp accumulation, by restoring the ratio of cholesterol and Plp as it was shown before (Saher et al., 2012). Furthermore, we speculate that KD might enhance local energy production (e.g in astrocytes or neurons) by a glycolysis independent pathway to support increased neuronal energy demands upon severe demyelination.

4.3.3.1 Reduced hypomyelination by KD treatment

The application of KD diet to Plp-tg mice ameliorated disease severity with decreased hypomyelination. The increase in myelination might be due to enhanced OPC proliferation and increased stability of mature oligodendrocytes. *In vivo* tracing of labeled β-hydroxybutyrate and acetoacetate revealed that ketone bodies are predominantly used for the synthesis of fatty acids and especially cholesterol (Webber and Edmond, 1977). Moreover, it was shown that dietary cholesterol application in our mouse line restored oligodendrocyte numbers and increased myelination (Saher et al., 2012). Furthermore, cholesterol supplementation in the cuprizone model, a model for de- and remyelination, revealed increased OPC proliferation and oligodendrocyte differentiation (Berghoff et al., 2017b). Our data showed an increase in mRNA abundance of squalene synthase (*Fdftf1*), which catalyzes the first dedicated step to cholesterol biosynthesis. This increase possibly reflects elevated myelination, but it might also suggest that feeding a KD increases the synthesis of cholesterol, thereby supporting myelination. Considering that ketone bodies in young rodents are used to synthesize lipids and especially cholesterol for the integration in the myelin sheath (Koper et al., 1981) might support the assumption that KD enhances cholesterol synthesis, thereby increasing myelination. Furthermore, ketone bodies might facilitate lipid synthesis, since aceto-acetyl-CoA, which is produced during ketolysis can be directly integrated in fatty acid synthesis. In contrast glycolytic derived acetyl-CoA must first be converted to aceto-acetyl-CoA (Morris, 2005). Moreover, KD itself contains small amounts of cholesterol (0.09%), which could directly enter the CNS, since our Plp-tg mice suffer from impaired BBB function (Saher et al., 2012; this study).

A highly speculative explanation might be that during PMD disease state, astrocytes, which are highly activated in our Plp-tg mice, might support axons with lactate to cover increased axonal energy requirements due to severe hypomyelination. Furthermore, PLP-laden oligodendrocytes might try to support axons as well. When PLP accumulation in oligodendrocytes would reach a certain threshold, myelination is impaired finally causing oligodendrocyte cell death. We showed that KD treatment of Plp-tg mice significantly increased mRNA expression of *Mct1* and *Mct2*. Since endothelial cells and astrocytes express *Mct1* (Zhang et al., 2014), these results might suggest enhanced ketone body import. Increased levels of intracellular ketone bodies could lead to increased cholesterol synthesis to enhance astrocytic

cholesterol support for oligodendrocytes. This would restore the ratio of cholesterol and PLP in accordance with our previous study (Saher et al., 2012), leading to increased myelination. This hypothesis might be supported by our finding that Plp-tg mice treated with KD revealed enhanced stability of mature oligodendrocytes.
In contrast, HMG-CoA reductase, the rate limiting enzyme of cholesterol synthesis, showed unaltered mRNA expression in Plp-tg mice fed KD compared SD. Since evidence of a direct function of ketone bodies on astrocytic cholesterol synthesis are lacking, further experiments need to be performed to support this hypothesis. The next step could be to analyze cholesterol synthesis *in vitro* in a mutant mixed glia culture with and w/o the treatment of ketone bodies. Another possibility might be to extract glia cells from spinal cord tissue e.g by magnetic cell isolation to analyze the cell specific cholesterol synthesis related expression profile. Until then, we need to consider that KD treatment might ameliorate PMD disease pathology by another mechanism (see chapter 4.3.3.3).

4.3.3.2 KD treatment reduced ER stress

Overexpressed PLP has been shown to accumulate in the ER as well as in the endosome/lysosome compartment (Saher et al., 2012; Simons et al., 2002; Southwood et al., 2007). Increased ER stress in the PMD mouse model is highly associated with Plp missense mutation and rather modest changes were reported for mice with extra copies of the native *Plp1* gene (Cerghet et al., 2002; Southwood et al., 2007). This study provides evidence of an enhanced ER stress response in the mild Plp-tg$^{72/72}$ overexpressing mice with an increase in *Xbp1* and *Atf6* transcription and ATF6 abundance. The transcription factors *Atf6* and *Xbp1* were shown to increase the expression of ERAD transcription factors (*Hrd1* and *Sel1*) (Kaneko et al., 2007) and the induced cytosolic proteasome degradation machinery was proven to be the main pathway for degradation of overexpressed Plp (Karim et al., 2010). Our data revealed that by feeding a KD, Plp accumulation is decreased in the endosome/lysosome compartment. Furthermore, Plp overexpression associated ER stress is highly attenuated shown by decreased mRNA expression of *Atf6* and *Xbp1* reduced ATF6 protein level. The current study suggests that the amelioration of intracellular PLP accumulation might be a secondary effect due to the increased PLP incorporation into the newly formed myelin sheaths. Ketone bodies might be

imported and metabolized by neighboring cells (e.g. astrocytes) to synthesize cholesterol for the support of highly impaired oligodendrocytes. This might restore the ratio of PLP and cholesterol and enhance myelination as it was shown before (Saher et al., 2012). Conclusively, reduction in ER stress response factors ATF6 and XBP1 might reflect the decreased PLP retention within the ER. This might be supported by the indicated amelioration of PLP accumulation in the endosome/lysosome.

4.3.3.3 KD might provide metabolic support for neurons

As mentioned above, mitochondrial dysfunction contributed to the severe axonal loss in Plp-tg mice. The current study demonstrates a treatment approach in which we supplied Plp-tg mice with alternative metabolites in form of ketone bodies. This study provides evidence that unmyelinated axons in the CST of Plp-tg mice suffer from mitochondrial alterations, which can be rescued by the treatment with KD. Moreover, overall axonal pathology (myelinated and unmyelinated axons) was reduced indicated by highly decreased axonal spheroids in the CST of Plp-tg mice after KD treatment. These data might also suggest that the KD especially supports unmyelinated axons with additional energy sources to compensate for local energy demands, which favors axonal health. Together these results raised the question whether neurons themselves are able to take up ketone bodies for local energy production or if other cell types provide energetic support via metabolic coupling.
The major glucose transporter GLUT1 and the main ketone body transporter MCT1 are highly expressed in astrocytes (Zhang et al., 2014). Astrocytic end-feet are involved in the maintenance of the BBB (Abbott et al., 2006). Therefore, they have direct access to glucose and ketone bodies transported via the blood stream. Interestingly, astrogliosis in the CST of Plp-tg mice was persistently increased comparing applications of SD and KD. This finding might possibly suggest astrocytic functioning in the support of axons in our leukodystrophy model.

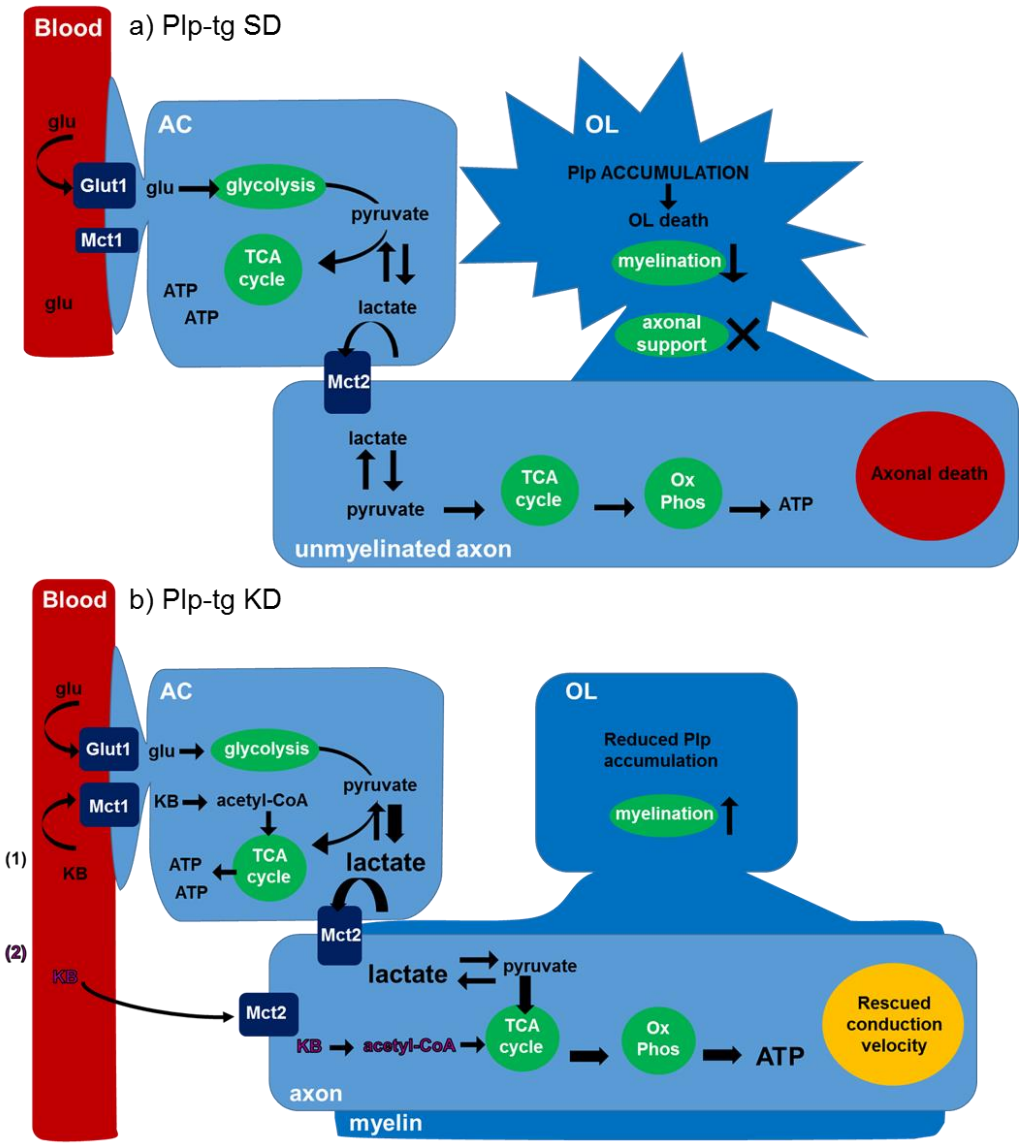

Figure 4.18l Working model of KD treatment to support axonal energy requirements. (a) In untreated Plp-tg mice on standard diet (SD), Plp accumulation in oligodendrocytes (OL) leads to OL cells death. Due to decreased numbers of OL, myelination and the axonal support by OL might be highly impaired. Consequently, upon disease progression most axons become severely demyelinated. Peripheral glucose (glu) can be imported by astrocytes (AC) via the Glut1 transporter to perform glycolysis. Lactate is generated, which can be provided via metabolic coupling to unmyelinated axons. Axons can import lactate via Mct2 transporters to enhance local energy production. If axons suffer from energy deficiency, axonal conduction velocity is disrupted leading finally to axonal death. **(b)** Feeding a ketogenic diet (KD) might support axonal energy requirements in two distinct manners (1) ketone bodies (KB) can be transported via Mct1 into astrocytes. Astrocytes might metabolize KB for local energy demands and might use glycolysis derived lactate to provide it to axons. This mechanism would enhance axonal lactate supply by astrocytes. (2) KB might be directly imported into axons via Mct2 to be metabolized and used for local ATP production.

In our model, we hypothesize that in untreated Plp-tg mice, astrocytes might provide energy depleted axons with lactate to preserve conduction (astrocyte-neuron lactate shuttle; Pellerin and Magistretti, 1994) (Figure 4.18a). Furthermore, also oligodendrocytes might provide metabolic coupling to neurons (Fünfschilling et al.,

2012). In this study we show that upon disease progression in Plp-tg mice, oligodendrocytes suffer from accumulated PLP, which leads to increased oligodendrocyte cell death. Neurons might lose the speculated energetic support of oligodendrocytes. Further, postulated astrocytic support of neurons might become highly important (Pellerin and Magistretti, 1994). Demyelination in the CST of Plp-tg mice would lead to increased axonal energy demands, which might not be covered by astrocytic lactate support. Additionally to glucose metabolism, ketolysis by astrocytes might be beneficial to sustain the metabolic support of neurons (Figure 4.18b (1)). In summary, we speculate that astrocytic ketolysis might provide neuroprotective properties by preserving neuronal function in a CNS disease state. However, we did not show that astrocytes increase the import of ketone bodies and use them to provide support to axons. Therefore, another possibility might be that neurons import ketone bodies to cover for their local energy demands. Neurons highly express the ketone body transporter Mct2 (Zhang et al., 2014).

In our study we demonstrate that *Mct2* mRNA expression was upregulated upon KD treatment, suggesting increased neuronal ketone body uptake. In rat hippocampal sliced cultures, neuronal acetyl-CoA metabolism is preferentially performed by β-hydroyxbutyrate oxidation compared to glycolytic substrates (Valente-Silva et al., 2015). Hence, we hypothesize that neurons are able to metabolize ketone bodies to cover their local energy demands (Figure 4.18b (2)). In neurons, ketone bodies can be converted to acetyl-CoA through a lactate independent metabolic pathway and directly integrated in the TCA cycle for local energy production.

Taken together, our data demonstrates a novel therapeutic approach for the leukodystrophy PMD by the treatment with KD. This study highlights the benefit of KD on (1) the preservation of a stable oligodendrocyte pool for proper myelination and (2) the possible metabolic support of axonal energy requirements. These advantages favor reduced Plp accumulation, decreased ER stress and improved motor performance in Plp-overexpressing mice. Especially the ability of ketone bodies to enter the CNS might provide the major advantage for PMD patient, since it is still uncertain whether they exhibit BBB impairments.

As a future perspective, KD treatment of PMD patients might improve their livelihood and ameliorate disease pathology as it was shown for our Plp-tg mice. Furthermore, clinical trials with KD have been approved for diverse neurological disease, which facilitates the translation of our treatment approach to PMD patients.

5 BBB manipulation with short-term isoflurane treatment enhances the delivery of cisplatin chemotherapy for glioblastoma treatment in mice

5.1 Introduction

5.1.1 Blood-brain-barrier

5.1.1.1 BBB components

The blood-brain barrier (BBB) regulates the flux of metabolites between the circulatory blood system and central nervous system. Furthermore, BBB protects the CNS from neurotoxic substances and pathogens. The blood system supplies the brain with oxygen and nutrients and eliminates carbon dioxide throughout the body. In return, the CNS releases signaling molecules such as hormones (Blood et al., 2015). The cerebral spinal fluid (CSF) of the CNS has a unique composition, which allows execution of neuronal function. Disruption of CNS homeostasis (e.g. through diverse neurological diseases that affect BBB permeability) results in dysregulation of signaling pathways, uncontrolled immune responses, inflammation and finally failure of neuronal transmission.

Endothelial cells (EC) form a thin layer endothelial tube enabling blood flow. In the CNS ECs are tightly connected to each other via specialized junctions, called tight junctions (Brightman, 1969; Reese and Karnovsky, 1967) (Figure 5.1). Brain ECs have unique physiological properties compared to other epithelial cells of the body to sustain the maintenance of barrier function. For instance, brain ECs revealed to have increased mitochondrial density (Oldendorf et al., 1977), which might reflect increased energy requirements due to the maintenance of transport function or preservations of tight junction structures. Moreover, decreased expression of leukocyte adhesion molecules in ECs is thought to restrict invasion of immune cells (Blood et al., 2015; Daneman et al., 2010a).

In addition to ECs, pericytes and astrocytes play an important role in the development and maintenance of barrier function forming the Neurovascular Unit (NVU). Pericytes are in close contact to endothelial cells on the ablumenal surface, embedded in the basal lamina membrane (Sims, 1986). During development ECs secrete platelet-

derived growth factor β (PDGF-β) for pericyte recruitment and alteration of pericyte numbers can cause BBB dysfunction (Blanchette and Daneman, 2015).

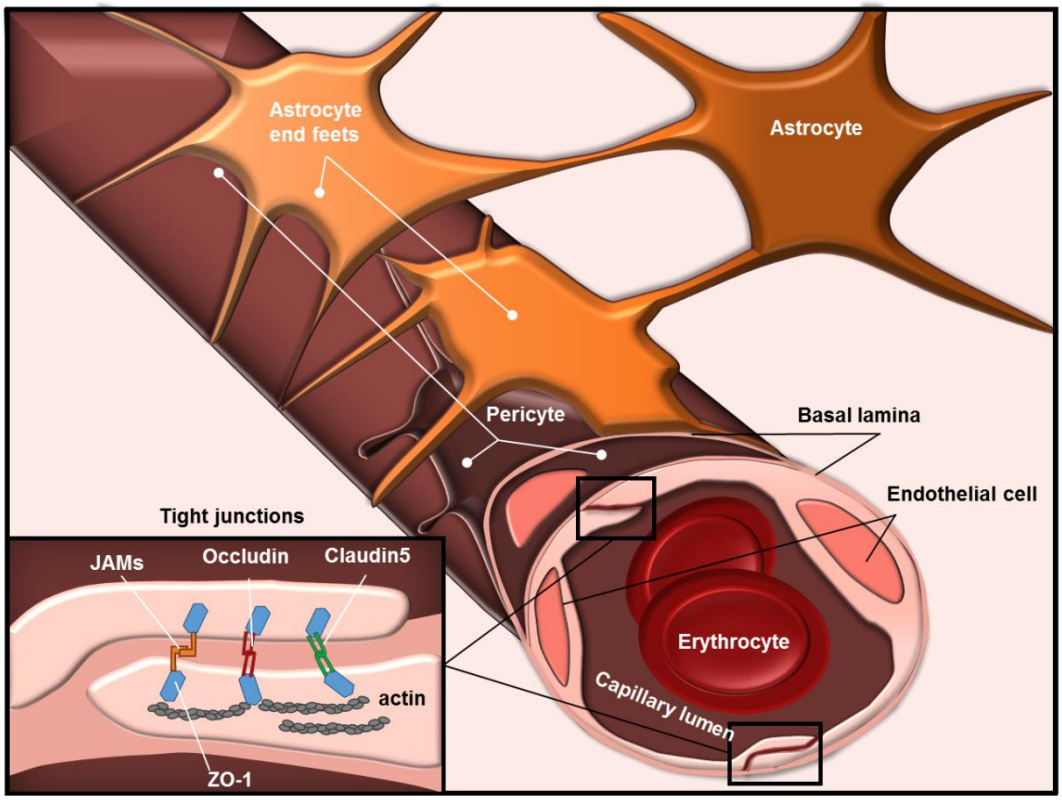

Figure 5.1l Components of the BBB. Endothelial cells form the linings of the blood vessels. Pericytes attached to the endothelial cell layer are embedded in the basal lamina. Astrocytic end-feet ensheath almost the complete endothelial tube. Tight junction proteins, including occludin, claudin-5 and JAMs built the connection between adjacent endothelial cells. Scaffold proteins such as ZO-1 provide the intracellular connection of the tight junctions to the actin cytoskeleton.

In recent years many functions of pericytes were unraveled such as the regulation of the capillary diameter (Peppiatt et al., 2006) or the control of cerebral blood flow (Hall et al., 2014). Furthermore, pericytes function in angiogenesis, wound healing and provide a regulatory role in the infiltration of immune cells (Daneman and Prat, 2015). During embryogenesis pericytes are indispensable for BBB formation, even before astrocytic end-feet attachment (Daneman et al., 2010b). Pericytes are critically involved in BBB maintenance indicated by severely enhanced BBB permeability for small and large molecular weight tracers in pericyte deficient mice (Armulik et al., 2010). Upon pericyte deficiency astrocyte end-feet revealed abnormal polarization, indicated by altered abundance and localization of the water channel protein, aquaporin 4 (AQP4). Furthermore, pericytes were shown to control BBB function by

regulating endothelial gene expression e.g. for the transferrin receptor (CD71), which functions in iron uptake

The covering of endothelial cells and pericytes by the basal lamina membrane is of great importance, since it serves as an additional barrier for substances to enter the CNS. The basal lamina is composed of extracellular matrix proteins such as collagen, laminin, heparin sulfate proteoglycan and fibronectin, which are secreted by endothelial cells, pericytes and astrocytes (Keaney and Campbell, 2015). Furthermore, astrocytic derived laminin was shown to support pericyte differentiation by binding to integrin α2 receptor (Yao et al., 2014). Moreover, astrocytic derived laminin deficiency leads to decreased aquaporin 4 abundance and a reduced level of tight junction proteins, occludin and claudin-5.

Astrocytes belong to the components of the NVU and play an important role in maintaining BBB function (Blanchette and Daneman, 2015). The extended astrocytic end-feet ensheath almost the complete endothelial tube (Abbott et al., 2006). These astrocytic borders, referred to as the *glia limitans*, provide functional barrier properties e.g. by restriction of immune cell infiltration (Sofroniew, 2015). Furthermore, in *in vitro* BBB models, ECs co-cultured with astrocytes provide enhanced transendothelial resistance, highlighting the importance of astrocytic function (Abbott and Friedman, 2012). In addition, astrocytes interact with pericytes and even neurons to adjust cerebral blood flow highlighting the interplay at the NVU (Attwell et al., 2010).

Taken together, each component of the neurovascular unit possesses a distinct function and the complex crosstalk among them provides the basis for the strict regulation of BBB function.

5.1.1.2 Tight and adherens junction proteins at the BBB

The tight connection between adjacent endothelial cells is achieved through the action of tight and adherens junction proteins. Their main function is to prohibit paracellular passage ions (Bazzoni and Dejana, 2004). In general, tight junctions are divided in claudins, occludins, and junctional adhesion molecules.

Claudins are tetraspan proteins at the BBB of the CNS that include four different isoforms, claudin-1,-3,-5 and -12 (Morita et al., 1999). All four isoforms are expressed by endothelial cells of the CNS, with claudin-5 as the main constituent of cerebral

tight junction protein (Jia et al., 2014). Mice lacking claudin-5 develop increased permeability of the BBB, but the passage was limited only to small molecules (Nitta et al., 2003). Claudin-5 function involves the restriction of ion permeability and the C-terminus of claudin-5 provided the connection to cytoskeleton adapter proteins such as ZO proteins (Jia et al., 2014).

Occludin with four transmembrane domains was shown to be important for barrier resistance. Transfection of a MDCK cell line (Madin-Darby canine kidney) with COOH-terminally truncated occludin revealed increased paracellular flux of especially small tracers (Balda et al., 1996). Overall tight junction appearance was reported to be normal. Since new analytic methods to investigate tight junction appearance (e.g. high-resolution microscopy) have been invented in the last decades, this statement needs to be reviewed. Deletion of occludin N-terminus led to a strong failure of tight junction assembly, with low transendothelial electrical resistance and diffusion of tracers (Bamforth et al., 1999). Mice lacking functional full-length occludin exhibit a mild BBB phenotype with high electrical resistance and only minor increases in calcium flux (Saitou et al., 2000). Tracer entries as well as other factors, which might contribute to tight junction formation in the absence of occludin, were not evaluated. Furthermore, occludin deficient mice developed several other defects like growth retardation, inflammation and altered bone structure pointing to other functions of occludin in addition to tight junction formation of the BBB. Occludin was shown to be highly prone to phosphorylation (Sakakibara et al., 1997). Moreover, in MDCK I cells only highly phosphorylated occludin localized to tight junctions, whereas non- or less phosphorylated occludin was found at the basolateral membrane and in cytoplasmic vesicles. All together, these studies provided evidence that occludin contributes to tight junction stability and regulates paracellular BBB permeability.

Junctional adhesion molecules (JAMs) are located between endothelial cells adjacent to occludin and claudins. JAMs contain two immunoglobulin-like domains and one transmembrane domain (Garrido-Urbani et al., 2014). Furthermore, the C-terminal JAM domain protrudes into the cytosol and contains a protein binding domain (PDZ domain) for interaction with scaffold proteins such as ZO-1 (Stamatovic et al., 2012). JAMs were shown to regulate monocyte transmigration of the BBB (Martìn-Padura et al., 1998).

Furthermore, tricellulin a novel tight junction protein with four transmembrane domains was reported to be enriched at tricellular endothelial cell contacts (Ikenouchi

et al., 2005). Knockdown of tricellulin in cultured epithelial cells revealed altered distribution of claudin-3 and occludin pointing to tricellulin function in tight junction stability.

Supporting the stability of endothelial connection in the intercellular cleft, the tight junction proteins are linked to the cytoskeleton by adaptor molecules like ZO-1 (zona occludens), ZO-2 or cingulin (Dejana, 2004). ZO proteins are junctional adaptor proteins that were shown to interact with the actin cytoskeleton as well as adherens and tight junction proteins. Knockdown of ZO-1 and ZO-2 in mouse cultured epithelial cells disrupted tight junction assembly (Umeda et al., 2006).

Adherens junctions are involved in several functions such as regulation of cell-cell adhesion, connections with the cytoskeleton as well as intracellular signaling (Hartsock and Nelson, 2008). Furthermore, adherens junctions are supposed to be important to provide EC contact prior to tight junction assembly. In fact, adherens junction proteins strengthen EC contacts via connections to the cytoskeleton through the action of catenins (Dejana, 2004). For example VE-cadherin, the main EC adherens junction glycoprotein interacts with ZO-1 for actin cytoskeleton anchoring (Dejana et al., 2008). Moreover, VE-cadherin is supposed to play a role in maintaining barrier function through a process involving signaling of endothelial cell migration and angiogenesis (Tornavaca et al., 2015). N-cadherin functions in the interaction of ECs with pericytes, which additionally increased the tightness of the BBB (Gerhardt, 1999). PECAM1 (platelet EC adhesion molecules), a cellular adhesion and signaling receptor was shown to be involved in endothelial cell migration and leukocyte emigration (Woodfin et al., 2007).

5.1.1.3 Transport across the BBB

Due to the complex structure of tight and adherens junctions at the intercellular cleft of the ECs, paracellular transport is highly restricted (Figure 5.2a; Abbott et al., 2006). However, transcellular diffusion of some small lipophilic components (e.g. nicotine or alcohol) is possible (Figure 5.2b). Transport across the BBB mainly requires specific proteins or vesicle-mediated transcytosis (Abbott et al., 2006). Transport proteins such as nutrient transporters are very important for the metabolic supply of the CNS (Figure 5.2c). Nutrient transporters for primary metabolites of the CNS belong to the solute carrier (SLC) superfamily. Glucose is transported via glucose transporters with

GLUT1 (*Slc2a1*) as the most abundant one. (Yudilevich and De Rose, 1971; Zlokovic, 2008). Monocarboxylate transporters (MCT) comprise a family of 14 isoforms (Halestrap, 2013). MCT1 (*Slc16A1*), as the most abundant one, is expressed in all brain cells with the highest expression found in endothelial cells (Zhang et al., 2014). MCT1, MCT2 and MCT4 (*Slc16A3*) function in the transport of lactate and ketone bodies (acetoacetate and β-hydroxybutyrate). Furthermore, MCT1 and MCT2 are able to transport pyruvate (Halestrap, 2013). Efflux transporters in contrast to import transporters (e.g. SLCs) require energy in form of ATP for transport. The efflux transporter P-glycoprotein is largely responsible for the excretion of xenobiotics or undesired side products. (Figure 5.2c)(Barar et al., 2016).

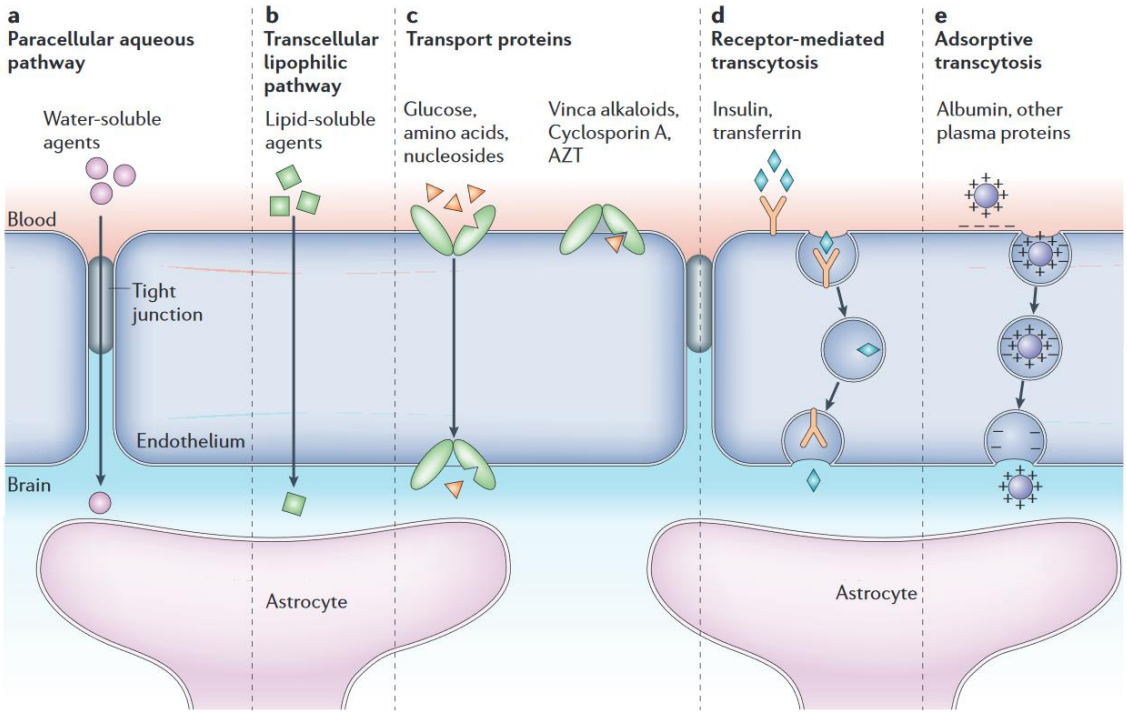

Figure 5.2l Transport routes across the BBB. (a) Paracellular transport is highly restricted for only very small aqueous molecules (e.g. hydrogen). **(b)** Transcellular passage through ECs can be performed by lipid-soluble agents. **(c)** Either influx or efflux of proteins is facilitated via transport proteins. Transcytosis can be divided in **(d)** receptor-mediated, by binding of a peptide to a receptor at the luminal membrane of the EC or **(e)** adsorptive, by the direct binding to the plasma membrane followed by vesicle invagination. (taken from Abbott et al., 2006)

Furthermore, ECs contain vesicular transport systems, which include the function of either caveolae or clathrin-coated vesicles (Hervé et al., 2008). The vesicular transport of peptides with endocytic carriers is divided in receptor-mediated transcytosis and adsorptive transcytosis (Abbott et al., 2006). The receptor-mediated transport is mediated by the binding of the peptide to the receptor at the luminal

membrane. This process initializes the transcytosis of the receptor–peptide complex in vesicles until the peptide is released at the abluminal membrane. Well known compounds for receptor-mediated transport are transferrin and insulin (Figure 5.2d) (Xiao and Gan, 2013). Adsorptive transcytosis is the main transport system for soluble plasma protein such as albumin. Cationized albumin interacts with the luminal membrane for vesicular transport through the EC (Figure 5.2e).

5.1.1.4 Mediators of BBB breakdown

Disturbances of barrier function were shown to be associated with diverse CNS diseases (Brown and Davis, 2002; Chodobski et al., 2012; Sweeney et al., 2018). Since usually several factor are involved in BBB disruption upon CNS diseases, inflammation and important inflammatory mediators such as increased matrix metalloproteinase activity and hypoxia are discussed in the following (Kaur and Ling, 2008; Varatharaj and Galea, 2017).

5.1.1.4.1 Inflammation

CNS inflammation is highly associated with disease expression and increased BBB permeability. One possibility for the systemic induction of inflammation is the application of the immunogenic, bacterial component lipopolysaccharide (LPS) (Varatharaj and Galea, 2017). LPS challenging of bovine ECs causes a reduction in barrier resistance, which might be due to increased EC eicosanoid production (de Vries et al., 1996). Eicosanoids are oxidized fatty acids that are produced by the enzyme cyclooxygenase and function in cell signaling such as regulation of inflammation and control of blood pressure (Spector, 1989). Furthermore, cyclooxygenase activity can be influenced by diverse stimuli such as cytokines abundance (de Vries et al., 1997), which makes LPS a suitable model to investigate early changes during inflammation. In response to *in vivo* LPS treatment, increased tracer penetration was associated with the translocation of occludin and ZO-1 from the EC membrane into the cytosol without any alteration in claudin-5 (Banks et al., 2015). Furthermore, *in vitro* BBB disruption by LPS seems to be independent of

pericyte and astrocyte function, since co-cultures did not provide an ameliorating effect. However, depending on the applied LPS dosage, endothelial cell death (Karahashi et al., 2009) as well as astrocyte loss (Cardoso et al., 2015) were reported. LPS treatment of a human EC line results in increased expression of MMP-2 and induction of the p38MAPK/JNK pathways which lead to decreased mRNA levels and protein abundance of occludin (Qin et al., 2015). Pro-inflammatory cytokines are produced by diverse brain cells such microglia, astrocytes, and ECs upon inflammation. The predominant cytokines during CNS inflammation and injury that have been studied in the context of BBB damage are tumor necrosis factor (TNF), interleukin-1 (IL-1), and interleukin-6 (IL-6) (de Vries et al., 1997). *In vitro* application of TNF, IL-1 and IL-6 on primary ECs caused the downregulation of claudin-5 m-RNA (Camire et al., 2015) with involvement of the PI3K/AKT pathway (Camire et al., 2014). Additionally, it has been shown that occludin is internalized via caveolin-1-dependent mechanism upon TNFα signaling (Marchiando et al., 2010) Application of the cytokine, interleukin 17 *(*IL-17), leads to a decreased abundance of occludin and ZO-1 (Kebir et al., 2007). Il-17 was further shown to induce EC reactive oxygen species (ROS) production, resulting in the downregulation of occludin (Huppert et al., 2010). IL-1β decreased sonic hedgehog signaling, which is important for tight junction expression and increased cytokine production in astrocytes, finally causing enhanced BBB permeability (Wang et al., 2014). Moreover, the chemokine CCL2 was able to induce internalization of occludin and claudin-5 mediated via lipid raft/caveolin-1 endocytosis (Stamatovic et al., 2009). Together, CNS inflammation is highly associated with the increase in cytokines, dysregulation of BBB maintenance molecules such as sonic hedgehog and induction of MMP activation, leading to BBB disruption.

5.1.1.4.2 Matrix metalloproteinases

Middle cerebral artery occlusion (MCAO), an ischemic stroke model provides a suitable model to analyze matrix metalloproteinase (MMP) function on BBB dysregulation (Durukan and Tatlisumak, 2007). Mice challenged by MCAO, developed BBB disruptions associated with the upregulation of the MMPs (Lenglet et al., 2014). Furthermore, rats challenged with MCAO revealed increased mRNA and protein abundance of MMP-2, which was shown to be responsible for the early

phase of BBB disruption, whereas MMP-9 was involved in progression of BBB damage. Moreover, increased MMP abundance was associated with claudin-5 and occludin degradation including fragments found in astrocytes. Inhibition of MMP function by BB-1101 prevented BBB breakdown and preserved tight junction structure (Yang et al., 2007). MMP2 was further shown to be directly involved in the degradation of occludin, whereas caveolin (Cav-1) induced endocytosis of claudin-5 caused its dissociation from the cytoskeleton (Liu et al., 2012). Additionally to MMP-9 function in tight junction degradation *in vitro* and *in vivo* (claudin-5, occludin, ZO-1), MMP-9 was shown to be responsible for the degradation of basal membrane components (laminin, collagen, fibronectin) (Lakhan et al., 2013). Taken together, MMP activation causes the degradation of tight junction proteins and basal lamina components, which leads to increased BBB permeability.

5.1.1.4.3 Hypoxia

Hypoxia-induced HIF1 signaling was shown to be involved in BBB disturbances (Kaur and Ling, 2008). HIF1, the main regulator of hypoxia, contains an oxygen-inducible α-subunit and a nuclear located subunit Hif1β. Under normoxic conditions HIF1α is constantly marked for proteasomal degraded by prolyl hydroxylases (PHD1-3, genes *Egln1-3*). Upon hypoxia, the expression of PHD1-3 is inhibited, leading to HIF1α stabilization. Consequently, HIF1α can bind to Hif1β to form a functional transcription factor that promotes the expression of HIF1 target genes, including VEGF (Vascular endothelial growth factor), MMP2 and GLUT1 (Ziello et al., 2007). Furthermore, VEGF signaling affects the expression of the tight junction protein, occludin (Zhao et al., 2014). In an *in vivo* approach of posthypoxic reoxygenation, BBB function determined by tracing labeled sucrose showed increased permeability that was associated with reduced protein abundance of the tight junction proteins occludin and ZO-1 with unaltered expression levels (Witt et al., 2003). Hypoxia induced reduction in ZO-1 abundance, localization and expression was caused by elevated levels of VEGF (Fischer et al., 2002). Further, in an ischaemia model hypoxia induction caused disturbances in ZO-1 and claudin-5 localization with unaffected occludin abundance. Inhibition of HIF1 with the use of siRNA prevented BBB breakdown (Chen et al., 2009). Moreover, hypoxia induced the decrease in claudin-5, occludin and ZO-1 protein abundance, which was rescued for claudin-5

and occludin after 24h reperfusion (Chen et al., 2012). Taken together, hypoxia induces BBB disruption by reducing tight junction protein abundance. HIF1α target genes (e.g. VEGF) might provide indication on the mechanism of hypoxia induced BBB disruption.

In summary, BBB disruption can be caused by a variety of factors, including induction of pro-inflammatory cytokines, MMP activation, ROS production and hypoxia induced HIF1α signaling. In CNS diseases usually several of these factors contribute to disease progression and persistent BBB dysfunction.

5.1.1.5 Manipulation of the BBB

In addition to the development of new pharmaceuticals for CNS diseases, one major challenge includes the application of therapeutically relevant concentrations into the brain (Pardridge, 2007). Therefore, treatment strategies focused on the manipulation of BBB function to increase drug entry for a predictive duration. One of the first attempts for the chemical manipulation of BBB function was the osmotic disruption of tight junctions by infusion with urea or mannitol (Brightman et al., 1973; Siegal et al., 2000). This approach reversibly opened the BBB, but challenges like undesired entry of other substances and long-lasting disruption of tight junctions for several hours unraveled the disadvantage of the system (Kemper et al., 2004; Kroll and Neuwelt, 1998). Analysis of the microvascular brain structure of frogs revealed increased permeability after administration of bradykinin, an inflammatory and neurovascular mediator (Olesen and Crone, 1986). Mimicking bradykinin function by the application of RMP-7, an agonist that binds to the bradykinin receptor localized on endothelial cells, revealed opening of the BBB for a shorter time period compared to osmotic disruption (Sanovich et al., 1995). In a rat tumor model RMP-7 application in combination with the chemotherapeutic agent carboplatin enhanced carboplatin entry, which was associated with increased survival (Matsukado et al., 1996). Nevertheless, clinical application for cancer therapy with a combination of RMP-7 and a chemotherapeutical showed unaltered tumor progression in malignant glioma, possible due to insufficient RMP-7 dosages (Prados et al., 2003). A synthetically modified E-cadherin peptide (His-Ala-Val; HAV) is able to modulate BBB function by the inhibition of the interaction between E-cadherin proteins in the intercellular cleft of ECs (On et al., 2014). Moreover, changes in BBB permeability were detected

already after three minutes treatment with the duration of only one hour. A first report of a treatment approach in glioblastoma revealed elevated drug entry into the brain (On et al., 2017). For the neurotransmitter glutamate it was shown that it increases barrier permeability by the activation of NMDA-receptors, which was prevented by the application of an antagonist (Attwell et al., 2010; Vazana et al., 2016). A hypothesis for the increased BBB permeability was reported by the enhancement of calcium flux and nitric oxide levels within or adjacent to microvascular structures, which might lead to reorganization or altered regulation of tight junction proteins. Furthermore, NMDA activation via high-intensity magnetic stimulation provided a non-invasive tool to manipulate BBB function in rats with an increase in the delivery of penicillin to the neural tissue. Moreover, a preclinical trial with malignant glioma patients using dynamic contrast-enhanced MRI revealed increased permeability in the tumor area, the peritumoral area und even the contralateral hemisphere (Vazana et al., 2016). Another approach to enhance drug entry in the CNS is the encapsulation of therapeutic agents in biodegradable nanoparticles (Hernández-Pedro et al., 2013). A major advantage of nanoparticles for drug delivery into the CNS is the possibility to engineer labeled nanoparticles that are recognized by specific receptors for targeted delivery of e.g. chemotherapeutic drugs for glioma therapy (Lee, 2017). A clinical trial of glioblastoma multiforme patients using magnetic nanoparticles for targeted thermotherapy in glioma cells with combined radiotherapy revealed a median survival of 23 month (Maier-Hauff et al., 2011). The extended survival of 23 month compared to the 15 month with a standard treatment for glioblastoma multiforme (Stupp et al., 2005) providing future perspectives for nanoparticle therapy in glioblastoma treatment.

Interestingly, volatile anesthetics such as isoflurane and sevoflurane were shown to manipulate BBB function (Acharya et al., 2015; Tétrault et al., 2008), which are described in the next chapter (5.1.2 Isoflurane).

5.1.2 Isoflurane

In addition to the above described mechanism of BBB manipulation, volatile anesthetic agent such as isoflurane and sevoflurane were shown to increase BBB permeability. Isoflurane is a widely used inhalational anesthetic agent of the halogenated ether group. It was shown to increase tracer entry into the brain of cats

in a dose dependent manner (1% and 3% isoflurane concentration) (Tétrault et al., 2008). Isoflurane and sevoflurane anesthesia were shown to cause BBB disruption in elderly rats (1-3% isoflurane anesthesia for 3h) (Acharya et al., 2015). Furthermore, sevoflurane anesthesia altered luminal endothelial cell surface morphology with indications for endothelial cell death. BBB disruption was persistent even after 24h recovery. These results are supported by the finding that isoflurane applied in elderly mice increased the abundance of pro-inflammatory cytokines such as TNF, Il-6 and Il-1β (1.4% isoflurane for 2h) (Wu et al., 2012). Further it was shown that isoflurane enhances HIF1 signaling in primary hippocampal neurons (1.2% isoflurane for 12 h) (Chai et al., 2016). These findings are in accordance with the assumption that isoflurane can cause neurotoxicity (Jiang et al., 2012; Lemkuil et al., 2011). Moreover, during sevoflurane and isoflurane anesthesia in an experimental brain trauma model in mice tight junction abundance of ZO-1 and claudin-5 was decreased, whereas tight junctions of healthy control animals were unaffected (1.5% isoflurane or 3.5% sevoflurane for 20min) (Thal et al., 2012). Aged rats treated with isoflurane showed decreased expression of occludin (1.5% isoflurane for 4h) (Cao et al., 2015). A mechanism of isoflurane function in BBB breakdown has been postulated by Zhao and others in an *in vitro* approach, which showed that isoflurane increased the abundance of HIF1α inducing the expression of the target genes *Vegf* and *Tgf-β3* (0.5-2.5% isoflurane for 3-6h). In the following, VEGF and TGF-β3 cause the reduction of occludin expression and internalization, respectively (Zhao et al., 2014).

Taken together, isoflurane (and sevoflurane) modulate BBB function by targeting tight junction stability. Furthermore, the concentration of the anesthetic agent and the duration of the treatment highly influence the extent of the permeability and the impact on tight junction stability. For example 1.5% isoflurane anesthesia for 4h decreased occludin expression (Zhao et al., 2014), whereas 20min of 1.5% isoflurane treatment showed unaffected tight junctions (Thal et al., 2012). Therefore, highly regulated use of isoflurane anesthesia might provide a suitable system to manipulate BBB function to increase the brain entry of pharmaceutical agents.

5.1.3 Glioblastoma multiforme

5.1.3.1 Disease and therapy

Primary brain tumors, referred to as gliomas, are named after their originating cell like e.g. astrocytoma, oligodendrogliomas, ependymomas and glioblastoma. In general, gliomas are classified into four categories: grade I, II, III and IV by the WHO (World Health Association) according to their growth pattern and malignity. Glioblastoma multiforme (GBM) is the most common form of grade IV brain tumors, which is characterized by an aggressive growth pattern, enhanced tumor outgrowth into surrounding tissue, autonomous vasculature and a necrotic tumor center (Davis, 2016). The incidence to develop a glioblastoma is 3.2/100.000 population with a poor prognosis of a median survival of 15 month (Hanif et al., 2017). GBMs are mainly spontaneous arising tumors and only 1% of GBMs are reported to be hereditary (Schwartzbaum et al., 2006). Genetic diseases such as tuberous sclerosis or multiple endocrine neoplasia as well as physical brain injuries were shown to cause the development of glioma (Urbanska et al., 2014). Further, increased expose to ionizing radiation provides a risk factor for the development of GBM (Hanif et al., 2017). GBM are developed at all ages with 64 years as the average age of diagnosis (Ostrom et al., 2013). The standard treatment for GBM is surgical resection followed by radiotherapy and chemotherapy; however additional chemotherapy only prolonged patients' survival of about 3 month in contrast to radiotherapy alone (Stupp et al., 2005).

The most common used chemotherapeutic agent is temozolomide, since it is able to pass the BBB (Koukourakis et al., 2009). Temozolomide is hydrolyzed resulting in the active form methyl-triazeno imidazole-carboxamide (MTIC), which acts by methylation of DNA causing cytotoxicity (Newlands et al., 1997). Due to the short half-life of temozolomide (1.5h/plasma) (H.-L. Liu et al., 2014) systemic administration needs to be performed at high doses, which cause varies side effects, such as headache and nausea (Zhang and Gao, 2007). Furthermore, as stated above, temozolomide only shows minor benefit on patients' survival. Another antineoplastic drug used in clinical trials is the intercalating agent, carmustine, which acts by crosslinking DNA strands that blocks DNA repetition. After surgical resection of the tumor, carmustine incorporated in a degradable reservoir enables local application. Unfortunately, carmustine treatment only provided a minor benefit for

patients with the undesired side effect of increased CSF leak, which could facilitate infections (Nagpal, 2012; Westphal et al., 2003). A well-known chemotherapeutic agent is cisplatin that is successfully used to treat diverse cancer types outside the CNS, such lung or ovarian cancer (Shaloam Dasari and Paul Bernard Tchounwou, 2015). Cisplatin functions similar to carmustine, by crosslinking DNA strands thereby inhibiting DNA repetition and repair. Undesired side effects like nephrotoxicity and especially the disability to penetrate functional BBB illustrate the weakness of cisplatin for glioblastoma treatment (Shaloam Dasari and Paul Bernard Tchounwou, 2015). However, another study postulated efficacy against brain tumors e.g. medulloblastoma (Gottardo and Gajjar, 2008).
In addition to the development of new chemotherapeutic agents, the main challenge in the treatment of GBM is the achievement of effective doses within the tumor and the surrounding tissue, since GBM are vulnerable for spreading and reoccurrence (Cooper et al., 2015).

5.1.3.2 Gl261 glioblastoma cell line

Spontaneous development of CNS tumors in rodents is extremely rare (Fitzgerald et al., 1974; Fraser, 1971). Animal models include: transgenic models, virus-induced tumors, transplantation of human glioma cells in immunocompromised mice and transplantation of murine glioma cell line in syngeneic mouse models (Peterson et al., 1994). The main benefit of transplantation studies using a glioma cell line is the high reproducibility with a predictable tumor growth pattern. Transplantation studies of a murine glioma cell line in a syngeneic mouse model further provides the advantage to avoid the additional treatment of mice with immunocompromising agents.
A well-known cell line for transplantation studies is the Gl261 mouse glioblastoma cell line that was established using chemical induction with methylcholanthrene (Ausman et al., 1970). Intracranial implanted C57BL/6 mice with 1x 10^5 implanted Gl261 cells showed an invasive and angiogenic growth behavior with a medium survival of 25 days (Szatmári et al., 2006). Histological analysis of Gl261 tumors revealed a tumor with irregularly shaped borders and a few migrating tumor cells into surrounding tissue (Newcomb and Zagzag, 2009). However, the Gl261 tumor model provided still limitations, since the growth pattern is distinct from the highly invading,

spontaneously arisen glioma in human patients (Maes and Van Gool, 2011). Gl261 cells that express the fluorescent marker GFP provided the possibility to analyze histologically tumor size and single cell outgrowth in Gl261 implanted tumor mice

5.1.4 Aim of the study

GBM is the most common malignant brain tumor that is characterized by an invasive growth pattern, autonomous vasculature and a necrotic tumor center (Davis, 2016). Standard treatment for GBM includes surgical resection followed by radiotherapy and chemotherapy with only minor impact on patients' survival. The major challenge in the chemotherapeutic treatment of patients is the application of therapeutically relevant concentrations into the brain (Pardridge, 2007).

In this study the first aim was to analyze the potential of the volatile anesthetic agent isoflurane to manipulate BBB permeability. Therefore, biochemical quantification of tracer entry was performed with different isoflurane concentrations. Additionally, transcriptional changes were investigated after short-term and long-term isoflurane treatment. Moreover, late effects after short-term isoflurane treatment were analyzed. Analysis of tight junction protein abundance was performed by antibody labeling. In the second part, Gl261 glioblastoma cells were transplanted into wildtype mice. The chosen cell line was already proved to serve as a suitable model system for GBM research (Szatmári et al., 2006). Isoflurane induced enhancement of tracer extravasation in Gl261 cells transplanted tumor mice was quantified. In the third part, we focused on the development of a new therapeutic approach for GBM by the use of a combined treatment of cisplatin with isoflurane anesthesia to increase drug entry into the brain of Gl261 transplanted mice. After transplantation of Gl261 cells, mice were treated two times with the chemotherapeutic agent cisplatin with and without isoflurane anesthesia. Tumor growth was monitored twice by magnetic resonance imaging. For the readout of the therapeutic benefit, tumor volume, T-cell infiltration, tumor cell viability and the invasive phenotype of Gl261 cells was investigated. With our experimental design we wanted to answer the questions (1) whether isoflurane anesthesia can be used to manipulate BBB function in a confined period (2) whether isoflurane treatment can increase tracer/ drug entry into the brain of tumor mice and (3) whether a combined treatment of cisplatin and isoflurane can decrease tumor

viability and outgrowth, including the restriction of migrating tumor cells into surrounding tissue?

5.2 Results

5.2.1 Dose-dependent increase in BBB permeability after treatment with volatile isoflurane

The controlled flux of metabolites and the restrictive passage of biomolecules between the periphery and central nervous system is mediated by the BBB. Today, different systems to modulate BBB function have been studied with several advantages and disadvantages (Attwell et al., 2010; Bartus et al., 1996; Kemper et al., 2004; Lee, 2017; On et al., 2014; Vazana et al., 2016) (see chapter 5.1.1.5). One novel approach to modulate BBB function might be by the use of the anesthetic agent isoflurane. It has been shown that cats under isoflurane anesthesia exhibit an impairment of the BBB (Tétrault et al., 2008). The present work represents the investigation of isoflurane as a tool to modulate BBB function and further to enhance drug delivery in a glioblastoma mouse model.

First, we needed to analyze whether isoflurane treatment of wildtype mice increases tracer delivery into the brain. Therefore, Evans blue was i.v. injected into the tail vein of wildtype mice and allowed to circulate with 1%, 4% isoflurane treatment or oxygen for 1h. Interestingly, the results indicate that isoflurane treatment increases Evans blue extravasation into the brain (Figure 5.3a). Furthermore, 4% isoflurane treatment seemed to be more effective to enhance tracer extravasation than 1% isoflurane. Next, to analyze the duration and the indicated dose-response of isoflurane treatment, a biochemical quantification of Evans blue extravasation was performed with a novel developed approach (Berghoff et al., 2017a). Notably, the results revealed a significant dose-dependent increase in blood-brain-barrier permeability of isoflurane treated animals (O_2 3.1±0.05 EB µg/g dry weight compared to 1% isoflurane 4.2±0.32 and 2.5% isoflurane 5.7±0.27) (Figure 5.3c). Further, Evans blue application after the withdrawal of isoflurane showed an extravasation level comparable to oxygen treated controls (O_2 3.1±0.05 EB µg/g dry weight compared to 3.1±0.48 after the withdrawal of isoflurane). The brain water content, as a measure of edema formation, was unaffected by isoflurane treatment, excluding edema as a cause of increased blood-brain-barrier permeability (Figure 5.3d).

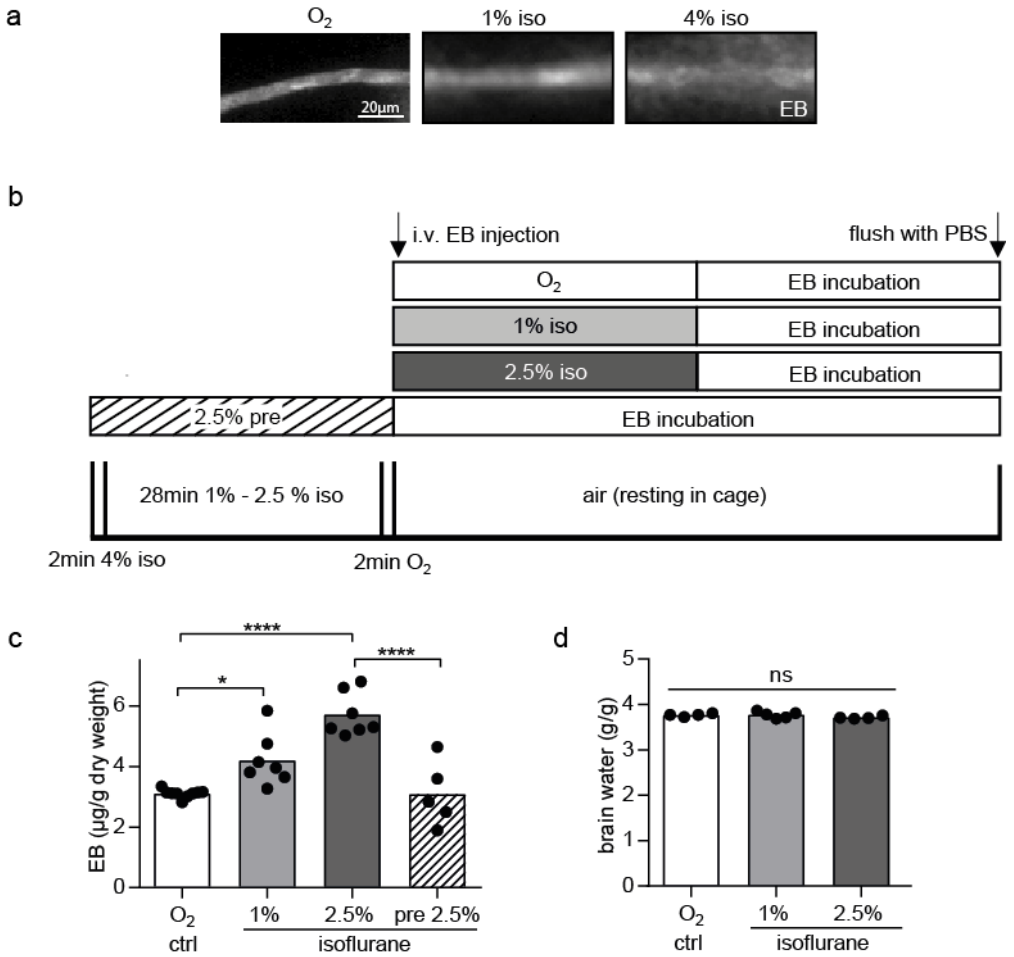

Figure 5.3l Dose dependent increase of Evans blue extravasation in isoflurane treated animals. (a) Evans blue extravasation on sections of the striatum. Control animals were treated with oxygen. Isoflurane anesthesia was applied in two concentrations, 1% and 4% isoflurane for the duration of 1h. **(b)** Treatment scheme for the biochemical quantification assay of Evans blue extravasation after isoflurane application. Evans blue extravasation was quantified for 1% and 2.5% isoflurane as well as under oxygen treatment alone. Furthermore, Evans blue extravasation was analyzed after the withdrawal of 2.5% isoflurane. Isoflurane treatment was performed as followed: The mouse was put to sleep with 4% isoflurane for 2min. Afterwards the respective treatment with 1% or 2.5% isoflurane was performed for 28min followed by 2min oxygen to allow the mouse to wake up and recover from anesthesia. Evans blue was allowed to circulate for the total duration of 1h. For the isoflurane recovery experiment, Evans blue was applied directly after the recovery of the mouse with 2min oxygen. For comparable results, Evans blue circulation was performed for 1h. **(c)** Biochemical quantification of Evans blue extravasation in control and isoflurane treated mice (n=5-9). One-way-ANOVA with Tukey's multiple comparison test was performed **(d)** Quantification of brain water content in control and isoflurane treated mice (n= 4-5). One-way-ANOVA with Tukey's multiple comparison test was performed. Differences were considered significant with a P-value of *, P<0.05; **, P<0.01; ***, P<0.001; ****, P<0.0001; ns = not-significant. (Evans blue quantification was done together with Stefan Berghoff).

These data indicate that 2.5% isoflurane treatment modulates BBB tracer application for the duration of 30min (referred to as short-term) in a sufficient manner. Additionally, tracer application after the withdrawal of isoflurane revealed an extravasation level of oxygen treated control mice, suggesting unaltered BBB modulation.

5.2.2 BBB modulation after short-term isoflurane treatment functions via a hypoxia independent pathway

The BBB is mainly formed by endothelial cells which are connected to each other via belt-like tight junctions. Alterations of tight junction abundance or distribution disrupt BBB function (Coisne and Engelhardt, 2011). It has been shown that long-term isoflurane treatment in an *in vitro* approach stabilizes the main regulator of hypoxia Hif1α, which triggers *Vegfα* and *Tgfβ3* expression and this affects the expression of the tight junction protein, occludin (*Ocln*) (Zhao et al., 2014). Therefore, it is highly presumable that long-term isoflurane treatment *in vivo* enhances hypoxia induced gene expression. In contrast acute transcriptional changes are unknown. Therefore, we wanted to analyze early changes in the transcriptional expression level of mice treated with 2.5% isoflurane for 30min (short-term). Three additional control groups were added: (1) the first cohort was treated for 30min with the carrier gas oxygen (2) the second group was treated with 2.5% isoflurane for 3h (long-term) as positive control (3) the third cohort was treated with 2.5 % isoflurane for 30min followed by 2.5h recovery and served as a control group for possible long-term effects.

After long-term isoflurane treatment, the expression of *Cldn5* was significantly increased (*Cldn5* oxygen 1.0±0.09 rel. exp. and after 3h isoflurane 2.1±0.41) and ZO-1 (*Tjp1*) was slightly downregulated (*Tjp1* oxygen 1.0±0.04 rel. exp. and after 3h isoflurane 0.71±0.15) (Figure 5.4a). Occludin expression was unaltered, but Hif1α signaling changed after long-term isoflurane treatment with an increase in both *Vegfα* and *Tgfβ3* expression (*Vegfα*: oxygen 1.0±0.04 rel. exp. and after 3h isoflurane 1.8±0.28 and *Tgfβ3*: oxygen 1.0±0.05 and after 3h isoflurane 1.7±0.17), indicating hypoxic conditions (Figure 5.4b). Under normoxic conditions Hif1α is marked for degradation by proline-hydroxylases 1-3 (gene *Egln1-3*), whereas during hypoxia the expression of these enzymes is inhibited. Therefore, the expression level of *Egln1-3* was tested showing decreased expression of all *Egln* genes for the 3h time-point (Figure 5.4c). Additionally after long-term treatment, *Hif1α* expression was downregulated (*Hlf1α* O_2: 1.0±0.03 rel. exp. and after 3h isoflurane 0.57±0.14).

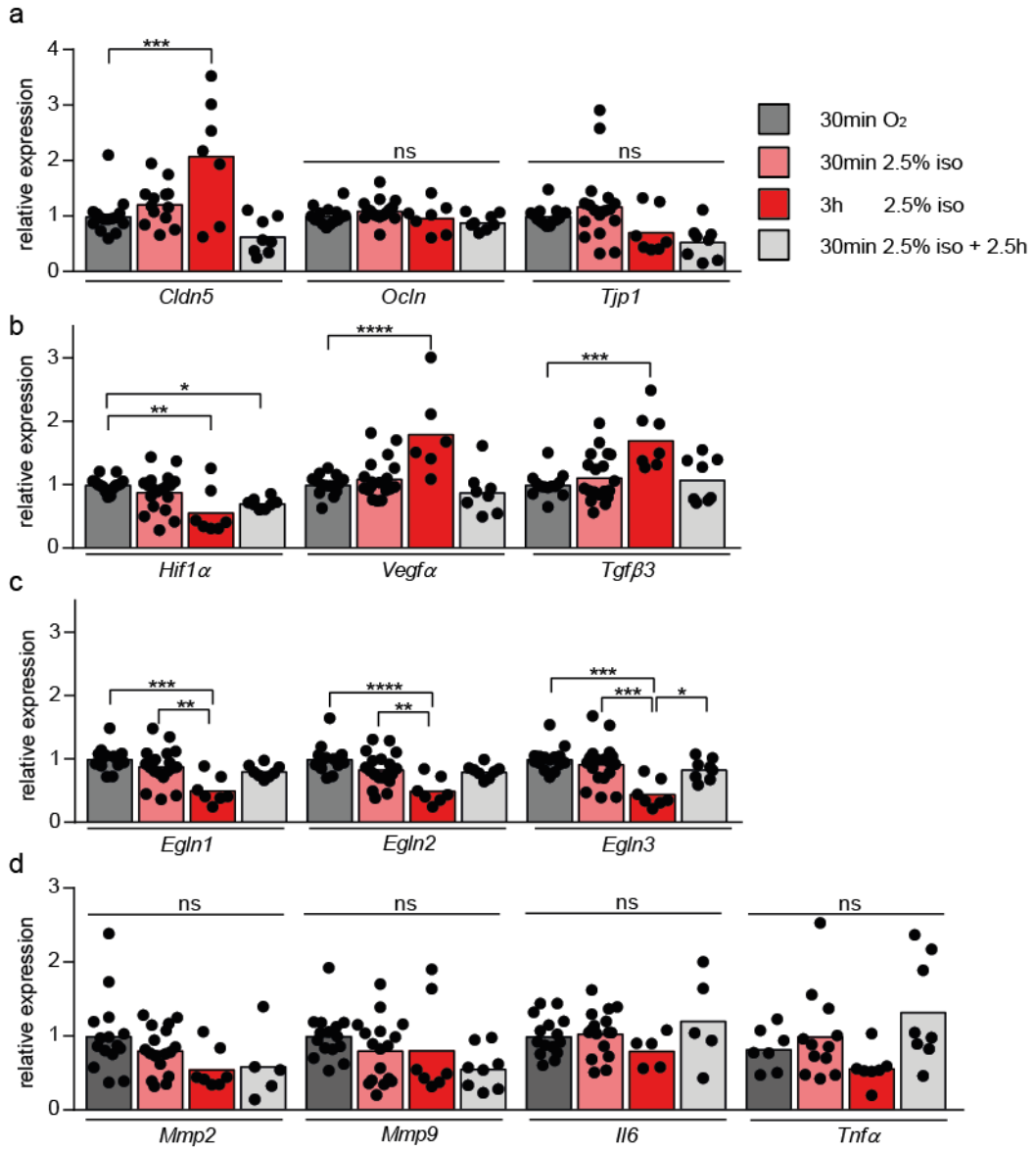

Figure 5.4l Expression level of tight junction proteins, Hif1α signaling, MMPs and pro-inflammatory cytokines in isoflurane treated animals. (a) Quantitative RT-PCR on striatum and thalamus determining expression of the tight junction proteins, *Cldn5*, *Ocln* and *Tjp1*, **(b)** markers for hypoxia/Hif1a signaling, *Hif1α*, *Vegfα* and *Tgfβ3* **(c)** Hif1α degrading enzymes Phd1-3 (*Egln1-3*) **(d)** and markers for MMPs and pro-inflammatory cytokines, *Mmp2*, *Mmp9*, *Il6* and *Tnfα* (n= 5-18). One-way ANOVA of each gene with Tukey's multiple comparison test was performed and normalized to *RplpO*. Furthermore, treatment cohorts were normalized to oxygen treated wildtype controls. Differences were considered significant with a P-value of *, P<0.05; **, P<0.01; ***, P<0.001; ****, P<0.0001; ns = not-significant.

In summary these data suggest hypoxia induced changes in the expression level of tight junction genes after long-term isoflurane treatment. Claudin5 and ZO-1 showed alterations in the expression level after long-term isoflurane treatment. Occludin expression was unaltered in contrast to published data, which might reflect an earlier signaling state in our *in vivo* approach compared to the *in vitro* model by Zhao (Zhao

et al., 2014). Since Hif1α is highly regulated on protein level, western blot experiments must be performed to confirm this hypothesis.

In contrast to the 3h time-point, the expression level of the tight junction proteins claudin5, ZO-1 and occludin was unaltered after 30min isoflurane treatment (Figure 5.4a). Interestingly, hypoxia induced alterations in gene expression were not detectable, suggesting a different mechanism for BBB modulation after short-term isoflurane treatment compared to long-term treatment (Figure 5.4b/c).

Matrix metalloproteinases (MMP) are involved in BBB disruption in diverse CNS diseases (Rempe et al., 2016). MMPs function in the degradation of basement membrane proteins and tight junction proteins (Feng et al., 2011). Long-term isoflurane treatment has been shown to increase the expression of pro-inflammatory cytokines e.g. *tumor necrosis factor α* (*Tnfα*) and interleukin-6 (*Il6)* (Wu et al., 2012). Furthermore, pro-inflammatory cytokines were involved in disruption of occludin (Lv et al., 2010; Rochfort and Cummins, 2015). To investigate whether pro-inflammatory cytokines and MMPs contribute to isoflurane induced BBB modulation, transcriptional changes in the expression of *Mmp2*, *Mmp9*, *Il6* and *Tnfα* were analyzed (Figure 5.4d). Short-term isoflurane treatment of 30min as well as extensive isoflurane treatment for 3h revealed unaltered expression levels of MMPs and pro-inflammatory cytokines. These data imply that the isoflurane induced increase in BBB permeability does not function via the upregulation of pro-inflammatory cytokines or MMPs.

5.2.3 Decreased protein abundance of occludin and claudin5 after short-term isoflurane anesthesia

The expression level of tight junction proteins after short-term isoflurane treatment was unaltered, but the Evans blue extravasation assay showed increased tracer permeability. Therefore, we wanted to address the question, whether the abundance of tight junction proteins is decreased after isoflurane treatment. Pilot stainings of claudin5, ZO-1 and occludin on brain section of 30min and 3h isoflurane treated animals were performed and compared to oxygen treated controls. Preliminary results revealed reduced abundance of occludin and claudin5 after long-term isoflurane treatment (Figure 5.5).

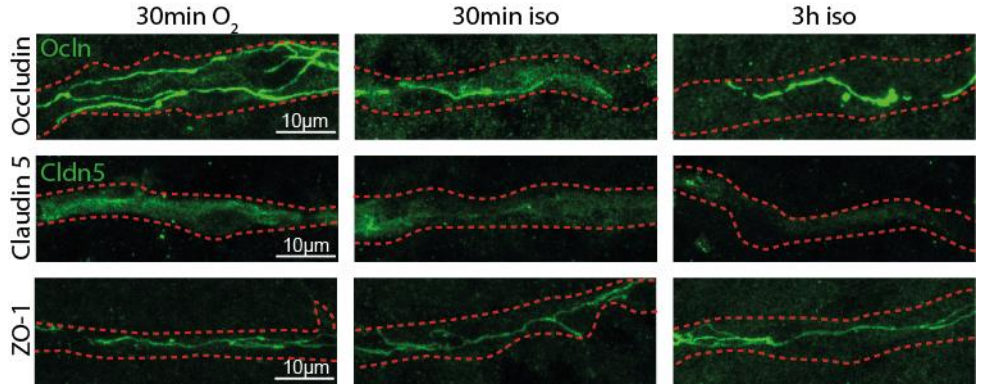

Figure 5.5**I Tight junction staining of isoflurane treated mice.** Pilot tight junction staining's were performed for single animals. Mice were treated for 30min with oxygen or isoflurane for 30min and 3h. Occludin (Ocln), claudin5 (Cldn5) and ZO-1 were depicted in green and the blood vessel is outlined in red. Scale bar 10µm.

Notably, already after short-term isoflurane treatment, occludin protein abundance showed a strong reduction compared to oxygen treated control mice and further claudin5 seemed to be slightly reduced. Stainings of ZO-1 revealed unaltered ZO-1 intensity in isoflurane treated mice compared to oxygen treated controls. Nevertheless, ZO-1 positive area per vessel (marked in red) seem to be reduced. Further staining's need to be performed to elucidate the abundance of ZO-1 in isoflurane treated animals.

Taken together these results suggest that isoflurane treatment decreases the abundance of occludin and claudin5, starting with 30min anesthesia and proceeding in the tested 3h time point.

5.2.4 Increased BBB permeability in a tumor mouse model after short-term isoflurane treatment

We showed that 2.5% isoflurane treatment for 30min provided the perfect tool to modulate BBB function for a restrictive duration to enhance Evans blue extravasation into the brain. Treatment strategies in the field to brain tumor research focus on applications to modulate BBB function to increase the permeability for chemotherapeutics (see chapter 5.1.1.5) (Kemper et al., 2004). Therefore, we wanted to investigate whether isoflurane can be used to increase *in vivo* extravasation of Evans blue in a brain tumor model. For that purpose, a glioblastoma mouse model was established in our laboratory (in collaboration with Dr. Petra Hülper). Mice were implanted with Gl261 glioblastoma cells (provided by Dr. Petra

Hülper) in the right hemisphere and the tumor was allowed to grow for 10 days. At day 10 mice were i.v. injected with Evans blue and treated either for 30min with 2.5% isoflurane or vehicle. Afterwards, brains were divided in right hemisphere (tumor) and contralateral, left hemispheres (w/o tumor) (Figure 5.6a). Further mice without transplantation served as control.

Previously it has been reported that the tumor area of Gl261 implanted cells in mice was permeable for Evans blue entry already after two weeks implantation (Leten et al., 2014). Therefore, elevation in Evans blue abundance in the tumor hemisphere of oxygen treated mice was expected (tumor hemisphere: control 2.33±0.04 EB µg/g dry weight compared to oxygen 3.3±0.08) (Figure 5.6b). However, this effect was not detected in the contra hemisphere (contralateral hemisphere: control 2.5±0.06 EB µg/g dry weight compared to oxygen 2.84±0.14). Interestingly, mice treated with isoflurane for 30min displayed not only an increase in Evans blue permeability in the contra hemisphere, but also a further increase in the tumor hemisphere (contralateral hemisphere: 3.69±0.09 EB µg/g dry weight tumor hemisphere 4.65±0.06) (Figure 5.6b).

These data suggest that 30min 2.5% isoflurane treatment might be feasible to enhance the delivery of chemotherapeutics not only to the tumor mass, but further to the whole brain tissue.

In order to analyze the influence of isoflurane on Gl261 cells, a WST-1 (water soluble tetrazolium salt) assay was performed, in which cell viability was quantified (performed by Nina Gerndt). The viability of Gl261 cells was highly affected with 1% isoflurane treatment (Figure 5.6c). Therefore, an isoflurane treated control group was added for later described experiments.

The cytostatic agent, cisplatin, is a widely used drug for the treatment of diverse solid cancer types, like lung or testicular carcinoma. It acts by DNA crosslinking and therefore induces apoptosis of any proliferating cell (Shaloam Dasari and Paul Bernard Tchounwou, 2015). To investigate the lowest feasible concentration to treat Gl261 cells, a dose-response assay with the use of the WST-1 system was performed (Nina Gerndt). The results revealed that cisplatin concentrations of 0.5µg/ml or lower showed unaltered Gl261 viability, whereas concentration of 5µg/ml or higher seemed to be highly efficient (Figure 5.6d). We decided for 2.5µg/ml as the lowest, feasible concentration of cisplatin for the use in the following experiments.

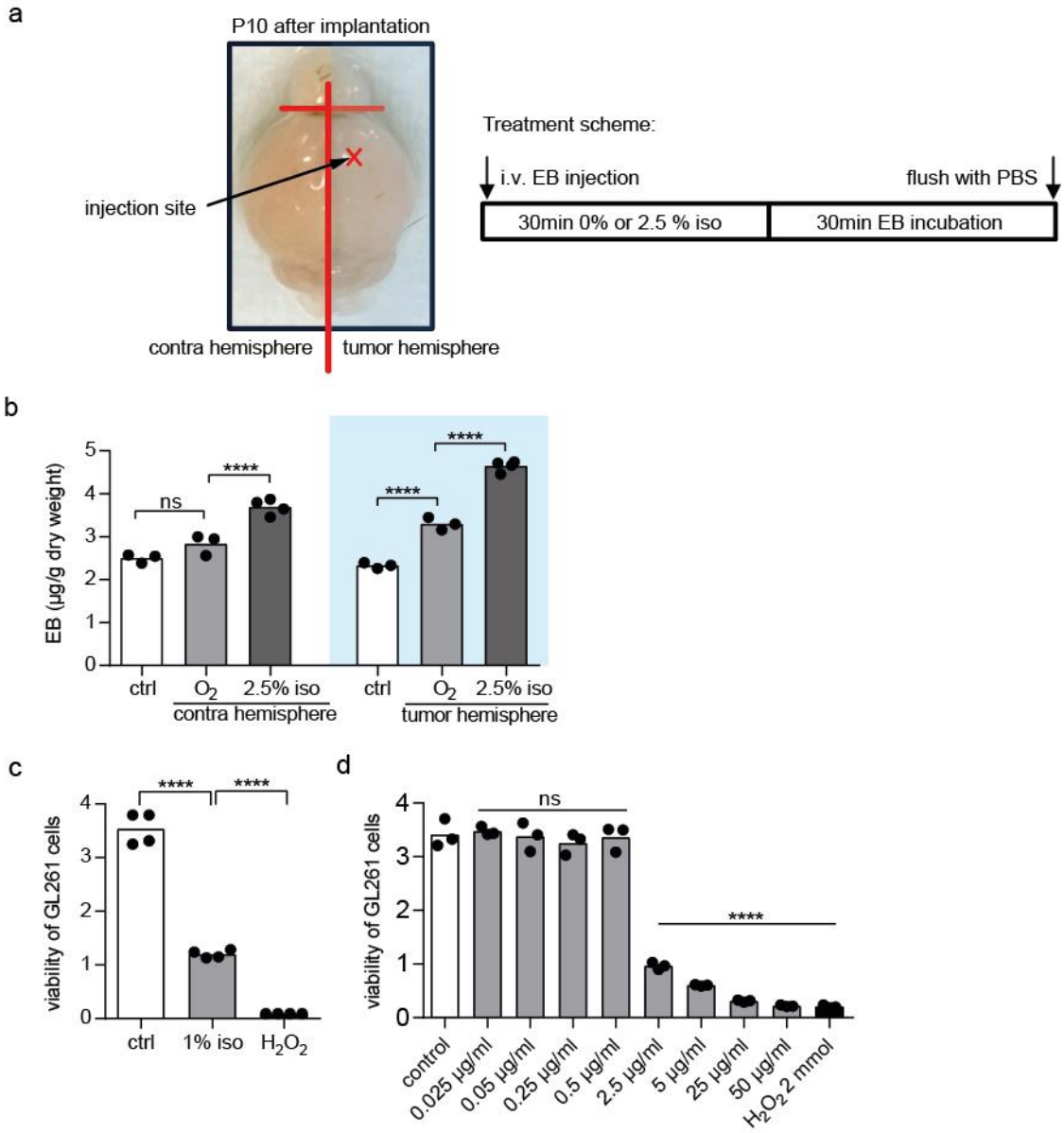

Figure 5.6l Isoflurane treatment increased BBB permeability in a glioblastoma mouse model. (a) Treatment scheme of brain tissue sectioning for the Evans blue extravasation assay **(b)** Biochemical quantification of Evans blue extravasation in control (O_2) and isoflurane treated mice (n= 3-4) implanted with Gl261 glioblastoma cells. One-way-ANOVA with Tukey's multiple comparison test was performed for the tumor hemisphere and the contralateral site. Results were compared to mice without tumor transplantation (b) WST-1 viability test of isoflurane treated Gl261 glioblastoma cells (n= 4). H_2O_2 served a positive control. **(c)** Dose-response curve of GL261 cells treated with cisplatin (n= 3). WST-1 system was used. Significance was quantified with one-way-ANOVA with Tukey's multiple comparison test. H_2O_2 served a positive control. Differences were considered significant with a P-value of ****, P<0.0001; ns = not-significant. (WST-1 assay was performed by Nina Gerndt; biochemical Evans blue quantification was done together with Stefan Berghoff).

5.2.5 Decreased tumor volume in cisplatin and isoflurane treated mice

Next, we wanted to investigate the impact of isoflurane initiated BBB modulation on the therapeutic action of cisplatin in our glioblastoma mouse model. GFP expressing Gl261 glioma cells were intrathecal implanted in the right hemisphere of wildtype mice. Tumor growth was controlled by MRI imaging techniques on day 7 (in collaboration with the Biomedizinische NMR Forschungs GmbH, Prof. Jens Frahm). Two treatment time-points were chosen on day 9 and day 11. Mice were i.v. injected with either cisplatin (3mg/kg cisplatin) or saline. Afterwards, mice of the isoflurane cohorts were treated with 2.5% isoflurane for 30 min under constant control of body temperature and respiration. Tumor volume was measured with a second MRI on day 13. On day 14 mice were perfused and immunohistological aspects of the different treatment paradigms were analyzed on brain tissue (Figure 5.7a). The experimental design comprised four treatment cohorts: (1) i.v. saline (2) i.v. saline with 2.5% isoflurane treatment for 30min (3) i.v. cisplatin (4) i.v. cisplatin with 2.5% isoflurane anesthesia for 30min.

Quantification revealed that isoflurane treatment without cisplatin showed unaltered tumor volume (saline: 3.05±0.26mm^2 compared to isoflurane 3.39±0.14mm^2) (Figure 5.7b). This suggests a different effect of isoflurane on the implanted Gl261 cells compared to the cultivated cells, which already showed decreased viability with 1% isoflurane treatment (Figure 5.6b).

Mice treated with cisplatin alone showed a slightly reduced tumor volume, but did not reach significance (saline: 3.05±0.26mm^2 compared to cisplatin 2.58±0.23mm^2). Notably, application of the combined treatment of cisplatin and isoflurane decreased significantly the tumor volume compared to all other tested groups animals by almost 50% (cisplatin + isoflurane 1.71±0.19mm^2).

In summary, quantification of tumor volume showed only a small effect for cisplatin treatment alone as expected. Since cisplatin is unable to pass the BBB, the treatment was limited to the BBB compromised tumor center. In contrast, the combined treatment with cisplatin and isoflurane highly decreased tumor volume. These results suggest that isoflurane treatment increased the penetration of cisplatin into whole brain tissue and thereby limited tumor outgrowth.

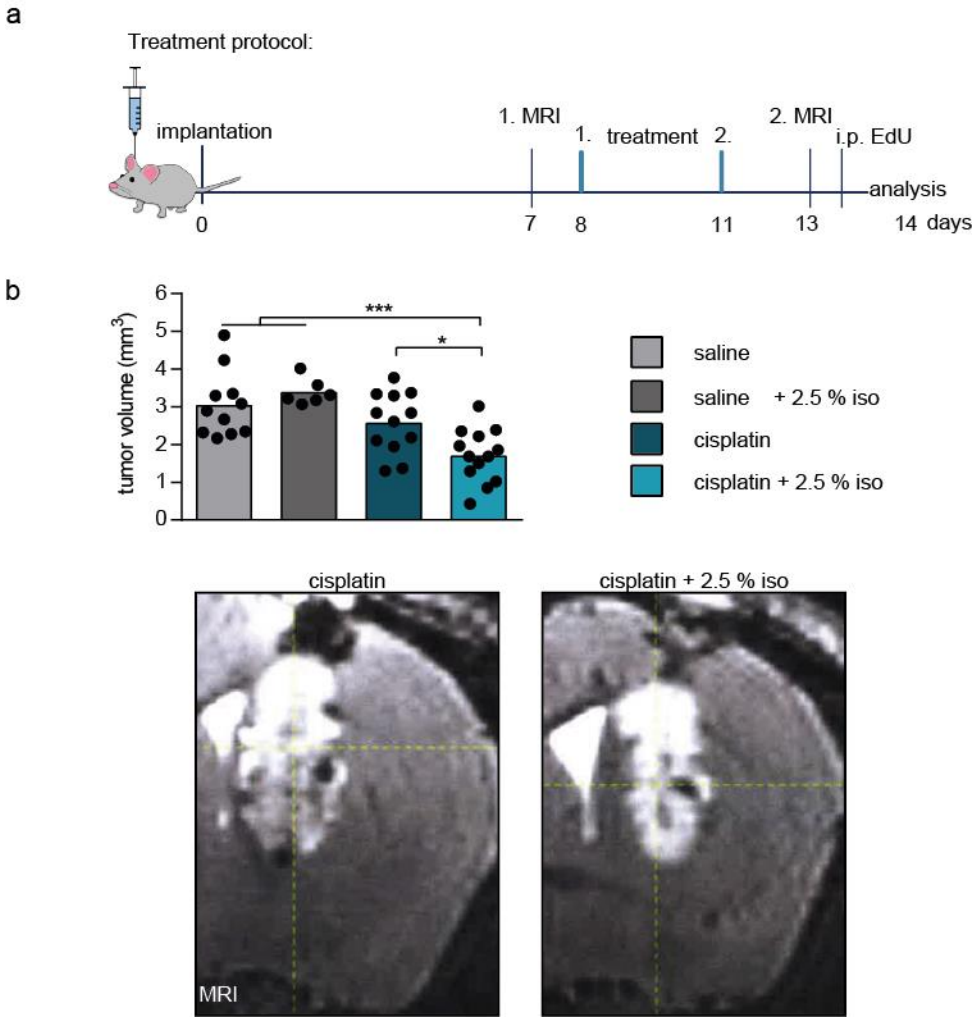

Figure 5.7l Reduced tumor volume in cisplatin and isoflurane treated glioblastoma mice. (a) Treatment protocol of the glioblastoma mouse model. Four treatment cohorts were analyzed (1) i.v. saline (2) i.v. saline with isoflurane (3) i.v. cisplatin (4) i.v. cisplatin with isoflurane (n= 6-13). **(b)** Quantification of MRI measurements: T_1-weighted MRI was used to quantify t*umor volume. Single images were analyzed,* positive tumor area selected and tumor volume was quantified with Amira Software. Significance was quantified with one-way-ANOVA with Tukey's multiple comparison test between all tested cohorts. MRI of one representative cisplatin and one cisplatin + isoflurane treated animal (performed by Thomas Michaelis, Takashi Watanabe and Sabine Höfer, Biomedizinische NMR Forschungs GmbH, Prof. Jens Frahm). Differences were considered significant with a P-value of *, P<0.05; ***; ns = not-significant.

5.2.6 Increased T-cell infiltration in the surrounding tumor area of cisplatin and isoflurane treated mice

It is known that human glioblastoma develop strategies to escape immune surveillance (Razavi et al., 2016). Therefore, quantification of T-cell numbers served as a first readout of the immune response in glioblastoma mice.

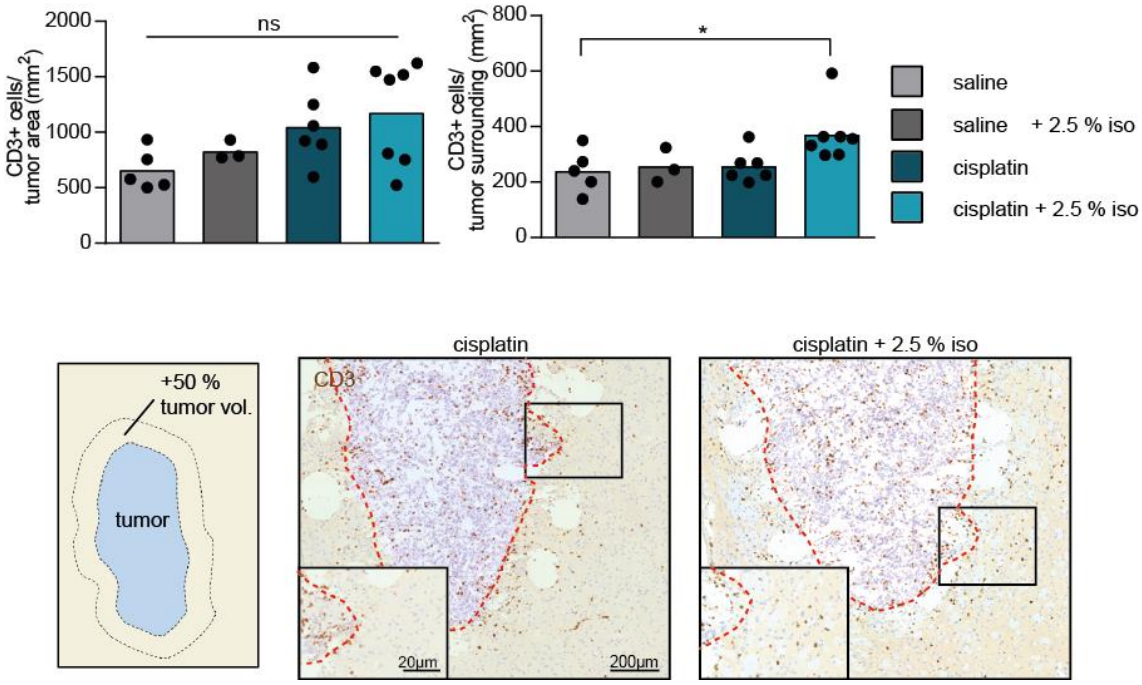

Figure 5.8l Increased numbers of T-cells in the tumor surrounding of cisplatin and isoflurane treated mice. Quantification of CD3 positive cells in tumor tissue and in tumor surrounding (tumor surrounding = + 50 % of the tumor area) of GI261 implanted mice treated with cisplatin or saline with or without additional 2.5% isoflurane treatment for 30min (n= 3-7). The tumor mass is outlined in red One-way-ANOVA with Tukey's multiple comparison test was performed for the tumor area and the tumor surrounding between treatment cohorts. Differences were considered significant with a P-value of *, P<0.05; ns = not-significant. Scale bar 200µm, selection 20µm.

CD3 (cluster of differentiation 3) staining was used as a marker for the T-cell lineage of tumor-infiltrating lymphocytes (Chetty and Gatter, 1994). To address the question if isoflurane treatment extended cisplatin delivery from the tumor mass to the tumor surrounding, CD3 positive cells within the tumor mass and the surrounding area were analyzed. A slight, but not significant increase in T-cell infiltration in the tumor mass of both cisplatin treated groups was detected as expected (saline: 658.8±81.9 CD3+/mm^2 compared to cisplatin 1050±137.8 and cisplatin + isoflurane 1178±174.7). Notably, only the combined treatment of cisplatin and isoflurane showed elevated numbers of CD3 positive cells within the tumor surrounding (saline: 240.4±35.4 CD3+/mm^2 compared to cisplatin + isoflurane 371±38.3) (Figure 5.8). In summary, both cisplatin cohorts revealed elevated immune response within the tumor area. Furthermore, the combined treatment of isoflurane and cisplatin caused an increased immune responsiveness in the tumor surrounding. This increased immune response in the combined cohort suggests that the modulation of BBB function by isoflurane enhanced cisplatin delivery to the tumor surrounding.

5.2.7 Reduced tumor cell viability in the combined treatment of cisplatin and isoflurane

Gl261 cells implanted in wildtype mice developed a highly proliferative phenotype in which the untreated tumor approximately doubled the size within six days (data not shown). To further address the question, whether the combined treatment of cisplatin and isoflurane shows reduced tumor proliferation, EdU (5-ethynyl-2′-deoxyuridine) was injected 16h prior to perfusion. Combined stainings of EdU for proliferating cells and TUNEL (Terminal deoxynucleotidyl transferase dUTP nick end labeling) for apoptotic cells were performed to determine the viability of the tumor cells. The viability was quantified by the ratio of apoptotic cells (TUNEL) vs. proliferating cells (EDU).

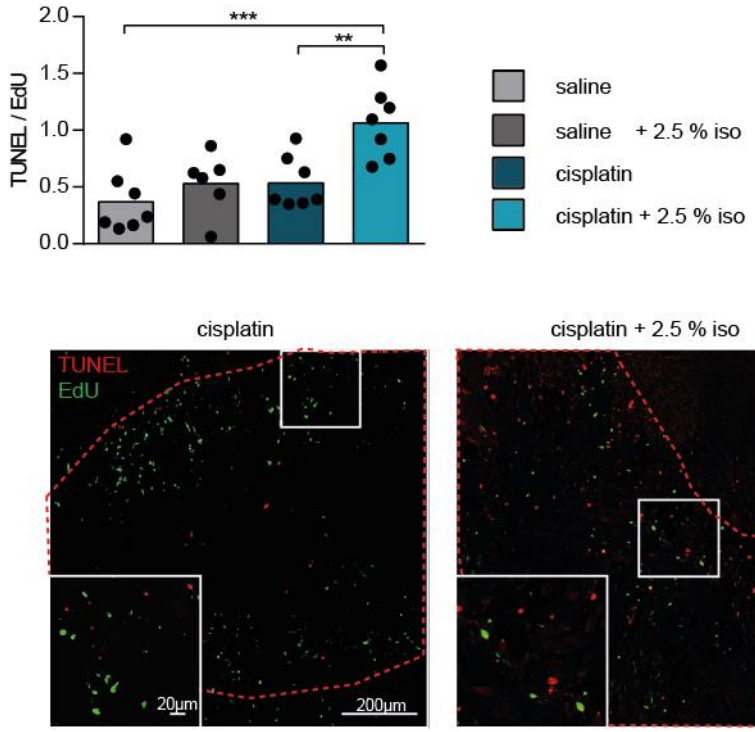

Figure 5.9l Reduced proliferation in cisplatin and isoflurane treated animals. Quantification of TUNEL and EdU positive cells in the tumor area (n= 6-7) of Gl261 implanted mice treated with cisplatin or saline with or without additional 2.5% isoflurane treatment for 30min. One-way-ANOVA with Tukey's multiple comparison test was performed between all tested cohorts. Differences were considered significant with a P-value of **, P<0.01; ***, P<0.001; Scale bar 200µm, selection 20µm.

The analysis revealed increased numbers EdU positive cells over TUNEL positive cells in both saline treated groups as well as in the cohort treated with cisplatin alone (saline: 0.38±0.11 TUNEL/EdU compared to saline/isoflurane 0.54±0.11 and

cisplatin 0.54±0.09) (Figure 5.9). These results indicate a highly proliferative phenotype for the cisplatin group as expected, since treatment is limited to the BBB comprised tumor core. Interestingly, the combined treatment of cisplatin and isoflurane showed equal numbers of apoptotic and proliferative cells (cisplatin + isoflurane 1.07±0.12 TUNEL/EdU). These results suggest enhanced cisplatin treatment within the whole tumor area, when isoflurane treatment was performed.

5.2.8 Decreased tumor cell migration in cisplatin and isoflurane treated mice

Glioblastoma multiforme is a very aggressive, rapidly growing brain tumor with intrinsic resistance to radio- and chemotherapy and therefore a poor prognosis for patients. New treatment approaches are currently under investigation with the main purpose to target tumor motility and prevent the tumor from spreading.

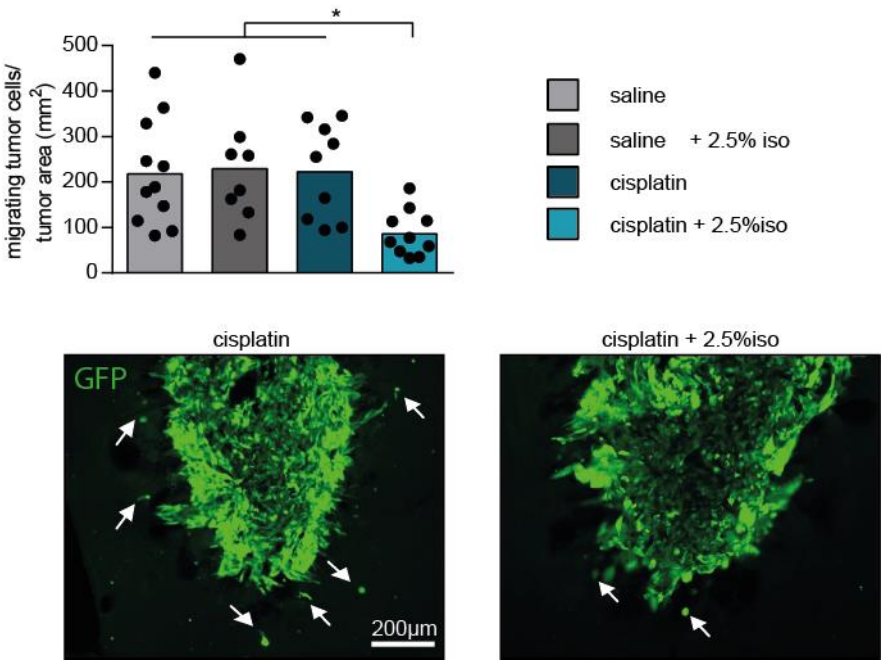

Figure 5.10l Decrease in migrating tumor cells in cisplatin + isoflurane treated mice. Quantification of GFP positive tumor cells in Gl261 implanted mice treated with cisplatin or saline with or without additional 2.5% isoflurane treatment for 30min (n= 8-11). Significance was quantified with one-way-ANOVA with Tukey's multiple comparison test. Differences were considered significant with a P-value of *, P<0.05; Scale bar 200µm.

GFP (Green fluorescent protein) expressing Gl261 cells were used to address the question, whether isoflurane can be used as a tool to attack specifically migrating tumor cells in the non-permeable brain area Therefore, additionally to the GFP

autofluorescence, GFP stainings on vibratome brain sections were performed to target all GFP expressing tumor cells. GFP positive tumor cells within the surrounding of the tumor area (50% of the tumor area) were quantified, including detached ones and cells that were still in contact with the tumor, but start to invade. The obtained data revealed that the number of migrating tumor cells in both saline cohorts and the cisplatin group showed a comparable number of GFP positive cells in the tumor surrounding (saline: 219.6±35.2 GFP+/mm^2 compared to saline/isoflurane 231.4±42.7 and cisplatin 224.4±35.12) (Figure 5.10). Notably, the combined treatment of cisplatin and isoflurane abolished tumor cell migration by about 70% (cisplatin + isoflurane 87.7±15.9 GFP+/mm^2) indicating that isoflurane serves as a suitable tool to increase the permeability of cisplatin in the tumor surrounding. With the use of isoflurane we are able to increase the treatment area of cisplatin, thereby targeting invading tumor cells and preventing these cells from spreading.

5.3 Discussion

5.3.1 Quantification of dose-dependent isoflurane BBB manipulation

Isoflurane anesthesia was shown to increase Evans blue brain entry in a dose-dependent manner (Tétrault et al., 2008). Using a new sensitive, biochemical quantification of Evans blue extravasation (Berghoff et al., 2017a), we were able to quantify the indicated dose-response and further achieve an estimation about the suitable duration for therapeutic intervention of isoflurane induced BBB manipulation. Therefore, the treatment of 30min with 2.5% isoflurane increased BBB permeability of Evans blue almost two-fold. For the first time we were able to quantify increased BBB permeability after short-term isoflurane treatment, in contrast to previous studies, which showed *in vivo* changes of BBB permeability only after three hours or more (Acharya et al., 2015; Cao et al., 2015). Furthermore, our results show that Evans blue application after the withdrawal of isoflurane revealed an extravasation level comparable to untreated controls, indicating reversible opening of BBB. These results suggest the applicability of isoflurane treatment for a temporarily confined manipulation of BBB function, with special focus on 2.5% isoflurane treatment for 30min.

5.3.2 Isoflurane mechanism of BBB modulation

To investigate the mechanism and safety of our treatment approach of 30min 2.5% isoflurane (in the following referred to as short-term treatment), we decided to compare it to 3h isoflurane treatment (referred to as long-term treatment), which was already investigated in previous studies (Acharya et al., 2015; Chai et al., 2016; Zhao et al., 2014). As expected long-term isoflurane treatment reduced the protein abundance of the tight junction proteins, occludin, claudin-5 with further indications of ZO-1 alterations. Moreover, the expression level of claudin-5 was highly increased, which might suggest a compensatory mechanism to increase tight junction abundance at the compromised BBB. In accordance with *in vitro* studies (Chai et al., 2016; Zhao et al., 2014), long-term *in vivo* isoflurane treatment induced transcriptional changes of the Hif1α signaling pathway. The expression level of *Hif1α* was downregulated, which might suggest increased Hif1α protein stability. Further,

enzymes involved in the degradation process of Hif1α (*Egln 1-3*) revealed reduced mRNA abundance. In addition, Hif1α target genes (*Vegf, Tgfβ3*) were almost two-fold upregulated, indicating increased Hif1α signaling. Moreover, increased abundance of pro-inflammatory cytokines (TNF, Il-6 and Il-1β) was associated with 2h isoflurane treatment and samples taken 6h after anesthesia (Wu et al., 2012). Furthermore, enhanced cytokine stimulation was associated with elevated levels of matrix metalloproteinases (MMP) (Qin et al., 2015). Therefore, transcriptional changes in cytokines and MMPs were investigated with the outcome of unaltered expression levels. However, western blot analysis or immunostainings might provide further insight in possible changes of cytokines and MMPs in our treated animals.

Together, the increase of Hif1α signaling after long-term isoflurane treatment is in accordance with published data (Chai et al., 2016; Zhao et al., 2014). The postulated mechanism of isoflurane BBB manipulation by Zhao and others, based on *in vitro* treated primary human brain vascular endothelial cells, comprised enhanced Hif1α stability, which triggers *Vegfα* and *Tgfβ3* expression and this affects the expression of the tight junction protein, occludin (*Ocln*) (Zhao et al., 2014). Our data are in agreement with the increase of Hif1α signaling, but the effect on occludin expression was not detectable. Instead, our results of *in vivo* long-term isoflurane treatment demonstrated decreased occludin and claudin-5 protein abundance and further increased claudin-5 expression.

Since long-term isoflurane treatment has been investigated previously, we focused on the short-term treatment. For the first time, we showed BBB manipulation by isoflurane treatment already after 30 min. Therefore, we wanted to investigate whether the mechanism of BBB opening might be comparable to long-term treatment. Short-term isoflurane treatment revealed decreased abundance of tight junction proteins occludin and claudin-5. Changes in expression levels were not detected for tight junction proteins. Furthermore, short-term isoflurane treatment in contrast to long-term treatment showed unaltered expression levels of Hif1α signaling components. The induced BBB manipulation of short-term isoflurane treatment was further independent of expression of pro-inflammatory cytokines and MMPs. In summary, these results suggest a different mechanism of BBB manipulation for the short-term isoflurane treatment compared to long-term treatment. Furthermore, one possible mechanism of short-term isoflurane treatment might be the internalization of tight junction proteins.

5.3.2.1 Short-term BBB manipulation by isoflurane functions via TJ internalization?

The complex structure of tight junction proteins at the intercellular cleft allows highly dynamic adaptation to various extracellular stimuli. To date two mechanisms of tight junction remodeling are postulated, which include diffusion and endocytosis (Stamatovic et al., 2017). Highly dynamic diffusion of the tight junction proteins occludin and ZO-1 was shown by FRAP and FLIP experiments with the use of an epithelial cell line (Fluorescence recovery after photobleaching and Fluorescence loss in photobleaching) (Shen et al., 2008). Since protein abundance of occludin and claudin-5 was highly diminished after isoflurane treatment, internalization of tight junction proteins most likely functions via another mechanism e.g. endocytosis.

The endocytosis of tight junction proteins is a well characterized mechanism in health and disease (Stamatovic et al., 2017). In fact, it has been shown that occludin is internalized via caveolin-1-dependent mechanism upon TNFα signaling (Marchiando et al., 2010). Furthermore, the chemokine CCL2 was able to induce internalization of occludin and claudin-5 mediated via lipid raft/caveolin-1 endocytosis (Stamatovic et al., 2009). Additionally, internalized tight junction proteins were found in early and recycling endosomes until they were re-shuttled to the cell membrane.

Occludin as well as claudin-5 were highly prone to phosphorylation by Rho kinase (Yamamoto et al., 2008). Moreover, only highly phosphorylated occludin was found to build up tight junction structures, whereas non- or less phosphorylated occludin localized at the basolateral membrane and in cytoplasmic vesicles (Sakakibara et al., 1997). Furthermore, occludin phosphorylation by different isoforms of protein kinase C (PKC) was shown to be important for the binding to the adaptor protein ZO-1 (Rao, 2009). Moreover, volatile anesthetic agents like isoflurane and sevoflurane were shown to be involved in Rho kinase function (Hanazaki et al., 2008; Kim et al., 2014; Yang et al., 2016) and PKC activity (Turner et al., 2005; Zhong et al., 2002). In fact, isoflurane functions via the PI3 kinase pathway to inhibit Rho kinase phosphorylation of myosin light chain kinase in rat bronchial smooth muscles (Yang et al., 2016).

Therefore, one hypothesis of isoflurane function of tight junction internalization might be that kinase activity (e.g. Rho kinase) is inhibited by isoflurane, which leads to insufficient phosphorylation of tight junction proteins (Figure 5.11).

In more detail, isoflurane anesthesia leads to the rapid exposure of isoflurane to endothelial cells. Isoflurane might induce alterations of Rho kinase activity, which leads to modifications of the phosphorylation status of tight junction proteins e.g. occludin and claudin-5. At least for occludin it has been shown that changes in the phosphorylation state are detrimental for tight junction localization (Sakakibara et al., 1997). Occludin, claudin-5 and ZO-1 are able to be internalized either by caveolae or clathrin-induced vesicle endocytosis (Stamatovic et al., 2017). Furthermore, internalized occludin and claudin-5 are stored in endosomes and are able to be recycled back to the plasma membrane upon so far unknown stimuli (Stamatovic et al., 2009). This predicted mechanism might be suitable to explain our temporarily confined BBB manipulation by short-term isoflurane treatment. Nevertheless, direct evidence of the involvement of Rho kinase activity needs to be elucidated in the near future. Therefore, analysis of the phosphorylation state of occludin and claudin-5 as well as analysis of Rho kinase abundance and activity needs to be performed.

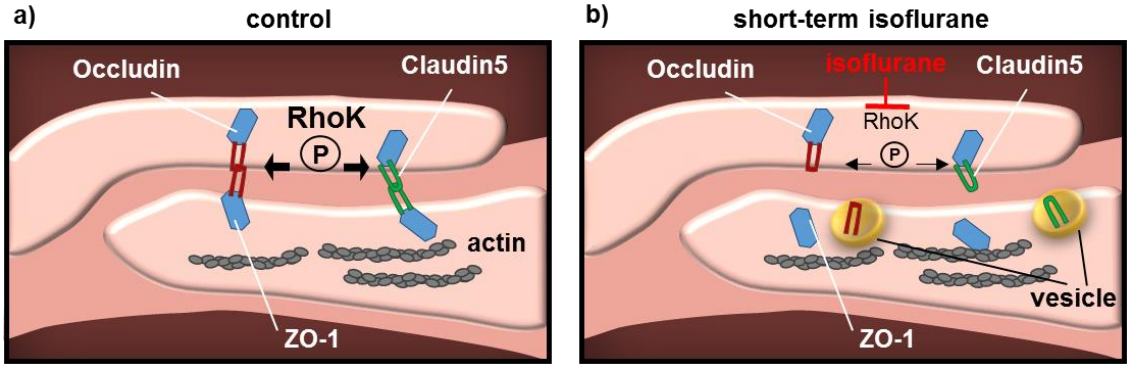

Figure 5.11I Theoretical mechanism of isoflurane-induced tight junction internalization. a) In endothelial cells the tight junction proteins occludin and claudin-5 are linked to the actin cytoskeleton via adaptor molecules such as ZO-1. Kinases such as RhoK phosphorylate tight junction proteins, which serves as a prerequisite for their localization in the intercellular cleft. **b)** Short-term isoflurane treatment might inhibit Rho kinase activity, thereby probably inducing the internalization of occludin and claudin-5 via caveolae or clathrin-coated vesicles. Further ZO-1 redistribution might be possible.

5.3.3 Benefit of isoflurane-induced BBB manipulation for glioblastoma treatment

The present work summarizes the investigation of isoflurane anesthesia as a tool to modulate BBB permeability and further to enhance drug delivery in a glioblastoma mouse model. Previously, it has been reported that the tumor core formed by transplanted cell lines in mice was permeable for Evans blue entry (Leten et al.,

2014). In our Gl261 implanted mice, we showed that short-term isoflurane treatment increased Evans blue entry from the tumor core into the whole brain tissue. Furthermore, Evans blue application after isoflurane withdrawal revealed unaltered BBB permeability. These findings suggested that short-term isoflurane treatment serves as a suitable tool to enhance the delivery of chemotherapeutic agent in a temporarily confined manner into the brain tissue of tumor implanted mice.

In a first therapeutic approach we treated glioblastoma implanted mice with a combined treatment of short-term isoflurane anesthesia after intravenous injection of the non-permeable cytostatic agent cisplatin. The results after 14 days revealed, decreased tumor volume, increased T-cell numbers in the tumor surrounding and reduced tumor cell viability. The most remarkable finding was the reduction of migrating tumor cells and therefore the decreased potential of tumor cells to spread into healthy brain tissue.

Already several decades ago, mechanisms to manipulate BBB function have been investigated including osmotic disruption and the neurovascular mediator bradykinin (Matsukado et al., 1996; Siegal et al., 2000). These early attempts developed several disadvantages such as the invasive and long-lasting disruption of the BBB, which induced several undesired side effects. In recent years, several systems to manipulate BBB function by a non-invasive method were under investigation with highly improved outcome. These systems include synthetically modified E-cadherin peptide (On et al., 2017, 2014), application of a focused ultrasound (Liu et al., 2014; Wei et al., 2013), NMDA activation via high-intensity magnetic stimulation (Vazana et al., 2016) and the development of highly specific nanoparticles (Lee, 2017) (see chapter 5.1.1.5).

The use of isoflurane anesthesia for the manipulation of BBB function in a defined period to increase the entry of chemotherapeutic agents into brain tissue of glioblastoma patients provides a promising perspective for future clinical trials. One major advantage of isoflurane anesthesia is that our used set-up of 2.5% isoflurane is considered a clinically relevant concentration (Zhao et al., 2013) and clinical application has already been approved. Moreover, the application of isoflurane for the duration of 30min seems to be safe and BBB manipulation most likely reversible. Chemotherapy for glioblastoma patients can be applied via intravenous infusions in combination with short-term isoflurane anesthesia under medical supervision with only minor inconvenience for patients compared to other treatment approaches.

6 Material

The used laboratory expendable material and equipment, if not mentioned differently, was provided by BD Falcon (Heidelberg, Germany), Bio-rad (München, Germany) Gilson (Limburg-Offheim, Germany), Eppendorf (Hamburg, Germany), Sartorius (Göttingen, Germany) and Greiner Bio-One (Frickenhausen, Germany).

6.1 Equipment

Treatment

Freestyle Precision System	Abbott Diabetes Care
Mouse restrainer	In-house made

Molecular Biology

7500 Fast Real-Time PCR System	Applied Biosystems
PowerPac 300 Power Supply	Bio-Rad
SDS-PAGE gel casting and running units	Bio-Rad
Eon Microplate Spectrophotometer	BioTek
Table-top ThermoMixer	Eppendorf
Table-top Centrifuge	Heraeus Sepatech
INTAS ChemoCam Imager ECL HR-16-3200	Intas
INTAS UV-system with Camera and printer	Intas
PCR-machine	PeqLab
NanoDrop200 Spectrophotometer	Thermo Scientific
Homogenizer Ultra Turrax T8	Kinematica
Lyophilization LMC-1 BETA 1-16	Christ

Tissue Culture

Clean bench	Heraeus
Cooling centrifuge Optima TLX	Beckmann
Incubator	Heraeus

Tissue Preparation

Student vannas spring scissor	Fine Science Tools
Fine iris scissor	Fine Science Tools

Standard scissor	Fine Science Tools
Dumont forceps	Fine Science Tools
Scalpel blades (#21)	Fine Science Tools
Scalpel handel	Fine Science Tools
Peristaltic Pump PD 5101	Heidolph

Surgery

Isoflurane anesthesia station Isotek5	Groppler
Animal temperature control ATC1000	WPI World Precision Instruments
Microscope M76	Leica
OP lamp KL1500 compact	Schott
Omni Drill 35	WPI World Precision Instruments
Injection needle 5A-FN-GP 5µl	S.G.E. Analytic Science
Scissor (11-755-11-07)	KLS MARTIN
Ball Mill, Carbide 501853	WPI World Precision Instruments
1x Histoacryl (tissue glue)	Braun
Stereotactic Instrument	Kopf

Histology

Microwave	Daewoo
Leica Jung Cryocut CM3000	Leica
Embedding station HMP110	Microm
Paraffin embedding center	Microm
Sliding microtome HM400	Microm
Sequenza™ Immunostaining Center System	Thermo Scientific

Electron microscopy

Semi 35° diamond knife	Diatome
Ultra 45º diamond knife	Diatome
Heatplate	Leica
Ultracut S	Leica

EM Trimm (Trimming device)	Leica

Microscopes

Axio Observer. Z1	Zeiss
Axiophot	Zeiss
LEO EM 912AB electron microscope	Zeiss
Leica TCS SP5	Leica

Behavior

Elevated beam test	In-house made
Rotarod	In-house made

Software

Adobe Illustrator CS5
ImageJ
Fiji
GraphPad Prism 5
Microsoft Excel 2013
Zen 2012 Zeiss
LSM software (Confocal images acquisition)
Mendeley (Reference manager)
Amira Software, Visage Imaging (MRI quantification)

6.2 Expendable Materials

All expendable material, if not mentioned differently, were purchased from Falcon (Becton Dickinson, Le Pont De Claix, France) and Eppendorf (Eppendorf, Hamburg, Germany). Culture flasks were obtained from Greiner Bio-One (Greiner Bio-One, Frickenhausen, Germany).

Glucose test strips	Abbott Diabetes Care
Ketone test strips	Abbott Diabetes Care
Micro haematocrit capillary	Brand

pH reagent strips	Macherey-Nagel
Syringe 1 ml	BD Bioscience
Venofix® 0.4 x 10 mm	Braun
Cover glass	Assistant
HistoBond® slides	Marienfeld
Tissue cassettes	Polyscience Inc.
Copper grids	Science Services
PVDF-Membran Hybond-PTM	Amersham
Aqua-Poly/Mount	Polysciences
Eukitt	Kindler
Tissue-Tek® O.C.T. Compound	VWR
Skimmed milk powder	Frema
Eye ointment	Bepanthen
Formamide	Sigma
50ml Falcon filter	BD Bioscience
21-gauge cannula	BD Bioscience
23-gauge cannula	BD Bioscience
Cell culture flask	Greiner Bio-One

6.3 Chemicals

All chemical, if not mentioned otherwise, are purchased from Merck KGaA (Darmstadt, Germany), Roche Diagnostics GmbH (Mannheim, Germany), Serva (Heidelberg, Germany) and Sigma-Aldrich GmbH (Munich, Germany).

Isoflurane CP®	CP-Pharma
Cis-Platin (cis-Diamineplatinum(II)dichloride)	Sigma-Aldrich Chemie GmbH
Xylariem	Ecuphar
Carprieve (Carprofen)	Norbrook (Bayer)
Goatserum	Invitrogen
Ketamin	Medistar

Cell culture

Dulbeco's Modified Eagle's Medium (DMEM)	Gibco/ Invitrogen
HBSS (Hanks balanced salt solution)	Lonza
Glucose	Sigma-Aldrich Chemie GmbH
Poly-L-lysine	Sigma-Aldrich Chemie GmbH
Insulin	Sigma-Aldrich Chemie GmbH
Horse serum	Sigma-Aldrich Chemie GmbH
EGTA (Ethylene-bis(oxyethylenenitrilo)tetraacetic acid)	Sigma-Aldrich Chemie GmbH
Penicillin/streptomycin	Lonza
GlutaMax™	Gibco/ Invitrogen
Bovine serum albumin (BSA)	Biomol GmbH

6.4 Enzymes

GoTaqTM DNS-Polymerase	Promega
Proteinase K (10mg/ml)	Boehringer
PhOSstop EASYstep phosphatase inhibitor	Roche Diagnostics GmbH
Complete Mini protease inhibitor	Roche Diagnostics GmbH
DNase	Roche Diagnostics GmbH
Papain	Worthington Biochemical Corp.
Trypsin	Invitrogen
Nucleotide (dATP, dCTP, dGTP, dTTP)	Boehringer

6.5 Kits

DAB Zytomed Kit	Zytomed Systems GmbH
DC Protein Assay (Lowry)	Bio-Rad
LSAB2 kit	Dako
Vector Elite ABC Kit	Vector Labs
RNeasy Mini kit DNase	Qiagen
NucleoSpin®Tissue Kit	Macherey-Nagel

Western Lightning™ Plus-ECL	Perkin Elmer Life Sciences, Inc.
Superscript IIITM Kit	Invitrogen
Click-it™EdU Alexa Fluor™555 Imaging kit	Thermo Fischer Scientific
DeadEnd™ Colorimetric TUNEL System	Promega Corporation
WST-1 cell proliferation assay kit	Cayman chemical

6.6 Antibodies

Primary antibodies

LAMP1	1:200 IHC	BD Biosciences 553792
GFAP	1:200 IHC	Novocastra NCL-GFAP-GA5
MAC-3	1:400 IHC	Pharmigen 01781D
GFP	1:500 IHC	Rockland
APP	1:1000 IHC	Chemicon
CaII	1:200 IHC	kindly provided by S. Ghandour PMID: 118210
Olig2	1:100 IHC	kindly provided by J. Alberta, PMID: 15198128
CD3	1:50 IHC	Serotec MCA1477
Isolectin IB4	1:50 IHC	Vector Lab
Occludin	1:10 IHC	Invitrogen 47-4400
Claudin5	1:10 IHC	Invitrogen #35-2500
ZO-1	1:10 IHC	Invitrogen #61-7300
Plp1	1:100 IHC	Jung et al., 1996
TUNEL	Kit	Promega
EdU	Kit	Thermo Fischer Scientific

NG2 (AN2)	1:100 IHC	kindly provided by J. Trotter, Mainz
ATF6	1:500 WB	Abcam #40256
Oxct1	1:1000 WB	Proteintech Europe #12175-1AP
Actin	1:2500 WB	Sigma #A3853

Secondary antibodies

α-rabbit-HRP	1:5000 WB	Dianova
α-mouse-HRP	1:5000 WB	Dianova
α-mouse-Alexa488	1:1000	ThermoScientific A-21202
α-mouse-Alexa555	1:1000	ThermoScientific A-31570
α-rabbit-Alexa488	1:1000	ThermoScientific A-21206
α-rabbit-Alexa555	1:1000	ThermoScientific A-31572
α-rat-Alexa488	1:1000	ThermoScientific A-21208

6.7 Buffers and Solutions

Fixation

Avertin

2% [w/v] 2,2,2 Tribromethanol 99%

2% [v/v] Amylalkohol

Mixed at 40°C for 30 min, filtered and stored at -20°C

16% [w/v] Paraformaldehye (PFA) stock solution

16% [w/v] Paraformaldehyde cooked at 65°C for 15 min while stirring

Add 5N NaOH until solution turns clear, filter and store at -20C°.

0.2M Phosphate buffer (fixation buffer)

0.36% [w/v] Sodiumdihydrogenphosphate (NaH_2PO_4)

3.1% [w/v] di-Sodiumhydrogenphosphate (Na_2HPO_4)

1% [w/v] Sodium chloride

4% [v/v] Paraformaldehye (PFA) for immunohistochemistry

4% [v/v] PFA

0.1 M Phosphate buffer

Karlsson-Schultz (K+S) fixative for electron microscopy

4% [w/v] PFA

2.5% [v/v] Glutaraldehyde

0.1 M Phosphate buffer

Molecular biology

10 mM dNTP (50x stock)

2.5 mM each nucleotide (dATP, dCTP, dGTP, dTTP) (Boehringer-Ingelheim)

200 µM final concentration in a PCR reaction (50 µM each nucleotide)

TBE 20x (stock solution)

1.8 M TrisBase

1.8 M Boric acid

200 mM EDTA

2 % agarose gel

3.5 g agarose

350 ml 1 x TBE buffer

Protein biochemistry

Protein lysis buffer

1x TBS

0.1% [v/v] SDS

0.1% [v/v] Triton X-100

Complete Mini protease inhibitor (Roche Diagnostics GmbH) and PhOSstop EASYstep phosphatase inhibitor (Roche Diagnostics GmbH) tablets were freshly added to the protein lysis buffer (1 tablet/10ml) before use.

SDS separating gel (1.5 mm thickness)

10% [v/v] Acrylamide / Bisacrylamide 29: 1

0.4 M Tris-HCl pH 8.8

0.1% [w/v] SDS

0.03% [v/v] Ammonium persulfate

0.08% [v/v] TEMED

SDS stacking gel (1.5 mm thickness)

4% [v/v] Acrylamide / Bisacrylamide 29: 1

125 mM Tris-HCl pH 6.8

0.1% [w/v] SDS

0.05% [w/v] Ammonium persulfate

0.1% [v/v] TEMED

4x SDS sample buffer

40% [v/v] Glycerol

240 mM Tris/HCl pH 6.8

8% [v/v] SDS

0.04% [w/v] Bromophenol blue

10x SDS running buffer (Laemmli buffer)

250 mM Tris base

1.92 M Glycine

1% [v/v] SDS

Transfer buffer

96 mM Tris base

78 mM Glycine

20% [v/v] Methanol

10x Tris-buffered saline (TBS)

500 mM Tris/HCl, pH 7.5

1.5 M NaCl

1x TBS with Tween-20 (TBST)

50 mM Tris/HCl, pH 7.5

150 mM NaCl

0.05% [v/v] Tween-20

Immunoblot blocking buffer

5% [w/v] non-fat dry milk powder in 1x TBST

Immunohistochemistry

10x Phosphate buffered saline (PBS)

1.7 M NaCl

0.04 M KCl

0.04 M Na_2HPO_4

0.018 M KH_2PO_4

Adjusted to pH 7.2 with 1 M NaOH.

0.01 M Citrate buffer (pH 6.0)

1.8 mM Citric acid

8.2 mM Sodium citrate

Prepared freshly before use.

BSA/PBS

0.04 M NaH_2PO_4

0.16 M Na_2HPO_4

1.8% [w/v] NaCl

1.0% [w/v] Bovine serum albumin (BSA)

Tris buffer (pH 7.6)

50 mM Tris/HCl, pH 7.6

0.9% [w/v] NaCl

Prepared freshly before usage.

Mayer's haematoxylin solution

0.1% [w/v] Haematoxylin

0.02% [w/v] $NaIO_3$

5% [w/v] $K_2Al_2(SO_4)_4 \cdot 24H_2O$

Added under constant shaking.

5% [w/v] Chloral hydrate

0.1% [w/v] Citric acid added

Always filter freshly before usage.

Scott's solution

0.2% [v/v] $KHCO_3$

2% [w/v] $MgSO_4$

HCl - alcohol

0.09% [v/v] HCl

70% [v/v] Ethanol

Electron microscopy

Epon

171.3 g Glycidether 100

115 g DDSA (Dodecenyl succinic anhydride)

89 g MNA (Methyl nadic anhydride)

Mixed for 10 min.

6.5 ml DMP-30

Added and mixed for another 20 min.

Methylene blue/ azure II

1% Na-tetraborat (Borax)

1% Methylen blue

1% Azure II

Azure II and Methylene blue were freshly mixed 1:1 before use.

Formvar solution

1.25% [w/v] Formvar

50 ml Chloroform

Mixed for 30 min. Store protected from light at RT.

Tissue culture

Cultivation Media (Glioblastoma GL261-GFP)

DMEM (4,5 g/l glucose, pyruvate)

+ 10% FCS

+ 1% GlutaMAX

+ 1% Penicillin/Streptomycin

6.8 Marker, dyes and tracer

GeneRuler 100 bp DNA ladder	Thermo Fisher Scientific
PageRuler™ Plus Prestained Protein Ladder	Thermo Fisher Scientific
DAPI (4,6-diamidino-2-phenylindol)	Roche Diagnostics GmbH
Evans blue	Sigma-Aldrich Chemie GmbH

6.9 Oligonucleotides

Hprt1	for:	TCCTCCTCAGACCGCTTTT
	rev:	CCTGGTTCATCATCGCTAATC
Rplp0	for:	GATGCCCAGGGAAGACAG
	rev:	ACAATGAAGCATTTTGGATAATCA
Rps13	for:	CGAAAGCACCTTGAGAGGAA
	rev:	TTCCAATTAGGTGGGAGCAC
Plp1	for:	TCAGTCTATTGCCTTCCCTAGC
	rev:	AGCATTCCATGGGAGAACAC
Olig2	for:	AGACCGAGCCAACACCAG
	rev:	AAGCTCTCGAATGATCCTTCTTT
Gfap	for:	TGCTCCTGCTTCGAGTCCTT
	rev:	CAAGAGGAACATCGTGGTAAAGA
Aif-1 (Iba-1)	for:	TGTTTTTCTCCTCATACATCAGAATC
	rev:	CCGAGGAGACGTTCAGCTAC
Hmgcs2	for:	CTGTGGCAATGCTGATCG
	rev:	CCATGTGAGTTCCCCTCA
Fasn	for:	GTCCACCCCAAGCAGGCACA
	rev:	ACTCACACCCACCCAGACGC
Slc16a1 (MCT1)	for:	ATGCTGCCCTGTCCTCCT
	rev:	CCACAAGCCCAGTACGTGTAT
Slc16a7 (MCT2)	for:	TCGTGGAGTGTTGTCCAGTT
	rev:	TCCAGTTATATCAAGCAATTTACCA
Acat1	for:	AGGGAAGTTTGCCAGTGAGA
	rev:	TTCACCACCACATCTGGTTTAC
Bdh1	for:	GAGCTACGGGTTCAGACGAG

	rev:	TGGCACCAAGTTGTAAGACG
Oxct1	for:	GGCCAACTGGATGATACCTG
	rev:	GGAACTGGACACCAAATCCA
Atf6	for:	GACAGCTCTTCGCTTTGGAC
	rev:	GGACGAGGTGGTGTCAGAG
Atf4	for:	ATGATGGCTTGGCCAGTG
	rev:	TCTCCAACATCCAATCTGTCC
Xbp1	for:	AGGAGTTAAGAACACGCTTGGG
	rev:	GGTCCAACTTGTCCAGAATGC
Hspa5 (BIP)	for:	CTGAGGCGTATTTGGGAAAG
	rev:	CAGCATCTTTGGTTGCTTGTC
Ddit-3 (Chop)	for:	GCGACAGAGCCAGAATAACA
	rev:	GATGCACTTCCTTCTGGAACA
Ocln	for	TCCGTGAGGCCTTTTGAA
	rev	GGTGCATAATGAATTGGGTTTG
Cldn5	for	ACGGGAGGAGCGCTTTAC
	rev	GTTGGCGAACCAGCAGAG
Zo1	for	ATGCAGACCCAGCAAAGGT
	rev	TGACCAAGAGCTGGTTGTTTT
Npc1	for	CCTTCGGGCCTCCATTG
	rev	TGTCACGGTTTCATTGTTGTAAGA
Npc2	for	CCGGTGAAGAATGAATACCC
	rev	TTCTTTTTGTCATCTTCAAGTTTCC
Mmp9	for	GGTCGCTCGGATGGTTATC
	rev	AGTTGCCCCCAGTTACAGTG
Mmp2	for	GTGGGACAAGAACCAGATCAC
	rev	GCATCATCCACGGTTTCAG
Il6	for	TCCATCTATTTGCCTAAGAATTTCA
	rev	TGTAGGGGAATGTCAGAGTGG
Tnfα	for	CATCTTCTCAAAATTCGAGTGACAA
	rev	TGGGAGTAGACAAGGTACAACCC
Egln2	for	GGAACCCACATGAGGTGAA
	rev	AACACCTTTCTGTCCCGATG
Egln1	for	CTGTGGAACAGCCCTTTTTG
	rev	CGAGTCTCTCTGCGAATCCT

Egln3	for	TGTCTGGTACTTCGATGCTGA
	rev	GCAAGAGCAGATTCAGTTTTTCT
Hif1α	for	GAGCACTAGTTGATCTTTCCGAGG
	rev	TCTCTCTAGACCCATAACGCCGC
Vegfα	for	AAAAACGAAAGCGCAAGAAA
	rev	TTTCTCCGCTCTGAACAAGG
Tgfβ3	for	CATGATGATTCCCCCACAC
	rev	GCAGTTCTCCTCCAAGTTGC
Hexa	for	ACCTGGGAGGGGATGAAGT
	rev	ATGAAGGCCTGGATGTTGG
Man2b1	for	CTGATCCGCCTGGTCAAC
	rev	AGGTAACACGTAGGGGTGGA
Hmgcr	for	TGATTGGAGTTGGCACCAT
	rev	TGGCCAACACTGACATGC
Fdft1	for	TCAATCAGACCAGTCGCAGC
	rev	GTGCCGTATGTCCCCATTCC
Mbp	for	CCAGCTTAAAGATTTTGGAAAG
	rev	GACTCACACACGAGAACTACCC
Mog	for	ATTTCCCATTGGCCTCTTTGCTGTGGAC
	rev	CTCAAGGTCCTCCCACCAGGCT
Cspg4	for	CACCTCCAGGTGGTTCTCC
	rev	CTTGGCCTTGTTGGTCAGAT
Car2	for	CAAGCACAACGGACCAGA
	rev	ATGAGCAGAGGCTGTAGG

6.10 Cells

GL261 mouse glioma cells expressing green fluorescent protein (GPF) were kindly provided by Dr. Petra Hülper.

7 Methods

7.1 Animals

All animal experiments were performed in compliance with the animal policies of the Max Planck Institute of Experimental Medicine, and were approved by the German Federal State of Lower Saxony.
In this study, we used C57BL/6N wildtype and Plp1 overexpressing transgenic mice, line 72 (PLP-tg$^{72/72}$; Readhead et al., 1994). Mice were bred and kept in individually ventilated cages with a 12-hour day/night cycle. Mice were sacrificed by cervical dislocation or by perfusion after deep anesthesia with Avertin. Only male mice were used in both studies.

7.1.1 Treatment

PLP-tg$^{72/72}$ mice were fed ad libitum a standard pellet chow (ssniff V1124) with or w/o supplemented cholesterol (5%), a medium chain fatty acid chow (ssniff MCT, modified Surwit) or a ketogenic chow (KD, ssniff E15249-30). Duration of feeding diets as indicated.
For the classical ketogenic diet a specialized rearing device was applied (developed by Tim Düking). Maternal milk production is highly impaired in response to high fat diets (Sussman et al., 2013). Therefore, a plateau and a box with a small hole were installed to separate the chow of the pups and damns. At around P15, the pups started to enter the installed box in which the ketogenic or standard chow was provided. In contrast, the medium chain fatty acid diet contained a sufficient level of carbohydrates (compared to KD), which are preferentially used to cover high energy expenditure during lactogenesis (Butte, 1999). Therefore, the standard cage set-up was used. Weight of the mice was monitored every week until twelve weeks of age starting with two weeks. Blood for glucose and β-hydroxybutyrate measurements were taken from mice tail tip weekly using the Freestyle Precision System with the corresponding glucose and ketone test strips (Abbott Diabetes Care). Endpoint serum pH was analyzed with reagent strips (Macherey-Nagel, Düren, Germany). Serum was obtained by collecting blood with a capillary tube (Micro haematocrit

capillary, Brand, Wertheim, Germany) from the eye vein. Samples were incubated at RT for 2h, centrifuged at 5.000rpm for 10min.

7.2 Glioblastoma

7.2.1 Surgery

Eight weeks old male C57BL/6N mice were anesthetized with an intraperitoneally injection of ketamine/xylazine 85 mg per kg body weight/ and 7 mg per kg body weight respectively. The head of the mice was shaved and a small hole was drilled 2mm lateral, 1mm anterior and 3 mm deep in the right hemisphere of mice. The mice were transferred into a stereotactic instrument (Kopf) and 5 µl PBS containing $7.5x10^4$ GL/261-GFP cells were injected. The wound was cleaned, sealed with tissue glue (Histoacryl) and 2-4mg/kg of the analgetic carprofen was injected subcutaneously. Respiration and body temperature was constantly monitored until the mice woke up and recovered from anesthesia. Mice were housed in individually ventilated single cages with a 12-hour day/night cycle. After two weeks mice were sacrificed by perfusion after deep anesthesia with Avertin.

7.2.2 Treatment

Mice were divided in four groups: cisplatin, cisplatin + isoflurane, saline and saline + isoflurane. At day eight and eleven after implantation mice were treated according to their group with 3mg/kg cisplatin (solution: 0.5mg/ml cisplatin in saline 0.9% NaCl) or equal amount of saline. Afterwards they were directly put into the isoflurane evaporator chamber (Isotek5, Groppler) preflushed with 4% of the volatile anesthetic isoflurane for 2min and then decreased for another 28min to 2% isoflurane at a flow rate of 0.7l/min. Body temperature and respiration was controlled (Animal temperature control ATC1000) during anesthesia and the mice were allowed to wake with 100% O_2 for 2min at the end of isoflurane treatment. Due to nephrotoxic side effects of the cisplatin treatment mice got an i.p injection of 300µl saline before and after the treatment, and after 24h. A single i.p. injection of EdU was applied 16h before the mice were sacrificed. On day 14 after implantation mice were sacrificed by perfusion after deep anesthesia with avertin.

7.3 Molecular biology

7.3.1 Genotyping

Tail or Ear biopsies were taken from PLP-tg$^{72/72}$ mice and digested using the NucleoSpin®Tissue Kit (Macherey-Nagel) according to manufacturer's instructions. The concentration of the DNA samples were measured with the NanoDrop200 Spectraphotometer (Thermo Scientific) and adjusted to 100ng per animal per PCR.

Plp-$^{tg72/72}$

Reaction approach:

3-10 µl DNA (100ng)
0.5 µl Primer (1751 NGII Primer)
0.5 µl Primer (1750 NGII Primer)
0.5 µl Primer (19398)
0.5 µl Primer (19399)
2 µl dNTP's (2 mM)
5 µl Go-Taq buffer (5x)
0.1 µl Go-Taq

Reaction batch was filled with ddH_2O to a total volume of 20 µl and the PCR (Peqlab) reaction was started using the following program:

PCR program:

(1)	95°C 3 min	
(2)	56°C 30 sec	
(3)	72°C 40 sec	19x
(4)	95°C 1 min	
(5)	56°C 1 min	
(6)	72°C 5 min	

DNA fragments were visualized with the use of 5 µl GelRed (1:40.000) added to each PCR reaction. Samples were loaded on a 2% agarose gel and gel electrophoresis was done in a running chamber with 1x TBE buffer for 60-100 min at 120 V. GeneRuler 100 bp DNA ladder (Thermo Scientific) was used as a size marker. For detection the INTAS UV-system with Camera and printer (Intas) was used. Homozygote and heterozygote Plp-tg mice were distinguished by comparing the transgene band to NGII control bands.

7.4 Gene expression analysis

7.4.1 RNA purification

RNA purification from brain tissue was done using the RNeasy kit (Qiagen) following manufacturer´s instructions. RNA quality and quantity was determined either on NanoDrop200 Spectraphotometer (Thermo Scientific) or Agilent 2100 Bioanalyzer (Agilent Technologies).

7.4.2 Complementary DNA (cDNA) synthesis

Reverse transcription (RT) was done using the SuperScript III (Thermo Fisher Scientific).

First RNA was premixed with two different primer:
4 µl RNA (0.4-1 µg)
1 µl dT mix Primer (0.6 pmol/µl)
1 µl N9 (random nonamers 120 pmol/µl)

Then samples were incubated at 70°C for 2 minutes, put on ice and the following mix was added to the reaction:

2 µl 5x first strand buffer
0.5 µl dNTP (10 mM)
1 µl DTT (100 mM)
1 µl SuperScript III reverse transcriptase (200 U/µl)

The reaction mix of 10.5 µl was centrifuged and the following PCR program was used:

(1) 25ºC 10 min
(2) 50ºC 45 min
(3) 55ºC 45 min

Synthesized cDNA was diluted with ddH_2O to a final concentration of 0.5 ng/µl.

7.4.3 Quantitative real-time PCR (qRT-PCR)

Quantitative RT-PCRs were performed in triplicates with the GoTaq master mix (Promega) on the Roche LC480 Detection System (Applied Biosystems). Expression values were normalized to the geometric mean of the housekeeping genes, Hprt (Hypoxanthin-Phosphoribosyl-Transferase 1), Rplp0 (60S acidic ribosomal protein P), Rps13 (Ribosomal *Protein S13)* and analyzed by the ΔΔCt method. Obtained data of RT-PCR is calculated as the relative expression to controls.

7.5 Protein biochemistry

7.5.1 Sample preparation

Mice were sacrificed by cervical dislocation and spinal cord samples were snap frozen in liquid nitrogen. Frozen spinal cord tissue was homogenized in 600µl sucrose buffer with the Ultraturrax (T8, Ika, Staufen, Germany) at highest settings for 20-40 s. Lysates were centrifuged for 5min at 13.000 rpm to remove nuclei and the supernatants were used for protein biochemistry.

7.5.2 Protein assay

According to the Lowry method for the measurement of protein concentrations (LOWRY et al., 1951) the Bio-Rad DC Protein Assay kit was used following manufacturer´s instructions. BSA standards with defined protein concentrations (0-

4µg/µl) were used to evaluate sample concentration. An Eon microplate spectrophotometer (BioTek) detected the absorbance at 650 nm and calculated the concentration according to standards.

7.5.3 Protein separation using SDS-PAGE

For the protein separation SDS-polyacrylamide gels with concentration of 12 % (MOPS Bis-Tris) and 1.5 mm thickness were used with the Bio-rad system. Samples were diluted in 2x SDS sample buffer and 5% 2-Mercaptoethanol or DTT was added for reducing conditions. Protein lysates were denaturated on a shaker for 10 min at 40°C or 70° corresponding to the used antibody. In addition 5 µl of the marker (PageRuler™ Plus Prestained Protein Ladder) was loaded on the gel. According to manufacturer's protokoll, the chamber of the Mini-PROTEAN® electrophoresis system (BIO-RAD) was filled with 1x SDS running buffer and the gel was run at 70 V and 50 mA for approximately 10 min. Then voltage was adjusted to 120 V and 25 mA/per gel at RT for 1-2 h to separate proteins according to their size.

7.5.4 Western blotting

The semi-dry chamber (Invitrogen) was used for protein transfer. The PVDF membrane (polyvinylidene difluoride membrane (Hybond P, Biosciences, pore size 0.45 µm)) was first activated for 1 min in 100% methanol. After washing two times with ddH_2O the membrane was put in transfer buffer. The transfer system was assembled with three Whatman papers, activated PVDF membrane, protein gel followed by three more Whatman papers all pre-incubated in transfer buffer. Proteins were transferred at 20 V for 40 min.

After blotting, the membrane was blocked with 5% milk powder in TBS-T (0.05% Tween-20 in TBS) at RT for 1 h. Membranes were incubated with primary antibodies (see chapter 6.6) in blocking solution on a rotor at 4°C overnight. On the next day membranes were washed three times for 10 min in TBS-T and detection with HRP-conjugated secondary antibodies (1:5000 diluted in blocking solution) was done at RT on a rotor for 1h. Membranes were washed three times in TBS-T. TBS-T was removed from the membrane and 1 ml of Western-Lighting Plus-ECL Reagent (PerkinElmer) was applied for 1 min for chemiluminescence detection of protein

bands with the Intas ChemoCam Imager for 1-15min. Obtained signals were normalized to loading controls and displayed as relative protein amounts using Fiji software

7.6 Immunohistochemistry

7.6.1 Tissue preparation

Mice were sacrificed by cervical dislocation and optic nerve, spinal cord and brain samples were immersion fixed in 4% paraformaldehyde (4% PFA, 0.1M Phosphate buffer, 0.5% NaCl) for 48h for immunohistochemistry.

7.6.2 Paraffin embedding

Fixed tissue was transferred to embedding cassettes and paraffin embedding was performed with a Tissue Processor (MICROM HMP 110).

The following program was used:

(1)	50% Ethanol	1 h
(2)	70% Ethanol	2x 2 h
(3)	96% Ethanol	2x 2 h
(4)	100% Ethanol	2x 2 h
(5)	Isopropanol	1 h
(6)	Xylol	2x 2 h
(7)	Paraffin	2x 2 h

Samples were transferred to metal forms and embedded in paraffin with the Embedding Station (MICROM AP 280). Paraffin blocks were stored at RT, cut in 5µm thick sections using the microtome (MICROM HM 400), mounted on slides and dried overnight at 37°C.

7.6.3 Histological and morphological analyses with DAB

Paraffin was removed from the sections with the following protocol:

(1)	60°C	10 min
(2)	Xylol	2x 10 min
(3)	Xylol/Isopropanol (1:1)	10 min
(4)	100% Ethanol	5 min
(5)	90% Ethanol	5 min
(6)	70% Ethanol	5 min
(7)	50% Ethanol	5 min
(8)	ddH_2O	5 min

Immunolabeling was performed as indicated (antibody list chapter 6.6) with either Dako- LSAB2 system (Dako) or Vector Elite ABC Kit (Vector Labs) following manufacturer's protocol. For chromogenic staining, deparaffinized sections were incubated and cooked with citrate buffer in a microwave for 10 min. After a cooling phase of 20 min, the samples were incubated in Tris buffer containing 2% milk powder for 5 min. The slides were sealed with coverplates (Thermo Fisher Scientific) to ensure even distribution of solutions. The slides were washed again with Tris buffer containing milk powder and in the following blocked with goat serum in PBS (1:5) for 10 min. The primary antibody was diluted in PBS/BSA and incubated at 4°C overnight. On the next day slides were rinsed with Tris buffer containing 2% milk powder and directly incubate with either Dako- LSAB2 system or Vector Elite ABC Kit. Slides were then washed with Tris buffer and coverplates were removed. For detection, 3,3'-Diaminobenzidine was applied by using the DAB Zytomed Kit (Zytomed Systems GmbH) for 10 min incubation time. After DAB was washed off nuclear staining of the samples was performed by incubation in Haematoxylin (0.1%). Slides were dipped in HCl for 10 sec and Scott's solution for 5 min.

In the end the samples were dehydrated using the following protocol:

(1)	ddH_2O	5 min
(2)	50% Ethanol	5 min
(3)	70% Ethanol	5 min
(4)	90% Ethanol	5 min
(5)	100% Ethanol	5 min

(6)	Xylol/Isopropanol (1:1)	10 min
(7)	Xylol	2x 10 min

Afterwards the slides were mounted with Eukitt (Kindler) and analyzed by light microscopy (Zeiss Axiophot Z1).

7.6.4 Histological fluorescent analyses

7.6.4.1 TUNEL/EdU Assay

Paraffin was removed from the slides as described in chapter 7.6.3. The slides were rinsed with 0.85% NaCl for 5min followed by washing with PBS for 5min. Deparaffinized sections were post-fixed with 4% PFA for 15min and then washed twice with PBS. Slides were put in an opaque chamber filled with wet tissue paper and incubated with proteinase K (20µg/ml) for 10 min at RT. After washing with PBS the slides were again fixed with 4% PFA for 5min. The slides were rinsed with PBS and TUNEL Equilibration Buffer was incubated for 10min, followed by the incubation with the rTDT Reaction Mix. Afterwards the section were rinsed with saline-sodium citrate SSC and washed three times with PBS. To inactivate the endogenous peroxidase, 0.3% H_2O_2 was applied to the section and incubated for 5min. After three times washing with PBS, Streptavidin-488 (1:200) in PBS was applied for 30min at RT, followed by three washing steps. The sections were blocked two times with 3% HS in PBS for 10min and then the EdU click-it-cocktail was incubated for 30min at RT. Finally the sections were blocked again, incubated with nuclei staining (Dapi 1:20000), washed with PBS and mounted with Aqua Poly Mount.

7.7 Electron microscopy

7.7.1 Tissue preparation

Mice were sacrificed by cervical dislocation and optic nerve and spinal cord samples were immersion fixed in Karlsson-Schultz fixation (Schultz and Karlsson, 1965) (4% PFA, 0.1M Phosphate buffer, 0.5% NaCl, 2.5% glutaraldehyde) for approximately one week.

7.7.2 Epon embedding

Region of interest of optic nerve and spinal cord samples was cut and stored, wrapped in a mesh, in baskets and put into the automated epon embedding machine (EMTP, Leica) running with the following protocol:

(1) Phosphate buffer 3 x 10 min
(2) 2% OsO_4 4 hours
(3) ddH_2O 3 x 10 min
(4) 30% Ethanol 20 min
(5) 50% Ethanol 20 min
(6) 70% Ethanol 20 min
(7) 90% Ethanol 20 min
(8) 100% Ethanol 4 x 10 min
(9) Propylenoxid 3 x 10 min
(10) Propylenoxid/Epon 2:1 2 hours
(11) Propylenoxid/Epon 1:1 2 hours
(12) Propylenoxid/Epon 1:2 4 hours
(13) Epon 4 hours

Afterwards samples were unwrapped, put into silicone moulds and polymerized in an oven at 60°C overnight.

7.7.3 Preparation of semi- and ultra-thin sections

For electron microscopic analyses, epon imbedded spinal cord was cut in semi-thin (0.5 mm) and ultra-thin (50-65nm) section on a microtome (Ultracut S, Leica) using a diamond knife (45°, Diatome).
Semi-thin section were mounted on slides and stained with azur-II-methylenblue for 1 min at 60°C. Ultra-thin sections were collected on formvar polyvinyl-coated copper grids and contrasted with 2% uranylacetate (30 min) and 1% lead citrate solution (12 min).

7.7.4 Electron microscopy and analysis

Pictures of uranyl acetate contrasted ultra-thin sections were taken with the LEO EM912AB electron microscope (Carl Zeiss NTS, Oberkochen, Germany) connected to an on-axis 2048x2048 CCD camera (Proscan, Scheuring, Germany).
At least 12 pictures from the corticospinal tract of the spinal cord were taken. To randomize the quantification of myelin thickness, the grid tool of the Fiji software was used. G-ratio measurements were performed as described with the ratio of fiber diameter divided by axon diameter (Saher et al., 2012). Data of unmyelinated axons and g-ratio was obtained from 100 axons/per animal. Mitochondrial thickness was measured for 100 randomly chosen mitochondria/per animal.

7.8 Blood-brain barrier permeability analysis

Evans blue solution (1%,0.5 µg/ g body weight; Sigma) was intravenously injected and allowed to circulate for four hours. Mice were anesthetized with avertin intraperitoneally (0.2 ml per 10g body weight) followed by perfusion for 15 min at 2.5 ml/min with 1x phosphate buffered saline. Brain samples (excluding brain stem and olfactory bulbs) were rinsed with PBS and cut sagittally. Hemispheres were frozen on dry ice and lyophilisated (Christ LMC-1 BETA 1-16) at -36 °C for 24 h under vacuum of 0.2 mBar. Evans blue was extracted from brain samples in 10 µl formamide (Sigma) per mg brain at 57°C for 24 h. Quantification of Evans blue fluorescence was done in triplicates on a fluorescent microscope (Observer Z2, Zeiss) connected with an AxioCam MRc3, x1 Camera Adaptor and the ZEN 2012 blue edition software recorded at x10 magnification. The concentration of Evans blue was calculated using a standard curve and normalized to matched controls.

7.9 Tissue culture

7.9.1 Thawing and cultivation of GL261-GFP cells

Frozen cryovials containing GL261-GFP cells in DMEM (+20% FCS +10% DMSO) were removed from the liquid nitrogen tank, thawed in the water bath at 37°C and then mixed with fresh media in a PLL-coated 75cm^2 flask. The cells were allowed to attach and further cultivated in the incubator at 37°C and 5% CO_2. Twice a week cells were washed with PBS, trypsinated and centrifuged at 800rpm for 10min. For implantation cells were counted and resuspended in PBS (75000 cells/5µl) and for keeping them in culture resuspended in media.

7.9.2 Cayman's WST1-Assay

Cayman's WST1 assay serves as a tool to analyze cell proliferation and therefore cell viability. The assay is based on the fact that tetrazolium salt WST-1 is cleaved by cellular mitochondrial dehydrogenases to formazan, which can only occur in living cells.

For this assay cells are plated in a 96-well plate in a density of 10^4-10^5 cells per well dissolved in a volume of 100µl. Cultured cells were allowed to grow in an incubator at 37°C for 24 - 72h. The reagent mix was prepared by mixing equal amounts of Electron Mediator Solution and WST-1 Developer Reagent, which were both provided in the kit. Subsequently 10µl of the mix was added to each well and mixed gently on a shaker for one minute. Adherent cultures were incubated for 2h at 37°C and suspension cultures for 4h. Afterwards the 96-well plates were again shaked for one minute to ensure homogeneous mixture of the color. The absorbance was then measured in a plate reader at a wavelength of 450nm.

7.9.3 Dose-response test: treatment of GL261 cells with cisplatin

For the dose-response measurement of the GL261 cells with cisplatin, cells were cultivated as described in chapter 7.9.1. Plating was performed in a 96 well plate with 10^4 cells per well. Media was changed every day. After 24h the plating density reached 50-75% confluence, after 48h 90% and after 72h complete confluence. Cells

were treated with an increasing dose of cisplatin from 0.025 µg/ml up to 50 µg/ml dissolved in saline. WST-1 measurements (chapter 7.9.2) were performed after 24, 48 and 72h. Adherent cultures (72h) were incubated in WST-1 reagent mix for 2h at 37°C and suspension cultures (24h and 48h) for 4h. As positive control we used living cells dissolved in saline and as negative control we used cells with 2 mmol H_2O_2.

7.10 Magnetic resonance imaging (MRI)

Magnetic resonance imaging was performed in collaboration with Thomas Michaelis, Takashi Watanabe and Sabine Höfer from the Biomedizinische NMR Forschungs GmbH, Head Prof. Jens Frahm. Quantification on T_1-weighted MRI was used to analyze tumor volume. Single images were analyzed, positive tumor area selected and tumor volume was quantified with Amira Software.

7.11 Behavioral analyses

7.11.1 Elevated beam test

Motor coordination was assessed with the elevated beam test (in-house made, MPI of experimental medicine) every other week starting with 6 weeks of age. Mice were put on a beam (width 1.5 cm) and allowed to run toward a hiding box (Figure 7.1). The number of slips in a defined 55 cm distance was assessed as a mean of two best of three repeats per time point.

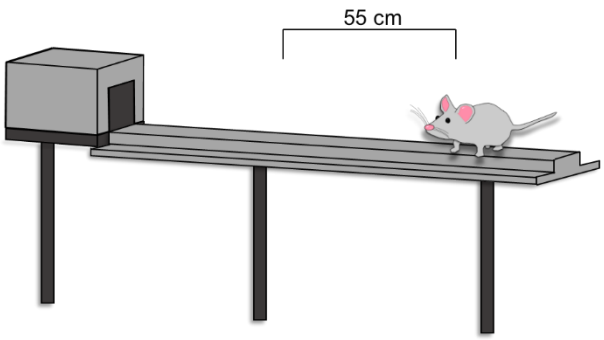

Figure 7.1| Elevated beam test

7.11.2 Rotarod

Motor performance and balance were weekly measured with the rotarod (in-house made, MPI of experimental medicine, 3cm diameter) starting with two weeks of age (Figure 7.2). Mice were placed on the rotarod starting with a speed of 4 rpm. Speed was increased with 10 rpm/min until 26 rpm was reached and held for 10sec. Trial was complete after 150sec and the latency to fall was recorded.

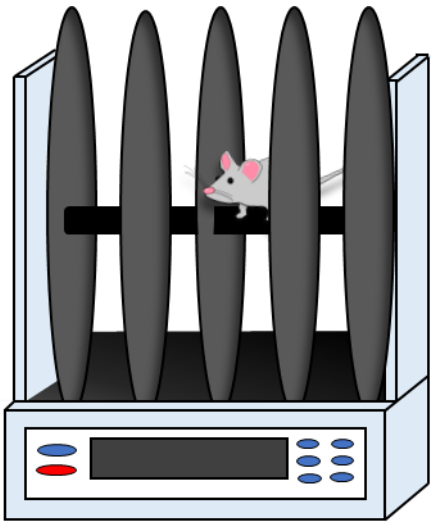

Figure 7.2| Rotarod

7.12 Statistical evaluation

Values are expressed as mean. All error bars show s.e.m. Statistical significance was calculated as indicated in figure legends by either one or two-way ANOVA or Student's t-test of two-tailed uncoupled samples, and P-values are shown as *, P<0.05; **, P<0.01; ***, P<0.001; ****, P<0.0001.

8 References

Abbott, N.J., Friedman, A., 2012. Overview and introduction: The blood-brain barrier in health and disease. Epilepsia 53, 1–6. doi:10.1111/j.1528-1167.2012.03696.x

Abbott, N.J., Patabendige, A.A.K., Dolman, D.E.M., Yusof, S.R., Begley, D.J., 2010. Structure and function of the blood-brain barrier. Neurobiol. Dis. 37, 13–25. doi:10.1016/j.nbd.2009.07.030

Abbott, N.J., Rönnbäck, L., Hansson, E., 2006. Astrocyte-endothelial interactions at the blood-brain barrier. Nat. Rev. Neurosci. 7, 41–53. doi:10.1038/nrn1824

Abou-Sleiman, P.M., Muqit, M.M.K., Wood, N.W., 2006. Expanding insights of mitochondrial dysfunction in Parkinson's disease. Nat. Rev. Neurosci. 7, 207–219. doi:10.1038/nrn1868

Acharya, N.K., Goldwaser, E.L., Forsberg, M.M., Godsey, G.A., Johnson, C.A., Sarkar, A., DeMarshall, C., Kosciuk, M.C., Dash, J.M., Hale, C.P., Leonard, D.M., Appelt, D.M., Nagele, R.G., 2015. Sevoflurane and Isoflurane induce structural changes in brain vascular endothelial cells and increase blood-brain barrier permeability: Possible link to postoperative delirium and cognitive decline. Brain Res. 1620, 29–41. doi:10.1016/j.brainres.2015.04.054

Andrews, Z.B., Diano, S., Horvath, T.L., 2005. Mitochondrial uncoupling proteins in the CNS: In support of function and survival. Nat. Rev. Neurosci. 6, 829–840. doi:10.1038/nrn1767

Anelli, T., Sitia, R., 2008. Protein quality control in the early secretory pathway. EMBO J. 27, 315–327. doi:10.1038/sj.emboj.7601974

Appikatla, S., Bessert, D., Lee, I., Hüttemann, M., Mullins, C., Somayajulu-Nitu, M., Yao, F., Skoff, R.P., 2014. Insertion of proteolipid protein into oligodendrocyte mitochondria regulates extracellular pH and adenosine triphosphate. Glia 62, 356–373. doi:10.1002/glia.22591

Armulik, A., Genové, G., Mäe, M., Nisancioglu, M.H., Wallgard, E., Niaudet, C., He, L., Norlin, J., Lindblom, P., Strittmatter, K., Johansson, B.R., Betsholtz, C., 2010. Pericytes regulate the blood-brain barrier. Nature 468, 557–61. doi:10.1038/nature09522

Attwell, D., Buchan, A.M., Charpak, S., Lauritzen, M., MacVicar, B.A., Newman, E.A., 2010. Glial and neuronal control of brain blood flow. Nature 468, 232–243. doi:10.1038/nature09613

Ausman, J.I., Shapiro, W.R., Rall, D.P., 1970. Studies on the Chemotherapy of Experimental Brain Tumors : Development of an Experimental Model Studies on the Chemotherapy of Experimental Development of an Experimental Model Brain Tumors : 30, 2394–2400.

Balda, M.S., Whitney, J.A., Flores, C., González, S., Cereijido, M., Matter, K., 1996. Functional dissociation of paracellular permeability and transepithelial electrical resistance and disruption of the apical-basolateral intramembrane diffusion barrier by expression of a mutant tight junction membrane protein. J. Cell Biol. 134, 1031–1049. doi:10.1083/jcb.134.4.1031

Bamforth, S.D., Kniesel, U., Wolburg, H., Engelhardt, B., Risau, W., 1999. A dominant mutant of occludin disrupts tight junction structure and function. J. Cell Sci. 112 (Pt 1, 1879–88.

Banks, W.A., Gray, A.M., Erickson, M.A., Salameh, T.S., Damodarasamy, M., Sheibani, N., Meabon, J.S., Wing, E.E., Morofuji, Y., Cook, D.G., Reed, M.J., 2015. Lipopolysaccharide-induced blood-brain barrier disruption: Roles of cyclooxygenase, oxidative stress, neuroinflammation, and elements of the neurovascular unit. J. Neuroinflammation 12, 1–15. doi:10.1186/s12974-015-0434-1

Barar, J., Rafi, M.A., Pourseif, M.M., Omidi, Y., 2016. Blood-brain barrier transport machineries and targeted therapy of brain diseases. BioImpacts 6, 225–248. doi:10.15171/bi.2016.30

Bartus, R.T., Elliott, P.J., Dean, R.L., Hayward, N.J., Nagle, T.L., Huff, M.R., Snodgrass, P.A., Blunt, D.G., 1996. Controlled modulation of BBB permeability using the bradykinin agonist, RMP-7. Exp. Neurol. 142, 14–28. doi:10.1006/exnr.1996.0175

Baumann, N., Pham-Dinh, D., 2001. Biology of oligodendrocyte and myelin in the mammalian central nervous system. Physiol. Rev. 81, 871–927.

Bazzoni, G., Dejana, E., 2004. Endothelial cell-to-cell junctions: molecular organization and role in vascular homeostasis. Physiol. Rev. 84, 869–901. doi:10.1152/physrev.00035.2003

Bélanger, M., Allaman, I., Magistretti, P.J., 2011. Brain energy metabolism: Focus on Astrocyte-neuron metabolic cooperation. Cell Metab. 14, 724–738. doi:10.1016/j.cmet.2011.08.016

Berghoff, S.A., Düking, T., Spieth, L., Winchenbach, J., Stumpf, S.K., Gerndt, N., Kusch, K., Ruhwedel, T., Möbius, W., Saher, G., 2017a. Blood-brain barrier hyperpermeability precedes demyelination in the cuprizone model. Acta Neuropathol. Commun. 5, 94. doi:10.1186/s40478-017-0497-6

Berghoff, S.A., Gerndt, N., Winchenbach, J., Stumpf, S.K., Hosang, L., Odoardi, F., Ruhwedel, T., Böhler, C., Barrette, B., Stassart, R., Liebetanz, D., Dibaj, P., Möbius, W., Edgar, J.M., Saher, G., 2017b. Dietary cholesterol promotes repair of demyelinated lesions in the adult brain. Nat. Commun. 8. doi:10.1038/ncomms14241

Björkhem, I., Meaney, S., Fogelman, A.M., 2004. Brain Cholesterol: Long Secret Life behind a Barrier. Arterioscler. Thromb. Vasc. Biol. 24, 806–815. doi:10.1161/01.ATV.0000120374.59826.1b

Blanchette, M., Daneman, R., 2015. Formation and maintenance of the BBB. Mech. Dev. 138, 8–16. doi:10.1016/j.mod.2015.07.007

Blood, T., Barrier, B., Daneman, R., Prat, A., 2015. The Blood –Brain Barrier 1–23. doi:10.1101/cshperspect.a020412

Boison, D., Stoffel, W., 1994. Disruption of the compacted myelin sheath of axons of the central nervous system in proteolipid protein-deficient mice. Proc. Natl. Acad. Sci. U. S. A. 91, 11709–13.

Boucher, S.E.M., Cypher, M. a, Carlock, L.R., Skoff, R.P., 2002. Proteolipid protein gene modulates viability and phenotype of neurons. J. Neurosci. 22, 1772–1783. doi:22/5/1772 [pii]

Bough, K.J., Rho, J.M., 2007. Anticonvulsant mechanisms of the ketogenic diet. Epilepsia 48, 43–58. doi:10.1111/j.1528-1167.2007.00915.x

Brightman, M.W., 1969. Junctions Between Intimately Apposed Cell Membranes in the Vertebrate Brain. J. Cell Biol. 40, 648–677. doi:10.1083/jcb.40.3.648

Brightman, M.W., Hori, M., Rapoport, S.I., Reese, T.S., Westergaard, E., 1973. Osmotic opening of tight junctions in cerebral endothelium. J. Comp. Neurol. 152, 317–25. doi:10.1002/cne.901520402

Brown, R.C., Davis, T.P., 2002. Calcium modulation of adherens and tight junction function: A potential mechanism for blood-brain barrier disruption after stroke. Stroke 33, 1706–1711. doi:10.1161/01.STR.0000016405.06729.83

Butte, N.., 1999. “Adjustments in energy expenditure and substrate utilization during late pregnancy and lactation.” Am. J. Clin. Nutr. 69, 299–307.

Camire, R.B., Beaulac, H.J., Brule, S.A., McGregor, A.I., Lauria, E.E., Willis, C.L., 2014. Biphasic Modulation of Paracellular Claudin-5 Expression in Mouse Brain Endothelial Cells Is Mediated through the Phosphoinositide-3-Kinase/AKT Pathway. J. Pharmacol. Exp. Ther. 351, 654–662. doi:10.1124/jpet.114.218339

Camire, R.B., Beaulac, H.J., Willis, C.L., 2015. Transitory loss of glia and the subsequent modulation in inflammatory cytokines/chemokines regulate paracellular claudin-5 expression in endothelial cells. J. Neuroimmunol. 284, 57–66. doi:10.1016/j.jneuroim.2015.05.008

Cao, Y., Ni, C., Li, Z., Li, L., Liu, Y., Wang, C., Zhong, Y., Cui, D., Guo, X., 2015. Isoflurane anesthesia results in reversible ultrastructure and occludin tight junction protein expression changes in hippocampal blood-brain barrier in aged rats. Neurosci. Lett. 587, 51–6. doi:10.1016/j.neulet.2014.12.018

Cardoso, F.L., Herz, J., Fernandes, A., Rocha, J., Sepodes, B., Brito, M.A., McGavern, D.B., Brites, D., 2015. Systemic inflammation in early neonatal mice induces transient and lasting neurodegenerative effects. J. Neuroinflammation 12, 1–18. doi:10.1186/s12974-015-0299-3

Casellas, J., 2011. Inbred mouse strains and genetic stability: A review. Animal 5, 1–7. doi:10.1017/S1751731110001667

Cerghet, M., Bessert, D.A., Nave, K.A., Skoff, R.P., 2002. Differential expression of apoptotic markers in jimpy and in Plp overexpressors: Evidence for different apoptotic pathways. J. Neurocytol. 30, 841–855. doi:10.1023/A:1019697506757

Chai, D., Jiang, H., Li, Q., 2016. Isoflurane neurotoxicity involves activation of hypoxia inducible factor-1?? via intracellular calcium in neonatal rodents. Brain Res. 1653, 39–50. doi:10.1016/j.brainres.2016.10.014

Chen, C., Hu, Q., Yan, J., Yang, X., Shi, X., Lei, J., Chen, L., Huang, H., Han, J., Zhang, J.H., Zhou, C., 2009. Early inhibition of HIF-1α with small interfering RNA reduces ischemic-reperfused brain injury in rats. Neurobiol. Dis. 33, 509–517. doi:10.1016/j.nbd.2008.12.010

Chen, X., Threlkeld, S.W., Cummings, E.E., Juan, I., Makeyev, O., Besio, W.G., Gaitanis, J., Banks, W.A., Sadowska, G.B., Stonestreet, B.S., 2012. Ischemia–reperfusion impairs blood–brain barrier function and alters tight junction protein expression in the ovine fetus. Neuroscience 226, 89–100. doi:10.1016/j.neuroscience.2012.08.043

Chetty, R., Gatter, K., 1994. CD3: structure, function, and role of immunostaining in clinical practice. J. Pathol. 173, 303–7. doi:10.1002/path.1711730404

Chodobski, A., Zink, B.J., Szmydynger-chodobska, J., 2012. Blood-brain barrier pathophysiology in traumatic brain injury, Translational stroke research. doi:10.1007/s12975-011-0125-x.Blood-brain

Chrast, R., Saher, G., Nave, K.-A., Verheijen, M.H.G., 2011. Lipid metabolism in myelinating glial cells: lessons from human inherited disorders and mouse models. J. Lipid Res. 52, 419–34. doi:10.1194/jlr.R009761

Coisne, C., Engelhardt, B., 2011. Tight Junctions in Brain Barriers During Central Nervous System Inflammation. Antioxid. Redox Signal. 15, 1285–1303. doi:10.1089/ars.2011.3929

Cooper, I., Last, D., Guez, D., Sharabi, S., Goldman, S.E., Lubitz, I., Daniels, D., Salomon, S., Tamar, G., Tamir, T., Mardor, R., Fridkin, M., Shechter, Y., Mardor, Y., 2015. Combined Local Blood–Brain Barrier Opening and Systemic Methotrexate for the Treatment of Brain Tumors. J. Cereb. Blood Flow Metab. 35, 967–976. doi:10.1038/jcbfm.2015.6

Cremer, J.E., 1982. Substrate Utilization and Brain Development. J. Cereb. Blood Flow Metab. 2, 394–407. doi:10.1038/jcbfm.1982.45

Daneman, R., Prat, A., 2015. The blood-brain barrier. Cold Spring Harb. Perspect. Biol. 7, a020412. doi:10.1101/cshperspect.a020412

Daneman, R., Zhou, L., Agalliu, D., Cahoy, J.D., Kaushal, A., Barres, B. a., 2010a. The mouse blood-brain barrier transcriptome: A new resource for understanding the development and function of brain endothelial cells. PLoS One 5, 1–16. doi:10.1371/journal.pone.0013741

Daneman, R., Zhou, L., Kebede, A.A., Barres, B.A., 2010b. Pericytes are required for blood-brain barrier integrity during embryogenesis. Nature 468, 562–6. doi:10.1038/nature09513

Davis, M., 2016. Glioblastoma: Overview of Disease and Treatment. Clin. J. Oncol. Nurs. 20, S2–S8. doi:10.1188/16.CJON.S1.2-8

de Vries, H.E., Blom-Roosemalen, M.C., de Boer, a G., van Berkel, T.J., Breimer, D.D., Kuiper, J., 1996. Effect of endotoxin on permeability of bovine cerebral endothelial cell layers in vitro. J. Pharmacol. Exp. Ther. 277, 1418–1423. doi:10.1016/0165-5728(94)90577-0

de Vries, H.E., Kuiper, J., de Boer, A.G., Van Berkel, T.J., Breimer, D.D., 1997. The blood-brain barrier in neuroinflammatory diseases. Pharmacol. Rev. 49, 143–55.

Dejana, E., 2004. Endothelial cell-cell junctions: Happy together. Nat. Rev. Mol. Cell Biol. 5, 261–270. doi:10.1038/nrm1357

Dejana, E., Orsenigo, F., Lampugnani, M.G., 2008. The role of adherens junctions and VE-cadherin in the control of vascular permeability. J. Cell Sci. 121, 2115–2122. doi:10.1242/jcs.017897

Dhaunchak, A., Nave, K., 2007. A common mechanism of PLP/DM20 misfolding causes cysteine-mediated endoplasmic reticulum retention in oligodendrocytes and Pelizaeus-Merzbacher disease. Proc. Natl. Acad. Sci. U. S. A. 104, 17813–8. doi:10.1073/pnas.0704975104

Dhaunchak, A.S., Colman, D.R., Nave, K.-A., 2011. Misalignment of PLP/DM20 transmembrane domains determines protein misfolding in Pelizaeus-Merzbacher disease. J. Neurosci. 31, 14961–71. doi:10.1523/JNEUROSCI.2097-11.2011

Dhopeshwarkar, G.A., Mead, J.F., 1969. Fatty acid uptake by the brain. II. Incorporation of [I-14C] palmitic acid into the adult rat brain. Biochim. Biophys. Acta 187, 461–7. doi:10.1016/j.bbagen.2008.12.001

Dhopeshwarkar, G.A., Mead, J.F., 1970. Fatty acid uptake by the brain. 3. Incorporation of (1-14C)oleic acid into the adult rat brain. Biochim. Biophys. Acta 210, 250–6.

Dhopeshwarkar, G.A., Subramanian, C., Mead, J.F., 1971. Fatty acid uptake by the brain. IV. Incorporation of (I-14C)linoleic acid into the adult rat brain. Biochim. Biophys. Acta 231, 8–14.

Durukan, A., Tatlisumak, T., 2007. Acute ischemic stroke: Overview of major experimental rodent models, pathophysiology, and therapy of focal cerebral ischemia. Pharmacol. Biochem. Behav. 87, 179–197. doi:10.1016/j.pbb.2007.04.015

Ebert, D., Haller, R.G., Walton, M.E., 2003. Energy contribution of octanoate to intact rat brain metabolism measured by 13C nuclear magnetic resonance spectroscopy. J. Neurosci. 23, 5928–35. doi:23/13/5928 [pii]

Eckel, R.H., Hanson, A.S., Chen, A.Y., Berman, J.N., Yost, T.J., Brass, E.P., 1992. Dietary substitution of medium-chain triglycerides improves insulin-mediated glucose metabolism in NIDDM subjects. Diabetes 41, 641–647. doi:10.2337/diab.41.5.641

Edgar, J.M., McCulloch, M.C., Montague, P., Brown, A.M., Thilemann, S., Pratola, L., Gruenenfelder, F.I., Griffiths, I.R., Nave, K.-A., 2010. Demyelination and axonal preservation in a transgenic mouse model of Pelizaeus-Merzbacher disease. EMBO Mol. Med. 2, 42–50. doi:10.1002/emmm.200900057

Epplen, D.B., Prukop, T., Nientiedt, T., Albrecht, P., Arlt, F.A., Stassart, R.M., Kassmann, C.M., Methner, A., Nave, K., Werner, H.B., Sereda, M.W., 2015. Curcumin therapy in a Plp1 transgenic mouse model of Pelizaeus-Merzbacher disease. Ann. Clin. Transl. Neurol. 2, 787–96. doi:10.1002/acn3.219

Farina Hanif, Kanza Muzaffar, Kahkashan Perveen, Saima M Malhi, Shabana U Simjee, 2017. Glioblastoma Multiforme: A Review of its Epidemiology and Pathogenesis through Clinical Presentation and Treatment. Asian Pacific J. Cancer Prev. J Cancer Prev 18, 3–9. doi:10.22034/APJCP.2017.18.1.3

Feng, S., Cen, J., Huang, Y., Shen, H., Yao, L., Wang, Y., Chen, Z., 2011. Matrix metalloproteinase-2 and -9 secreted by leukemic cells increase the permeability of blood-brain barrier by disrupting tight junction proteins. PLoS One 6. doi:10.1371/journal.pone.0020599

Fischer, S., Wobben, M., Marti, H.H., Renz, D., Schaper, W., 2002. Hypoxia-induced hyperpermeability in brain microvessel endothelial cells involves VEGF-mediated changes in the expression of zonula occludens-1. Microvasc. Res. 63, 70–80. doi:10.1006/mvre.2001.2367

Fitzgerald, J.E., Schardein, J.L., Kurtz, S.M., 1974. Spontaneous tumors of the nervous system in albino rats. J. Natl. Cancer Inst. 52, 265–273. doi:10.1093/jnci/52.1.265

Fraser, H., 1971. Astrocytomas in an inbred mouse strain. J. Pathol. 103, 266–70.

Fünfschilling, U., Supplie, L.M., Mahad, D., Boretius, S., Saab, A.S., Edgar, J., Brinkmann, B.G., Kassmann, C.M., Tzvetanova, I.D., Möbius, W., Diaz, F., Meijer, D., Suter, U., Hamprecht, B., Sereda, M.W., Moraes, C.T., Frahm, J., Goebbels, S., Nave, K.-A., 2012. Glycolytic oligodendrocytes maintain myelin and long-term axonal integrity. Nature 485, 517–21. doi:10.1038/nature11007

Garbern, J.Y., Yool, D.A., Moore, G.J., Wilds, I.B., Faulk, M.W., Klugmann, M., Nave, K., Sistermans, E.A., van der Knaap, M.S., Bird, T.D., Shy, M.E., Kamholz, J.A., Griffiths, I.R., 2002. Patients lacking the major CNS myelin protein, proteolipid protein 1, develop length-dependent axonal degeneration in the absence of demyelination and inflammation. Brain 125, 551–61.

Garrido-Urbani, S., Bradfield, P.F., Imhof, B.A., 2014. Tight junction dynamics: The role of junctional adhesion molecules (JAMs). Cell Tissue Res. 355, 701–715. doi:10.1007/s00441-014-1820-1

Gerhardt, H., 1999. N-cadherin expression in endothelial cells during early angiogenesis in the eye and brain of the chicken: Relation to blood-retina and blood-brain barrier development. Eur. J. Neurosci. 11, 1191–1201. doi:10.1046/j.1460-9568.1999.00526.x

Gopalakrishnan, G., Awasthi, A., Belkaid, W., De Faria, O., Liazoghli, D., Colman, D.R., Dhaunchak, A.S., 2013. Lipidome and proteome map of myelin membranes. J. Neurosci. Res. 91, 321–334. doi:10.1002/jnr.23157

Gottardo, N., Gajjar, A., 2008. Chemotherapy for malignant brain tumors of childhood. J. Child Neurol. 23, 1149–1159. doi:10.1177/0883073808321765.Chemotherapy

Gow, A., Friedrich, V.L., Lazzarini, R.A., 1994. Many naturally occurring mutations of myelin proteolipid protein impair its intracellular transport. J. Neurosci. Res. 37, 574–83. doi:10.1002/jnr.490370504

Gow, A., Southwood, C.M., Lazzarini, R.A., 1998. Disrupted proteolipid protein trafficking results in oligodendrocyte apoptosis in an animal model of Pelizaeus-Merzbacher disease. J. Cell Biol. 140, 925–34.

Griffiths, I.R., Scott, I., McCulloch, M.C., Barrie, J.A., McPhilemy, K., Cattanach, B.M., 1990. Rumpshaker mouse: a new X-linked mutation affecting myelination: evidence for a defect in PLP expression. J. Neurocytol. 19, 273–83. doi:10.1007/BF01217305

Halestrap, A.P., 2013. The SLC16 gene family-Structure, role and regulation in health and disease. Mol. Aspects Med. 34, 337–349. doi:10.1016/j.mam.2012.05.003

Hall, C.N., Reynell, C., Gesslein, B., Hamilton, N.B., 2014. Europe PMC Funders Group Capillary pericytes regulate cerebral blood flow in health and disease 508, 55–60. doi:10.1038/nature13165.Capillary

Hanazaki, M., Chiba, Y., Yokoyama, M., Morita, K., Kohjitani, A., Sakai, H., Misawa, M., 2008. Y-27632 augments the isoflurane-induced relaxation of bronchial smooth muscle in rats. J. Smooth Muscle Res. 44, 189–93.

Hartsock, A., Nelson, W.J., 2008. Adherens and tight junctions: Structure, function and connections to the actin cytoskeleton. Biochim. Biophys. Acta - Biomembr. 1778, 660–669. doi:10.1016/j.bbamem.2007.07.012

Hernández-Pedro, N.Y., Rangel-López, E., Magaña-Maldonado, R., de la Cruz, V.P., del Angel, A.S., Pineda, B., Sotelo, J., 2013. Application of nanoparticles on diagnosis and therapy in gliomas. Biomed Res. Int. 2013, 351031. doi:10.1155/2013/351031

Hervé, F., Ghinea, N., Scherrmann, J.-M., 2008. CNS Delivery Via Adsorptive Transcytosis. AAPS J. 10, 455–472. doi:10.1208/s12248-008-9055-2

Hirrlinger, J., Nave, K.-A., 2014. Adapting brain metabolism to myelination and long-range signal transduction. Glia. doi:10.1002/glia.22737

Hogan, V., White, K., Edgar, J., McGill, A., Karim, S., McLaughlin, M., Griffiths, I., Turnbull, D., Nichols, P., 2009. Increase in mitochondrial density within axons and supporting cells in response to demyelination in the Plp1 mouse model. J. Neurosci. Res. 87, 452–459. doi:10.1002/jnr.21867

Huppert, J., Closhen, D., Croxford, A., White, R., Kulig, P., Pietrowski, E., Bechmann, I., Becher, B., Luhmann, H.J., Waisman, A., Kuhlmann, C.R.W., 2010. Cellular mechanisms of IL-17-induced blood-brain barrier disruption. FASEB J. 24, 1023–1034. doi:10.1096/fj.09-141978

Hüttemann, M., Zhang, Z., Mullins, C., Bessert, D., Lee, I., Nave, K.-A., Appikatla, S., Skoff, R.P., 2009. Different proteolipid protein mutants exhibit unique metabolic defects. ASN Neuro 1, 165–180. doi:10.1042/AN20090028

Huttenlocher, P.R., Wilbourn, A.J., Signore, J.M., 1971. Medium-chain triglycerides as a therapy for intractable childhood epilepsy. Neurology 21, 1097–103. doi:10.1006/mgme.2000.3069

Ikenouchi, J., Furuse, M., Furuse, K., Sasaki, H., Tsukita, S., Tsukita, S., 2005. Tricellulin constitutes a novel barrier at tricellular contacts of epithelial cells. J. Cell Biol. 171, 939–945. doi:10.1083/jcb.200510043

Jahn, O., Tenzer, S., Werner, H.B., 2009. Myelin proteomics: molecular anatomy of an insulating sheath. Mol. Neurobiol. 40, 55–72. doi:10.1007/s12035-009-8071-2

Jansen, P.J., Lütjohann, D., Abildayeva, K., Vanmierlo, T., Plösch, T., Plat, J., von Bergmann, K., Groen, A.K., Ramaekers, F.C.S., Kuipers, F., Mulder, M., 2006. Dietary plant sterols accumulate in the brain. Biochim. Biophys. Acta 1761, 445–53. doi:10.1016/j.bbalip.2006.03.015

Jia, W., Lu, R., Martin, T.A., Jiang, W.G., 2014. The role of claudin-5 in blood-brain barrier (BBB) and brain metastases (Review). Mol. Med. Rep. 9, 779–785. doi:10.3892/mmr.2013.1875

Jiang, H., Huang, Y., Xu, H., Sun, Y., Han, N., Li, Q.F., 2012. Hypoxia inducible factor-1α is involved in the neurodegeneration induced by isoflurane in the brain of neonatal rats. J. Neurochem. 120, 453–460. doi:10.1111/j.1471-4159.2011.07589.x

Johns, T.G., Bernard, C.C., 1999. The structure and function of myelin oligodendrocyte glycoprotein. J. Neurochem. 72, 1–9.

Kagawa, T., Ikenaka, K., Inoue, Y., Kuriyama, S., Tsujii, T., Nakao, J., Nakajima, K., Aruga, J., Okano, H., Mikoshiba, K., 1994. Glial cell degeneration and hypomyelination caused by overexpression of myelin proteolipid protein gene. Neuron 13, 427–42.

Kaneko, M., Yasui, S., Niinuma, Y., Arai, K., Omura, T., Okuma, Y., Nomura, Y., 2007. A different pathway in the endoplasmic reticulum stress-induced expression of human HRD1 and SEL1 genes. FEBS Lett. 581, 5355–5360. doi:10.1016/j.febslet.2007.10.033

Karahashi, H., Michelsen, K.S., Arditi, M., 2009. Lipopolysaccharide-Induced Apoptosis in Transformed Bovine Brain Endothelial Cells and Human Dermal Microvessel Endothelial Cells: The Role of JNK. J. Immunol. 182, 7280–7286. doi:10.4049/jimmunol.0801376

Karim, S. a, Barrie, J. a, McCulloch, M.C., Montague, P., Edgar, J.M., Iden, D.L., Anderson, T.J., Nave, K.-A., Griffiths, I.R., McLaughlin, M., 2010. PLP/DM20 expression and turnover in a transgenic mouse model of Pelizaeus-Merzbacher disease. Glia 58, 1727–38. doi:10.1002/glia.21043

Kaur, C., Ling, E. a, 2008. Blood brain barrier in hypoxic-ischemic conditions. Curr. Neurovasc. Res. 5, 71–81. doi:10.2174/156720208783565645

Keaney, J., Campbell, M., 2015. The dynamic blood-brain barrier. FEBS J. 282, 4067–4079. doi:10.1111/febs.13412

Kebir, H., Kreymborg, K., Ifergan, I., Dodelet-devillers, A., Cayrol, R., Bernard, M., Giuliani, F., Arbour, N., Becher, B., 2007. Human T H 17 lymphocytes promote blood-brain barrier disruption and central nervous system inflammation. Nat. Med. 13, 4–6. doi:10.1038/nm1651

Kemper, E.M., Boogerd, W., Thuis, I., Beijnen, J.H., van Tellingen, O., 2004. Modulation of the blood-brain barrier in oncology: Therapeutic opportunities for the treatment of brain tumours? Cancer Treat. Rev. doi:10.1016/j.ctrv.2004.04.001

Kim, M., Ham, A., Kim, K.Y., Brown, K.M., Lee, H.T., 2014. The volatile anesthetic isoflurane increases endothelial adenosine generation via microparticle ecto-5'-nucleotidase (CD73) release. PLoS One 9, e99950. doi:10.1371/journal.pone.0099950

Kim, W.S., Weickert, C.S., Garner, B., 2008. Role of ATP-binding cassette transporters in brain lipid transport and neurological disease. J. Neurochem. 104, 1145–1166. doi:10.1111/j.1471-4159.2007.05099.x

Klugmann, M., Schwab, M.H., Pühlhofer, A., Schneider, A., Zimmermann, F., Griffiths, I.R., Nave, K.A., 1997. Assembly of CNS myelin in the absence of proteolipid protein. Neuron 18, 59–70.

Koper, J.W., Lopes-Cardozo, M., Van Golde, L.M., 1981. Preferential utilization of ketone bodies for the synthesis of myelin cholesterol in vivo. Biochim. Biophys. Acta 666, 411–7.

Koukourakis, G. V., Kouloulias, V., Zacharias, G., Papadimitriou, C., Pantelakos, P., Maravelis, G., Fotineas, A., Beli, I., Chaldeopoulos, D., Kouvaris, J., 2009. Temozolomide with radiation therapy in high grade brain gliomas: Pharmaceuticals considerations and efficacy; a review article. Molecules 14, 1561–1577. doi:10.3390/molecules14041561

Krämer-Albers, E.-M., Gehrig-Burger, K., Thiele, C., Trotter, J., Nave, K.-A., 2006. Perturbed interactions of mutant proteolipid protein/DM20 with cholesterol and lipid rafts in oligodendroglia: implications for dysmyelination in spastic paraplegia. J. Neurosci. 26, 11743–52. doi:10.1523/JNEUROSCI.3581-06.2006

Krebs, H.A., Williamson, D.H., Bates, M.W., Ann Page, M., Hawkins, R.A., 1971. The role of ketone bodies in caloric homeostasis. Adv. Enzyme Regul. 9, 387–409. doi:10.1016/S0065-2571(71)80055-9

Kroll, R.A., Neuwelt, E.A., 1998. Outwitting the blood-brain barrier for therapeutic purposes: Osmotic opening and other means. Neurosurgery 42, 1083–1100. doi:10.1097/00006123-199805000-00082

Lakhan, S.E., Kirchgessner, A., Tepper, D., Leonard, A., 2013. Matrix metalloproteinases and blood-brain barrier disruption in acute ischemic stroke. Front. Neurol. 4 APR, 1–15. doi:10.3389/fneur.2013.00032

Lappe-Siefke, C., Goebbels, S., Gravel, M., Nicksch, E., Lee, J., Braun, P.E., Griffiths, I.R., Navel, K.A., 2003. Disruption of Cnp1 uncouples oligodendroglial functions in axonal support and myelination. Nat. Genet. 33, 366–374. doi:10.1038/ng1095

Lee, C.Y., 2017. Strategies of temozolomide in future glioblastoma treatment. Onco. Targets. Ther. 10, 265–270. doi:10.2147/OTT.S120662

Lemkuil, B.P., Head, B.P., Pearn, M.L., Patel, H.H., Drummond, J.C., Patel, P.M., 2011. Isoflurane Neurotoxicity Is Mediated by p75NTR-RhoA Activation and Actin Depolymerization. Anesthesiology 114, 49–57. doi:10.1097/ALN.0b013e318201dcb3

Lenglet, S., Montecucco, F., Mach, F., Schaller, K., Gasche, Y., Copin, J.-C., 2014. Analysis of the expression of nine secreted matrix metalloproteinases and their endogenous inhibitors in the brain of mice subjected to ischaemic stroke. Thromb. Haemost. 112, 363–78. doi:10.1160/TH14-01-0007

Leten, C., Struys, T., Dresselaers, T., Himmelreich, U., 2014. In vivo and ex vivo assessment of the blood brain barrier integrity in different glioblastoma animal models. J. Neurooncol. 119, 297–306. doi:10.1007/s11060-014-1514-2

Linton, M.F., Gish, R., Hubl, S.T., Bütler, E., Esquivel, C., Bry, W.I., Boyles, J.K., Wardell, M.R., Young, S.G., 1991. Phenotypes of apolipoprotein B and apolipoprotein E after liver transplantation. J. Clin. Invest. 88, 270–281. doi:10.1172/JCI115288

Liu, H.-L., Huang, C.-Y., Chen, J.-Y., Wang, H.-Y.J., Chen, P.-Y., Wei, K.-C., 2014. Pharmacodynamic and therapeutic investigation of focused ultrasound-induced blood-brain barrier opening for enhanced temozolomide delivery in glioma treatment. PLoS One 9, e114311. doi:10.1371/journal.pone.0114311

Liu, H., Huang, C., Chen, J., Wang, H.J., Chen, P.-Y., Wei, K.-C., 2014. Pharmacodynamic and Therapeutic Investigation of Focused Ultrasound-Induced Blood-Brain Barrier Opening for Enhanced Temozolomide Delivery in Glioma Treatment. PLoS One 9, e114311. doi:10.1371/journal.pone.0114311

Liu, H., Yang, Y., Wang, Y., Tang, H., Zhang, F., Zhang, Y., Zhao, Y., 2018. Ketogenic diet for treatment of intractable epilepsy in adults: A meta-analysis of observational studies. Epilepsia Open 3, 9–17. doi:10.1002/epi4.12098

Liu, J., Jin, X., Liu, K.J., Liu, W., 2012. Matrix metalloproteinase-2-mediated occludin degradation and caveolin-1-mediated claudin-5 redistribution contribute to blood-brain barrier damage in early ischemic stroke stage. J. Neurosci. 32, 3044–57. doi:10.1523/JNEUROSCI.6409-11.2012

London, E., Brown, D.A., 2000. Insolubility of lipids in Triton X-100: Physical origin and relationship to sphingolipid/cholesterol membrane domains (rafts). Biochim. Biophys. Acta - Biomembr. 1508, 182–195. doi:10.1016/S0304-4157(00)00007-1

Lowry, O.H., Rosenbrough, N.J., Farr, A.L., Randall, R.J., 1951. Protein measurement with the Folin phenol reagent. J. Biol. Chem. 193, 265–75. doi:10.1016/0304-3894(92)87011-4

Lund, E.G., Guileyardo, J.M., Russell, D.W., 1999. cDNA cloning of cholesterol 24-hydroxylase, a mediator of cholesterol homeostasis in the brain. Proc. Natl. Acad. Sci. U. S. A. 96, 7238–43. doi:10.1073/PNAS.96.13.7238

Lv, S., Song, H.L., Zhou, Y., Li, L.X., Cui, W., Wang, W., Liu, P., 2010. Tumour necrosis factor-α affects blood-brain barrier permeability and tight junction-associated occludin in acute liver failure. Liver Int. 30, 1198–1210. doi:10.1111/j.1478-3231.2010.02211.x

Maes, W., Van Gool, S.W., 2011. Experimental immunotherapy for malignant glioma: lessons from two decades of research in the GL261 model. Cancer Immunol. Immunother. 60, 153–160. doi:10.1007/s00262-010-0946-6

Maier-Hauff, K., Ulrich, F., Nestler, D., Niehoff, H., Wust, P., Thiesen, B., Orawa, H., Budach, V., Jordan, A., 2011. Efficacy and safety of intratumoral thermotherapy using magnetic iron-oxide nanoparticles combined with external beam radiotherapy on patients with recurrent glioblastoma multiforme. J. Neurooncol. 103, 317–324. doi:10.1007/s11060-010-0389-0

Mantis, J.G., Meidenbauer, J.J., Zimick, N.C., Centeno, N. a, Seyfried, T.N., 2014. Glucose reduces the anticonvulsant effects of the ketogenic diet in EL mice. Epilepsy Res. 108, 1137–44. doi:10.1016/j.eplepsyres.2014.05.010

Marchiando, A.M., Shen, L., Vallen Graham, W., Weber, C.R., Schwarz, B.T., Austin, J.R., Raleigh, D.R., Guan, Y., Watson, A.J.M., Montrose, M.H., Turner, J.R., 2010. Caveolin-1-dependent occludin endocytosis is required for TNF-induced tight junction regulation in vivo. J. Cell Biol. 189, 111–126. doi:10.1083/jcb.200902153

Martìn-Padura, I., Lostaglio, S., Schneemann, M., Williams, L., Romano, M., Fruscella, P., Panzeri, C., Stoppacciaro, A., Ruco, L., Villa, A., Simmons, D., Dejana, E., 1998. Junctional adehsion moleculr, a novel member of the immunoglobulin superfamily that distributes at intracellular junctions and modulates monocyte transmigration. J. Cell Biol. 142, 117–127. doi:10.1083/jcb.142.1.117

Martini, R., Schachner, M., 1988. Immunoelectron microscopic localization of neural cell adhesion molecules (L1, N-CAM, and myelin-aasociated glycoprotein) in nerve regenerating adult mouse sciatic nerve. J. Cell Biol. 106, 1735–1746.

Masino, S.A., Rho, J.M., 2012. Mechanisms of Ketogenic Diet Action, Jasper's Basic Mechanisms of the Epilepsies. Elsevier Ltd. doi:10.1016/j.conb.2011.05.029

Matsukado, K., Inamura, T., Nakano, S., Fukui, M., Bartus, R.T., Black, K.L., 1996. Enhanced tumor uptake of carboplatin and survival in glioma-bearing rats by intracarotid infusion of bradykinin analog, RMP-7. Neurosurgery 39, 125–134. doi:10.1097/00006123-199607000-00025

Mitchell, R.W., On, N.H., Del Bigio, M.R., Miller, D.W., Hatch, G.M., 2011. Fatty acid transport protein expression in human brain and potential role in fatty acid transport across human brain microvessel endothelial cells. J. Neurochem. 117, 735–746. doi:10.1111/j.1471-4159.2011.07245.x

Montag, D., Giese, K.P., Bartsch, U., Martini, R., Lang, Y., Blüthmann, H., Karthigasan, J., Kirschner, D.A., Wintergerst, E.S., Nave, K.A., Zielasek, J., Toyka, K. V., Lipp, H.P., Schachner, M., 1994. Mice deficient for the glycoprotein show subtle abnormalities in myelin. Neuron 13, 229–246. doi:10.1016/0896-6273(94)90472-3

Morita, K., Sasaki, H., Furuse, M., Tsukita, S., 1999. Endothelial claudin: Claudin-5/TMVCF constitutes tight junction strands in endothelial cells. J. Cell Biol. 147, 185–194. doi:10.1083/jcb.147.1.185

Morris, A.A.M., 2005. Cerebral ketone body metabolism. J. Inherit. Metab. Dis. 28, 109–21. doi:10.1007/s10545-005-5518-0

Nagpal, S., 2012. The role of BCNU polymer wafers (Gliadel) in the treatment of malignant glioma. Neurosurg. Clin. N. Am. 23, 289–95, ix. doi:10.1016/j.nec.2012.01.004

Nave, K.A., Bloom, F.E., Milner, R.J., 1987. A single nucleotide difference in the gene for myelin proteolipid protein defines the jimpy mutation in mouse. J. Neurochem. 49, 1873–7.

Nave, K.A., Lai, C., Bloom, F.E., Milner, R.J., 1986. Jimpy mutant mouse: a 74-base deletion in the mRNA for myelin proteolipid protein and evidence for a primary defect in RNA splicing. Proc. Natl. Acad. Sci. U. S. A. 83, 9264–8.

Neal, E.G., Chaffe, H., Schwartz, R.H., Lawson, M.S., Edwards, N., Fitzsimmons, G., Whitney, A., Cross, J.H., 2008. The ketogenic diet for the treatment of childhood epilepsy: a randomised controlled trial. Lancet Neurol. 7, 500–506. doi:10.1016/S1474-4422(08)70092-9

Neishabouri, A.M., Faisal, A.A., 2011. The metabolic efficiency of myelinated vs unmyelinated axons. BMC Neurosci. 12, P100. doi:10.1186/1471-2202-12-S1-P100

Newcomb, E.W., Zagzag, D., 2009. The Murine GL261 Glioma Experimental Model to Assess Novel Brain Tumor Treatments. Humana Press, Totowa, NJ. doi:10.1007/978-1-60327-553-8

Newlands, E.S., Stevens, M.F., Wedge, S.R., Wheelhouse, R.T., Brock, C., 1997. Temozolomide: a review of its discovery, chemical properties, pre-clinical development and clinical trials. Cancer Treat. Rev. 23, 35–61.

Nitta, T., Hata, M., Gotoh, S., Seo, Y., Sasaki, H., Hashimoto, N., Furuse, M., Tsukita, S., 2003. Size-selective loosening of the blood-brain barrier in claudin-5-deficient mice. J. Cell Biol. 161, 653–660. doi:10.1083/jcb.200302070

Nussbaum, J.L., Roussel, G., 1983. Immunocytochemical demonstration of the transport of myelin proteolipids through the Golgi apparatus. Cell Tissue Res. 234, 547–559. doi:10.1007/BF00218650

O'Brien, J.S., Sampson, E.L., 1965. Lipid composition of the normal human brain: gray matter, white matter, and myelin. J. Lipid Res. 6, 537–44.

Oldendorf, W.H., Cornford, M.E., Brown, W.J., 1977. Large apparent work capability of blood-brain-barrier - study of mitochondrial content of capillary endothelial cells in brain and other tissues of rat. Ann Neurol 1, 409–417. doi:10.1002/ana.410010502

Olesen, S.P., Crone, C., 1986. Substances that rapidly augment ionic conductance of endothelium in cerebral venules. Acta Physiol. Scand. 127, 233–41. doi:10.1111/j.1748-1716.1986.tb07898.x

On, N., Alrushaia, S., Davies, N., Babu, S., Vanan, M., Siahaan, T., Miller, D., 2017. Transient Modulation of Blood-brain Barrier with E-cadherin Peptide Improves Adenanthin Penetration into the Brain for the Treatment of Medulloblastoma. J. Pharmacol. Toxicol. Methods 88, 174. doi:10.1016/j.vascn.2017.09.023

On, N.H., Kiptoo, P., Siahaan, T.J., Miller, D.W., 2014. Modulation of Blood–Brain Barrier Permeability in Mice Using Synthetic E-Cadherin Peptide. Mol. Pharm. 11, 974–981. doi:10.1021/mp400624v

Ostrom, Q.T., Gittleman, H., Farah, P., Ondracek, A., Chen, Y., Wolinsky, Y., Stroup, N.E., Kruchko, C., Barnholtz-Sloan, J.S., 2013. CBTRUS Statistical Report: Primary Brain and Central Nervous System Tumors Diagnosed in the United States in 2006-2010. Neuro. Oncol. 15, ii1-ii56. doi:10.1093/neuonc/not151

Pardridge, W.M., 2007. Blood-brain barrier delivery. Drug Discov. Today 12, 54–61. doi:10.1016/j.drudis.2006.10.013

Pellerin, L., Halestrap, A.P., Pierre, K., 2005. Cellular and subcellular distribution of monocarboxylate transporters in cultured brain cells and in the adult brain. J. Neurosci. Res. 79, 55–64. doi:10.1002/jnr.20307

Pellerin, L., Magistretti, P.J., 1994. Glutamate uptake into astrocytes stimulates aerobic glycolysis: a mechanism coupling neuronal activity to glucose utilization. Proc. Natl. Acad. Sci. 91, 10625–10629. doi:10.1073/pnas.91.22.10625

Peppiatt, C.M., Howarth, C., Mobbs, P., Attwell, D., 2006. Bidirectional control of CNS capillary diameter by pericytes. Nature 443, 700–704. doi:10.1038/nature05193

Peterson, D.L., Sheridan, P.J., Brown, W.E.J., 1994. Animal models for brain tumors: historical perspectives and future directions. J. Neurosurg. 80, 865–876.

Pfrieger, F.W., Ungerer, N., 2011. Cholesterol metabolism in neurons and astrocytes. Prog. Lipid Res. 50, 357–371. doi:10.1016/j.plipres.2011.06.002

Prados, M.D., Schold, S.C., Fine, H.A., Jaeckle, K., Mechtler, L., Fetell, M.R., Phuphanich, S., Feun, L., Janus, J., Ford, K., Graney, W., 2003. A randomized, double-blind, placebo-controlled, phase 2 study of RMP-7 in combination with carboplatin administered intravenously for the treatment of recurrent malignant glioma. Neuro. Oncol. 96–103.

Prukop, T., Epplen, D.B., Nientiedt, T., Wichert, S.P., Fledrich, R., Stassart, R.M., Rossner, M.J., Edgar, J.M., Werner, H.B., Nave, K.-A., Sereda, M.W., 2014. Progesterone antagonist therapy in a Pelizaeus-Merzbacher mouse model. Am. J. Hum. Genet. 94, 533–46. doi:10.1016/j.ajhg.2014.03.001

Qin, L.H., Huang, W., Mo, X.A., Chen, Y.L., Wu, X.H., 2015. LPS induces occludin dysregulation in cerebral microvascular endothelial cells via MAPK signaling and augmenting mmp-2 levels. Oxid. Med. Cell. Longev. 2015. doi:10.1155/2015/120641

Rao, R., 2009. Occludin phosphorylation in regulation of epithelial tight junctions. Ann. N. Y. Acad. Sci. 1165, 62–68. doi:10.1111/j.1749-6632.2009.04054.x

Razavi, S.-M., Lee, K.E., Jin, B.E., Aujla, P.S., Gholamin, S., Li, G., 2016. Immune Evasion Strategies of Glioblastoma. Front. Surg. 3, 1–9. doi:10.3389/fsurg.2016.00011

Readhead, C., Schneider, A., Griffiths, I.R., Nave, K.A., 1994. Premature arrest of myelin formation in transgenic mice with increased proteolipid protein gene dosage. Neuron 12, 583–95.

Reese, T.S., Karnovsky, M.J., 1967. Fine structural localizatin of blood-brain barrier to exogenous peroxidase. J. Cell Biol. 34, 207–217. doi:10.1083/jcb.34.1.207

Rempe, R.G., Hartz, A.M.S., Bauer, B., 2016. Matrix metalloproteinases in the brain and blood-brain barrier: Versatile breakers and makers. J. Cereb. Blood Flow Metab. 36, 1481–1507. doi:10.1177/0271678X16655551

Roach, A., Boylan, K., Horvath, S., Prusiner, S.B., Hood, L.E., 1983. Characterization of cloned cDNA representing rat myelin basic protein: Absence of expression in brain of shiverer mutant mice. Cell 34, 799–806. doi:10.1016/0092-8674(83)90536-6

Roboti, P., Swanton, E., High, S., 2009. Differences in endoplasmic-reticulum quality control determine the cellular response to disease-associated mutants of proteolipid protein. J. Cell Sci. 122, 3942–3953. doi:10.1242/jcs.055160

Rochfort, K.D., Cummins, P.M., 2015. The blood–brain barrier endothelium: a target for pro-inflammatory cytokines: Figure 1. Biochem. Soc. Trans. 43, 702–706. doi:10.1042/BST20140319

Romano, A., Koczwara, J.B., Gallelli, C.A., Vergara, D., Micioni Di Bonaventura, M.V., Gaetani, S., Giudetti, A.M., 2017. Fats for thoughts: An update on brain fatty acid metabolism. Int. J. Biochem. Cell Biol. 84, 40–45. doi:10.1016/j.biocel.2016.12.015

Ruiz, M., Bégou, M., Launay, N., Ranea-Robles, P., Bianchi, P., López-Erauskin, J., Morató, L., Guilera, C., Petit, B., Vaurs-Barriere, C., Guéret-Gonthier, C., Bonnet-Dupeyron, M.-N., Fourcade, S., Auwerx, J., Boespflug-Tanguy, O., Pujol, A., 2017. Oxidative Stress and Mitochondrial Dynamics Malfunction are linked in Pelizaeus-Merzbacher Disease. Brain Pathol. doi:10.1111/bpa.12571

Saeed, A.A., Genové, G., Li, T., Lütjohann, D., Olin, M., Mast, N., Pikuleva, I.A., Crick, P., Wang, Y., Griffiths, W., Betsholtz, C., Björkhem, I., 2014. Effects of a disrupted blood-brain barrier on cholesterol homeostasis in the brain. J. Biol. Chem. 289, 23712–23722. doi:10.1074/jbc.M114.556159

Saher, G., Brügger, B., Lappe-Siefke, C., Möbius, W., Tozawa, R., Wehr, M.C., Wieland, F., Ishibashi, S., Nave, K.-A., 2005. High cholesterol level is essential for myelin membrane growth. Nat. Neurosci. 8, 468–75. doi:10.1038/nn1426

Saher, G., Rudolphi, F., Corthals, K., Ruhwedel, T., Schmidt, K.-F., Löwel, S., Dibaj, P., Barrette, B., Möbius, W., Nave, K.-A., 2012a. Therapy of Pelizaeus-Merzbacher disease in mice by feeding a cholesterol-enriched diet. Nat. Med. 18, 1130–5. doi:10.1038/nm.2833

Saher, G., Rudolphi, F., Corthals, K., Ruhwedel, T., Schmidt, K.F., Löwel, S., Dibaj, P., Barrette, B., Möbius, W., Nave, K.A., 2012b. Therapy of Pelizaeus-Merzbacher disease in mice by feeding a cholesterol-enriched diet. Nat. Med. 18, 1130–1135. doi:10.1038/nm.2833

Saher, G., Stumpf, S.K., 2015. Cholesterol in myelin biogenesis and hypomyelinating disorders. Biochim. Biophys. Acta - Mol. Cell Biol. Lipids 1851, 1083–1094. doi:10.1016/j.bbalip.2015.02.010

Saitou, M., Furuse, M., Sasaki, H., Schulzke, J.-D., Fromm, M., Takano, H., Noda, T., Tsukita, S., 2000. Complex Phenotype of Mice Lacking Occludin, a Component of Tight Junction Strands. Mol. Biol. Cell 11, 4131–4142. doi:10.1091/mbc.11.12.4131

Sakakibara, A., Furuse, M., Saitou, M., Ando-Akatsuka, Y., Tsukita, S., 1997. Possible involvement of phosphorylation of occludin in tight junction formation. J. Cell Biol. 137, 1393–1401. doi:10.1083/jcb.137.6.1393

Sanovich, E., Bartus, R.T., Friden, P.M., Dean, R.L., Le, H.Q., Brightman, M.W., 1995. Pathway across blood-brain barrier opened by the bradykinin agonist, RMP-7. Brain Res. 705, 125–135. doi:10.1016/0006-8993(95)01143-9

Schneider, A.M., Griffiths, I.R., Readhead, C., Nave, K.A., 1995. Dominant-negative action of the jimpy mutation in mice complemented with an autosomal transgene for myelin proteolipid protein. Proc. Natl. Acad. Sci. U. S. A. 92, 4447–51.

Schnyder, S., Svensson, K., Cardel, B., Handschin, C., 2017. Muscle PGC-1α is required for long-term systemic and local adaptations to a ketogenic diet in mice. Am. J. Physiol. Endocrinol. Metab. 312, E437–E446. doi:10.1152/ajpendo.00361.2016

Schwartzbaum, J.A., Fisher, J.L., Aldape, K.D., Wrensch, M., 2006. Epidemiology and molecular pathology of glioma. Nat. Clin. Pract. Neurol. 2, 494–503. doi:10.1038/ncpneuro0289

Shaloam Dasari and Paul Bernard Tchounwou, 2015. Cisplatin in cancer therapy : molecular mechanisms of action. Eur J Pharmacol 5, 364–378. doi:10.1016/j.ejphar.2014.07.025.Cisplatin

Shen, L., Weber, C.R., Turner, J.R., 2008. The tight junction protein complex undergoes rapid and continuous molecular remodeling at steady state. J. Cell Biol. 181, 683–695. doi:10.1083/jcb.200711165

Siegal, T., Rubinstein, R., Bokstein, F., Schwartz, A., Lossos, A., Shalom, E., Chisin, R., Gomori, J.M., 2000. In vivo assessment of the window of barrier opening after osmotic blood—brain barrier disruption in humans. J. Neurosurg. 92, 599–605. doi:10.3171/jns.2000.92.4.0599

Sills, M.A., Forsythe, W.I., Haidukewych, D., MacDonald, A., Robinson, M., 1986. The medium chain triglyceride diet and intractable epilepsy. Arch. Dis. Child. 61, 1168–72.

Simons, K., Toomre, D., 2000. Lipid rafts and signal transduction. Nat Rev Mol Cell Biol 1, 31–39. doi:10.1038/35036052

Simons, M., Krämer, E.M., Macchi, P., Rathke-Hartlieb, S., Trotter, J., Nave, K.A., Schulz, J.B., 2002. Overexpression of the myelin proteolipid protein leads to accumulation of cholesterol and proteolipid protein in endosomes/lysosomes: Implications for Pelizaeus-Merzbacher disease. J. Cell Biol. 157, 327–336. doi:10.1083/jcb.200110138

Simons, M., Krämer, E.M., Thiele, C., Stoffel, W., Trotter, J., 2000. Assembly of myelin by association of proteolipid protein with cholesterol- and galactosylceramide-rich membrane domains. J. Cell Biol. 151, 143–54.

Sims, D.E., 1986. The pericyte - A review. Tissue Cell 18, 153–174. doi:http://dx.doi.org/10.1016/0040-8166(86)90026-1

Singhal, N.K., Huang, H., Li, S., Clements, R., Gadd, J., Daniels, A., Kooijman, E.E., Bannerman, P., Burns, T., Guo, F., Pleasure, D., Freeman, E., Shriver, L., McDonough, J., 2017. The neuronal metabolite NAA regulates histone H3 methylation in oligodendrocytes and myelin lipid composition. Exp. Brain Res. 235, 279–292. doi:10.1007/s00221-016-4789-z

Smith, L.L., Ray, D.R., Moody, J.A., Wells, J.D., Van Lier, J.E., 1972. 24-hydroxycholesterol levels in human brain. J. Neurochem. 19, 899–904. doi:10.11604/pamj.2017.26.57.9021

Snaidero, N., Möbius, W., Czopka, T., Hekking, L.H.P., Mathisen, C., Verkleij, D., Goebbels, S., Edgar, J., Merkler, D., Lyons, D. a, Nave, K.-A., Simons, M., 2014. Myelin membrane wrapping of CNS axons by PI(3,4,5)P3-dependent polarized growth at the inner tongue. Cell 156, 277–90. doi:10.1016/j.cell.2013.11.044

Sofroniew, M. V., 2015. Astrocyte barriers to neurotoxic inflammation. Nat. Rev. Neurosci. 16, 249–263. doi:10.1038/nrn3898

Southwood, C., Olson, K., Wu, C., Gow, A., 2007. Novel alternatively spliced endoplasmic reticulum retention signal in the cytoplasmic loop of Proteolipid Protein-1. J. Neurosci. Res. 85, 471–8. doi:10.1002/jnr.21153

Southwood, C.M., Garbern, J.Y., Jiang, W., Gow, A., 2002. The unfolded protein response modulates disease severity in Pelizaeus-Merzbacher disease. Neuron 36, 585–96.

Spector, R., 1989. Eicosanoids and the blood-brain barrier. Ann. N. Y. Acad. Sci. 559, 146–52.

Stamatovic, S.M., Johnson, A.M., Sladojevic, N., Keep, R.F., Andjelkovic, A. V., 2017. Endocytosis of tight junction proteins and the regulation of degradation and recycling. Ann. N. Y. Acad. Sci. 1397, 54–65. doi:10.1111/nyas.13346

Stamatovic, S.M., Keep, R.F., Wang, M.M., Jankovic, I., Andjelkovic, A. V., 2009. Caveolae-mediated internalization of occludin and claudin-5 during CCL2-induced tight junction remodeling in brain endothelial cells. J. Biol. Chem. 284, 19053–19056. doi:10.1074/jbc.M109.000521

Stamatovic, S.M., Sladojevic, N., Keep, R.F., Andjelkovic, A. V, 2012. Relocalization of junctional adhesion molecule A during inflammatory stimulation of brain endothelial cells. Mol. Cell. Biol. 32, 3414–27. doi:10.1128/MCB.06678-11

Stupp, R., Mason, W.P., van den Bent, M.J., Weller, M., Fisher, B., Taphoorn, M.J.B., Belanger, K., Brandes, A.A., Marosi, C., Bogdahn, U., Curschmann, J., Janzer, R.C., Ludwin, S.K., Gorlia, T., Allgeier, A., Lacombe, D., Cairncross, J.G., Eisenhauer, E., Mirimanoff, R.O., 2005. Radiotherapy plus Concomitant and Adjuvant Temozolomide for Glioblastoma. N. Engl. J. Med. 352, 987–996. doi:10.1056/NEJMoa043330

Sullivan, P.G., Rippy, N.A., Dorenbos, K., Concepcion, R.C., Agarwal, A.K., Rho, J.M., 2004. The Ketogenic Diet Increases Mitochondrial Uncoupling Protein Levels and Activity. Ann. Neurol. 55, 576–580. doi:10.1002/ana.20062

Supplie, L.M., Düking, T., Campbell, G., Diaz, F., Moraes, C.T., Götz, M., Hamprecht, B., Boretius, S., Mahad, D., Nave, K.-A., 2017. Respiration-Deficient Astrocytes Survive As Glycolytic Cells *In Vivo*. J. Neurosci. 37, 4231–4242. doi:10.1523/JNEUROSCI.0756-16.2017

Sussman, D., Ellegood, J., Henkelman, M., 2013. A gestational ketogenic diet alters maternal metabolic status as well as offspring physiological growth and brain structure in the neonatal mouse. BMC Pregnancy Childbirth 13, 1–10. doi:10.1186/1471-2393-13-198

Swanton, E., Holland, A., High, S., Woodman, P., 2005. Disease-associated mutations cause premature oligomerization of myelin proteolipid protein in the endoplasmic reticulum. Proc. Natl. Acad. Sci. U. S. A. 102, 4342–7. doi:10.1073/pnas.0407287102

Sweeney, M.D., Sagare, A.P., Zlokovic, B. V., 2018. Blood–brain barrier breakdown in Alzheimer disease and other neurodegenerative disorders. Nat. Rev. Neurol. 14, 133–150. doi:10.1038/nrneurol.2017.188

Szatmári, T., Lumniczky, K., Désaknai, S., Trajcevski, S., Hídvégi, E.J., Hamada, H., Sáfrány, G., 2006. Detailed characterization of the mouse glioma 261 tumor model for experimental glioblastoma therapy. Cancer Sci. 97, 546–553. doi:10.1111/j.1349-7006.2006.00208.x

Tétrault, S., Chever, O., Sik, A., Amzica, F., 2008. Opening of the blood-brain barrier during isoflurane anaesthesia. Eur. J. Neurosci. 28, 1330–41. doi:10.1111/j.1460-9568.2008.06443.x

Thal, S.C., Luh, C., Schaible, E.-V., Timaru-Kast, R., Hedrich, J., Luhmann, H.J., Engelhard, K., Zehendner, C.M., 2012. Volatile Anesthetics Influence Blood-Brain Barrier Integrity by Modulation of Tight Junction Protein Expression in Traumatic Brain Injury. PLoS One 7, e50752. doi:10.1371/journal.pone.0050752

Tieu, K., Perier, C., Caspersen, C., Teismann, P., Wu, D.C., Yan, S. Du, Naini, A., Vila, M., Jackson-Lewis, V., Ramasamy, R., Przedborski, S., 2003. D-β-Hydroxybutyrate rescues mitochondrial respiration and mitigates features of Parkinson disease. J. Clin. Invest. 112, 892–901. doi:10.1172/JCI200318797

Tornavaca, O., Chia, M., Dufton, N., Almagro, L.O., Conway, D.E., Randi, A.M., Schwartz, M.A., Matter, K., Balda, M.S., 2015. ZO-1 controls endothelial adherens junctions, cell-cell tension, angiogenesis, and barrier formation. J. Cell Biol. 208, 821–838. doi:10.1083/jcb.201404140

Trajkovic, K., Dhaunchak, A.S., Goncalves, J.T., Wenzel, D., Schneider, A., Bunt, G., Nave, K.A., Simons, M., 2006. Neuron to glia signaling triggers myelin membrane exocytosis from endosomal storage sites. J. Cell Biol. 172, 937–948. doi:10.1083/jcb.200509022

Turner, L.A., Fujimoto, K., Suzuki, A., Stadnicka, A., Bosnjak, Z.J., Kwok, W.M., 2005. The interaction of isoflurane and protein kinase C-activators on sarcolemmal K ATP channels. Anesth. Analg. 100, 1680–1686. doi:10.1213/01.ANE.0000152187.17759.F6

Umeda, K., Ikenouchi, J., Katahira-Tayama, S., Furuse, K., Sasaki, H., Nakayama, M., Matsui, T., Tsukita, S., Furuse, M., Tsukita, S., 2006. ZO-1 and ZO-2 Independently Determine Where Claudins Are Polymerized in Tight-Junction Strand Formation. Cell 126, 741–754. doi:10.1016/j.cell.2006.06.043

Urbanska, K., Sokolowska, J., Szmidt, M., Sysa, P., 2014. Glioblastoma multiforme - An overview. Wspolczesna Onkol. 18, 307–312. doi:10.5114/wo.2014.40559

Valente-Silva, P., Lemos, C., Köfalvi, A., Cunha, R.A., Jones, J.G., 2015. Ketone bodies effectively compete with glucose for neuronal acetyl-CoA generation in rat hippocampal slices. NMR Biomed. 28, 1111–1116. doi:10.1002/nbm.3355

Vanmierlo, T., Weingärtner, O., van der Pol, S., Husche, C., Kerksiek, A., Friedrichs, S., Sijbrands, E., Steinbusch, H., Grimm, M., Hartmann, T., Laufs, U., Böhm, M., de Vries, H.E., Mulder, M., Lütjohann, D., 2012. Dietary intake of plant sterols stably increases plant sterol levels in the murine brain. J. Lipid Res. 53, 726–35. doi:10.1194/jlr.M017244

Vannucci, S.J., Maher, F., Simpson, I.A., 1997. Glucose transporter proteins in brain: delivery of glucose to neurons and glia. Glia 21, 2–21. doi:10.1002/(SICI)1098-1136(199709)21:1<2::AID-GLIA2>3.0.CO;2-C

Varatharaj, A., Galea, I., 2017. The blood-brain barrier in systemic inflammation. Brain. Behav. Immun. 60, 1–12. doi:10.1016/j.bbi.2016.03.010

Vazana, U., Veksler, R., Pell, G.S., Prager, O., Fassler, M., Chassidim, Y., Roth, Y., Shahar, H., Zangen, A., Raccah, R., Onesti, E., Ceccanti, M., Colonnese, C., Santoro, A., Salvati, M., D'Elia, A., Nucciarelli, V., Inghilleri, M., Friedman, A., 2016. Glutamate-Mediated Blood-Brain Barrier Opening: Implications for Neuroprotection and Drug Delivery. J. Neurosci. 36, 7727–7739. doi:10.1523/JNEUROSCI.0587-16.2016

Wang, P.J., Young, C., Liu, H.M., Chang, Y.C., Shen, Y.Z., 1995. Neurophysiologic studies and MRI in Pelizaeus-Merzbacher disease: Comparison of classic and connatal forms. Pediatr. Neurol. 12, 47–53. doi:10.1016/0887-8994(94)00124-K

Wang, Y., Jin, S., Sonobe, Y., Cheng, Y., Horiuchi, H., Parajuli, B., Kawanokuchi, J., Mizuno, T., Takeuchi, H., Suzumura, A., 2014. Interleukin-1β induces blood-brain barrier disruption by downregulating sonic hedgehog in astrocytes. PLoS One 9, 1–8. doi:10.1371/journal.pone.0110024

Waxman, S.G., 1980. Determinants of conduction velocity in myelinated nerve fibers. Muscle Nerve 3, 141–150. doi:10.1002/mus.880030207

Webber, R.J., Edmond, J., 1977. Utilization of L(+)-3-hydroxybutyrate, D(-)-3-hydroxybutyrate, acetoacetate, and glucose for respiration and lipid synthesis in the 18-day-old rat. J. Biol. Chem. 252, 5222–6.

Wei, K., Chu, P., Wang, H.J., Huang, C., Chen, P., Tsai, H.-C., Lu, Y., Lee, P., Tseng, I., Feng, L., Hsu, P., Yen, T., Liu, H.-L., 2013. Focused Ultrasound-Induced Blood–Brain Barrier Opening to Enhance Temozolomide Delivery for Glioblastoma Treatment: A Preclinical Study. PLoS One 8, e58995. doi:10.1371/journal.pone.0058995

Werner, H.B., Krämer-Albers, E.M., Strenzke, N., Saher, G., Tenzer, S., Ohno-Iwashita, Y., De Monasterio-Schrader, P., Möbius, W., Moser, T., Griffiths, I.R., Nave, K.A., 2013. A critical role for the cholesterol-associated proteolipids PLP and M6B in myelination of the central nervous system. Glia 61, 567–586. doi:10.1002/glia.22456

Westphal, M., Hilt, D.C., Bortey, E., Delavault, P., Olivares, R., Warnke, P.C., Whittle, I.R., Jääskeläinen, J., Ram, Z., 2003. A phase 3 trial of local chemotherapy with biodegradable carmustine (BCNU) wafers (Gliadel wafers) in patients with primary malignant glioma. Neuro. Oncol. 5, 79–88. doi:10.1093/neuonc/5.2.79

Witt, K. a, Mark, K.S., Hom, S., Davis, T.P., 2003. Effects of hypoxia-reoxygenation on rat blood-brain barrier permeability and tight junctional protein expression. Am. J. Physiol. Heart Circ. Physiol. 285, H2820--31. doi:10.1152/ajpheart.00589.2003

Wolf, N.I., Sistermans, E.A., Cundall, M., Hobson, G.M., Davis-Williams, A.P., Palmer, R., Stubbs, P., Davies, S., Endziniene, M., Wu, Y., Chong, W.K., Malcolm, S., Surtees, R., Garbern, J.Y., Woodward, K.J., 2005. Three or more copies of the proteolipid protein gene PLP1 cause severe Pelizaeus-Merzbacher disease. Brain 128, 743–751. doi:10.1093/brain/awh409

Woodfin, A., Voisin, M.B., Nourshargh, S., 2007. PECAM-1: A multi-functional molecule in inflammation and vascular biology. Arterioscler. Thromb. Vasc. Biol. 27, 2514–2523. doi:10.1161/ATVBAHA.107.151456

Woodward, K.J., 2008. The molecular and cellular defects underlying Pelizaeus-Merzbacher disease. Expert Rev. Mol. Med. 10, e14. doi:10.1017/S1462399408000677

Wu, X., Lu, Y., Dong, Y., Zhang, G., Zhang, Y., Xu, Z., Culley, D.J., Crosby, G., Marcantonio, E.R., Tanzi, R.E., Xie, Z., 2012. The inhalation anesthetic isoflurane increases levels of proinflammatory cytokines TNF-α, IL-6, and IL-1β. Neurobiol. Aging 33, 1364–1378. doi:10.1016/j.neurobiolaging.2010.11.002

Xiao, G., Gan, L.-S., 2013. Receptor-mediated endocytosis and brain delivery of therapeutic biologics. Int. J. Cell Biol. 2013, 703545. doi:10.1155/2013/703545

Xu, Q., 2006. Profile and Regulation of Apolipoprotein E (ApoE) Expression in the CNS in Mice with Targeting of Green Fluorescent Protein Gene to the ApoE Locus. J. Neurosci. 26, 4985–4994. doi:10.1523/JNEUROSCI.5476-05.2006

Yamamoto, M., Ramirez, S.H., Sato, S., Kiyota, T., Cerny, R.L., Kaibuchi, K., Persidsky, Y., Ikezu, T., 2008. Phosphorylation of claudin-5 and occludin by Rho kinase in brain endothelial cells. Am. J. Pathol. 172, 521–533. doi:10.2353/ajpath.2008.070076

Yamamoto, T., Shimojima, K., 2013. Pelizaeus-Merzbacher disease as a chromosomal disorder. Congenit. Anom. (Kyoto). 53, 3–8. doi:10.1111/cga.12005

Yang, S., Wu, Q., Huang, S., Wang, Z., Qi, F., 2016. Sevoflurane and isoflurane inhibit KCl-induced Class II phosphoinositide 3-kinase α subunit mediated vasoconstriction in rat aorta. BMC Anesthesiol. 16, 1–10. doi:10.1186/s12871-016-0227-9

Yang, X., Cheng, B., 2010. Neuroprotective and anti-inflammatory activities of ketogenic diet on MPTP-induced neurotoxicity. J. Mol. Neurosci. 42, 145–153. doi:10.1007/s12031-010-9336-y

Yang, Y., Estrada, E.Y., Thompson, J.F., Liu, W., Rosenberg, G.A., 2007. Matrix metalloproteinase-mediated disruption of tight junction proteins in cerebral vessels is reversed by synthetic matrix metalloproteinase inhibitor in focal ischemia in rat. J. Cereb. Blood Flow Metab. 27, 697–709. doi:10.1038/sj.jcbfm.9600375

Yao, Y., Chen, Z., Norris, E.H., Strickland, S., 2014. Astrocytic laminin regulates pericyte differentiation and maintains blood brain barrier integrity. Nat. Commun. 5, 1–26. doi:10.1038/ncomms4413

Yudilevich, D.L., De Rose, N., 1971. Blood-brain transfer of glucose and other molecules measured by rapid indicator dilution. Am. J. Physiol. 220, 841–6.

Zhang, H., Gao, S., 2007. Temozolomide/PLGA microparticles and antitumor activity against Glioma C6 cancer cells in vitro. Int. J. Pharm. 329, 122–128. doi:10.1016/j.ijpharm.2006.08.027

Zhang, Y., Chen, K., Sloan, S.A., Bennett, M.L., Scholze, A.R., O'Keeffe, S., Phatnani, H.P., Guarnieri, P., Caneda, C., Ruderisch, N., Deng, S., Liddelow, S.A., Zhang, C., Daneman, R., Maniatis, T., Barres, B.A., Wu, J.Q., 2014. An RNA-Sequencing Transcriptome and Splicing Database of Glia, Neurons, and Vascular Cells of the Cerebral Cortex. J. Neurosci. 34, 11929–11947. doi:10.1523/JNEUROSCI.1860-14.2014

Zhao, J., Hao, J., Fei, X., Wang, X., Hou, Y., Deng, C., 2014. Isoflurane inhibits occludin expression via up-regulation of hypoxia-inducible factor 1α. Brain Res. 1562, 1–10. doi:10.1016/j.brainres.2014.03.025

Zhao, S., Hu, X., Park, J., Zhu, Y., Zhu, Q., Li, H., Luo, C., Han, R., Cooper, N., Qiu, M., 2007. Selective expression of LDLR and VLDLR in myelinating oligodendrocytes. Dev. Dyn. 236, 2708–2712. doi:10.1002/dvdy.21283

Zhao, X., Yang, Z., Liang, G., Wu, Z., Peng, Y., Joseph, D.J., Inan, S., Wei, H., 2013. Dual Effects of Isoflurane on Proliferation, Differentiation, and Survival in Human Neuroprogenitor Cells. Anesthesiology 118, 537–549. doi:10.1097/ALN.0b013e3182833fae

Zhong, L., Su, J.Y., Ph, D., 2002. Protein Kinase II via MAP Kinase Signaling in Cultured Vascular Smooth Muscle Cells 148–154.

Ziello, J.E., Jovin, I.S., Huang, Y., 2007. Hypoxia-inducible factor (HIF) -1 regulatory pathway and its potential for therapeutic intervention in malignancy and ischemia. Yale J. Biol. Med. Med. 80, 51–60. doi:10.1038/nature06613

Zlokovic, B. V., 2008. The Blood-Brain Barrier in Health and Chronic Neurodegenerative Disorders. Neuron 57, 178–201. doi:10.1016/j.neuron.2008.01.003